Utrecht University

Faculty of Science

The gravitational collapse of colloidal gels

Master's Thesis

Martijn van Schaik

Theoretical Physics

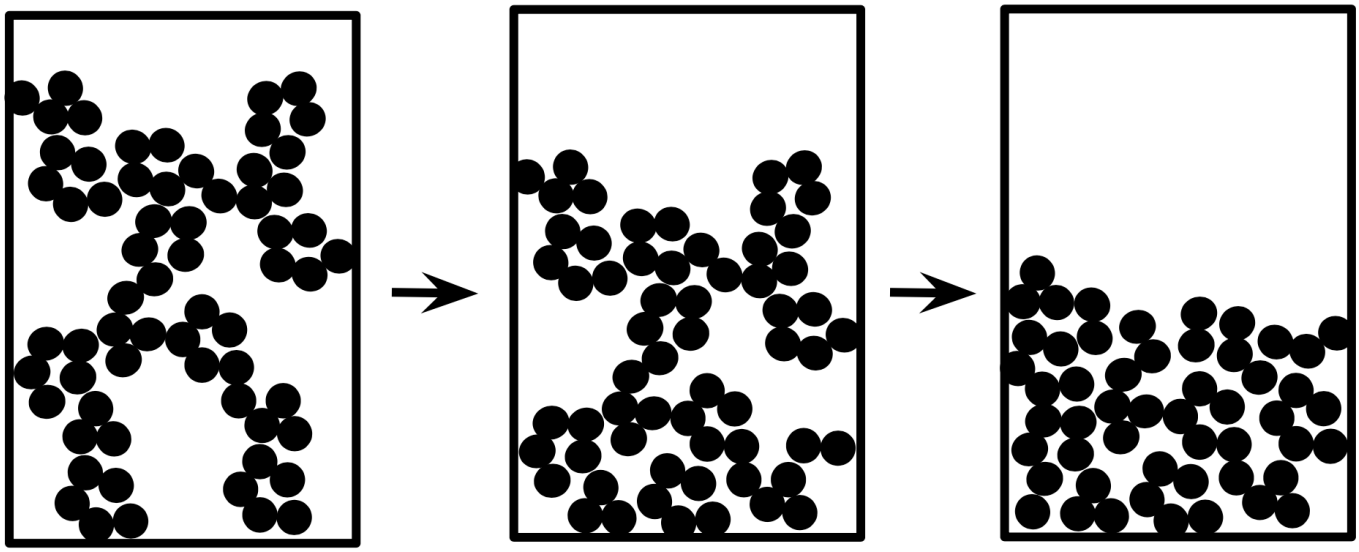

Supervisors:

K.W. Torre MSc
Institute for Theoretical Physics

Dr. J. de Graaf
Institute for Theoretical Physics

Prof. Dr. R.H.H.G. van Roij
Institute for Theoretical Physics

July 2024

Abstract

Colloidal gels are suspensions of micro-sized particles that can form a network-like structure, when interacting via a short-ranged attraction with bond energy much greater than the thermal energy. Under applied stresses, the network response is both viscous and elastic. Interestingly, there is a range of parameters in which the response is a delayed collapse. This response is initially elastic, followed by a rapid collapse in which the network disintegrates and the response is viscous. The collapse behaviour outside this range is relatively well understood, but a fundamental picture of the delayed collapse is yet incomplete. In this thesis project, we show that a continuum method can overcome the particular challenges that this problem poses to the more traditional approaches, such as experimental studies and particle-based simulations. Our model includes the viscous stress of fluid flow through the network and the elastic stress due to osmotic pressure, which we expect to explain the delay behaviour. However, we found that the elastic network response due to osmotic pressure does not play a role in this collapse process. Also, we show the delay times that our model produces to be a grid artifact. In comparison to a recent study that finds a larger delay time due to a visco-elastic stress, we identify this stress as (one of) the causes of delayed collapse.

Figure 1: (Title page) Schematic representation of the collapse of a colloidal gel. Colloidal particles are represented by black dots, which are suspended in a fluid. The initial state is a (macroscopically) homogeneous network of suspended colloidal particles. While the top of the network remains intact, its bottom collapses. In the final state, the system has phase-separated into a colloid-rich sediment and a supernatant fluid.

Acknowledgements:

K.W. Torre MSc,
for the many lessons and unconditional support.

Dr. J. de Graaf,
for his well-appreciated guidance.

M. van Leeuwen BSc,
for laying the foundations of this project.

And of course

S. Tasci,
for being a loving and supporting partner during this project.

Contents

1 Introduction

There is a large variety of fluids in our everyday life whose behaviour is more challenging to describe than one would expect. While simple, *Newtonian*, fluids flow 'regularly' under stress, complex fluids behave differently. Complex fluids are mixtures of substances of two different phases in coexistence, of which at least one is a fluid. In this thesis project, we are interested in a subclass of complex fluids, *colloidal gels*. *Colloidal* refers to the regime where Brownian forces have a non-negligible effect [1]. In this context, it implies that the dispersed particles have at least one dimension between approximately 1 nm and 1 µm [2]. A colloidal *gel* is defined to be a network of colloidal particles in a suspending medium that spans the sample.

These gels have numerous industrial applications [3], due to their behaviour under deformation and flow, that is, their rheology [4, 5]. These applications include cleaning products [6], hair care products [7], paints [8], proppants (used in oil and gas exploration) [9] and there are applications within food technology and nutrition [10, 11]. Gels have also gained attention in other fields of research, such as bio-engineering, where gels have been applied as scaffold material for tissue engineering [12, 13].

This industrial relevance has led to a large body of practical knowledge on how to form gels with specific mechanical properties [14], however, a full fundamental picture of a gel's rheology is not yet complete. A result of this practical knowledge is the finely tuned non-Newtonian stress response of toothpaste [15]. While the paste flows as we apply a small force to extract it from the tube, it behaves as a solid under gravitational stress on our brush. This type of response is desirable for a lot materials, leading to numerous industrial applications of gels

The usefulness of gels in some of these applications is limited by sedimentation, depending on their 'shelf life', which might range from weeks to years. In any real-world system, a density mismatch between the colloidal and suspending phase is unavoidable [16]. This mismatch gives rise to a buoyant force and ultimately drives leads to sedimentation (or creaming, in case of a negative buoyant density). The long-term behaviour is thus a separation into a colloid-rich and colloid-poor region. However, depending on the gel, different types of separation can be observed: fast sedimentation, delayed collapse, and slow sedimentation [17]. The delayed collapse is characterized by a finite time in which the network bears the buoyant weight, after which the gel settles rapidly, compared to sedimentation processes [17–22]. This time is typically referred to as the *delay time* and has an obvious relation with the shelf life of gel-based industrial applications that rely on the presence of the network. The onset of the rapid settling is not *fully* understood, and among the possible causes are streamer formation — dense clusters falling through the gel, leading to eroded channels in the network — and network collapse [23–27]. These processes are the result of the dynamics of the colloidal particles within the gel, and are clearly related to the gel's stability, and thus its reliability in applications. The goal of this thesis project is to contribute to the knowledge of these dynamics.

Several methods have been applied to study the dynamics of colloidal gels, where efforts can be divided into theoretical, computational, and experimental studies, each approach with its own pros and cons. The foundation of theoretical studies is formed by the poro-elastic model together with continuity equations [22, 19]. The drawback of such studies is that

significant approximations are needed in order to be able to solve the equations. These include reductions regarding the role played by hydrodynamic interactions [28] and viscous stresses due to porous flow [29]. In addition, these studies have been limited to a height-dependent volume fraction, which constrains fluid flow to be vertical. Horizontal flows require another spatial dimension, and so do shearing stresses of the network and a curved meniscus. These features are quite likely to influence the settling behaviour of gels, which has been verified experimentally for a curved meniscus [27].

Experimental studies have not only led to the large number of applications of gels, but also fundamental insights, since the microstructure of a gel is experimentally observable [30–32]. However, the duration of experimental studies is related to the delay time of the system. Since a shelf life of years is desirable for most practical purposes, a 'brute-force' approach to developing new products may require an infeasible amount of time. This means that fundamental experiments need to be conducted on weaker gels that show the salient features of their industrial analogues.

The efforts on the computational side consists mainly of particle-based simulations, which can predict the dynamics of a large number of colloidal particles to great accuracy [33, 21]. However, explicitly simulating each particle is simply not feasible for a typical experimental setup. A container of dimensions $1 \times 1 \times 4$ cm, of which a volume fraction of 10% consists of colloidal particles with a radius of 1 µm, contains about 10^{11} particles. A common way to overcome this challenge is to introduce periodic boundary conditions, which works well to simulate the bulk of the gel. However, the distance of the interactions between particles is still limited, while long-ranged interactions seem to play an important role in the gel's dynamics [34–36]. Also, processes at the boundaries of the gel, such as the forming of dense clusters at the top of the sample, are important in the collapse behaviour of the gel [17, 27]. This limits (particle-based) computational studies to system much smaller than the experimental scale, which is at least one order of magnitude smaller than the industrial scale. This forms an important drawback of these methods, since small-scale systems have been observed to behave differently from gels on these length scales [37].

From the discussion above, we conclude that all methods have such significant drawbacks that they are not useful to predict the collapse behaviour of colloidal gels. To overcome these, we use a hybrid method, combining theory and computation, which describes the system at the continuum level. The foundation of this method is a mean-field approximation, thus in our case we treat the colloidal volume fraction and velocity as a field. In this way, we integrate out the dynamics of the single colloids, but we do have access to mesoscale variables. The theoretical effort is limited to expressing the time evolution of these variables in terms of differential equations. Instead of introducing further approximations that are needed for an analytic solution, we solve these numerically. This leads to a quick generation of detailed information of gel collapse behaviour on experimental time scales, a fast and useful predictive tool once validated by experiment [38].

Our aim is to create a model that is able to provide us with this mesoscale information. Then this model can be used to identify the forces that have an influence on the collapse behaviour, and possibly also tells us *how* it influences the collapse. We will show that a simple model captures one of the separation behaviours. Increasing the complexity of the model by a height-dependent volume fraction will produce a wider range of these behaviours. Also, in the system we model, we can rule out the influence of osmotic pressure on the collapse

behaviour.

This thesis is built up as follows. We provide a broad historical perspective of the problem and related challenges in section 2. In section 3, we dive into the theory that leads up to the model, and specify the system we model in order to exhibit its non-equilibrium nature. Then we model the collapse process of a gel under the assumption that the gel can only compress homogeneously in section 4. When all these aspects have been covered, we move on to modeling the system without this assumption in section 5. In section 6, we compare the results to our expectations and existing literature. Section 7 summarizes this work and provides suggestions for follow-up studies.

2 A historical perspective

In this thesis project, we are interested in the settling behaviour of a specific system, a colloidal gel. This behaviour is rather complicated and depends on a lot of parameters, so we introduce the contributing factors by means of a historical perspective. We start with the simplest case of settling behaviour, a single small sphere in a viscous fluid under the influence of only gravity. Stokes' law [39] states that such a sphere experiences the following drag force

$$F_d = 6\pi\mu r v, \tag{1}$$

where μ is the viscosity of the fluid and r the radius of the settling sphere. If an external force such as gravity is applied to this system, a buoyant force drives an acceleration of the sphere until the drag force balances the driving force, as illustrated in figure 2. At that point, the sphere reaches a terminal, or settling, velocity

$$v_s = \frac{2}{9}\frac{\rho_b g r^2}{\mu}, \tag{2}$$

where the velocity is defined by the motion of the sphere relative to the fluid. The gravitational acceleration is denoted by g, and we have defined a *buoyant* density ρ_b. This is the density difference between the spherical particle and the suspending fluid. Note that the suspended particle is usually assumed to have a higher density than the suspending fluid, such that $\rho_b = \rho_s - \rho_f > 0$. However, these equations hold for any value of buoyant density, leading to 'upward settling', or *creaming* of suspended particles.

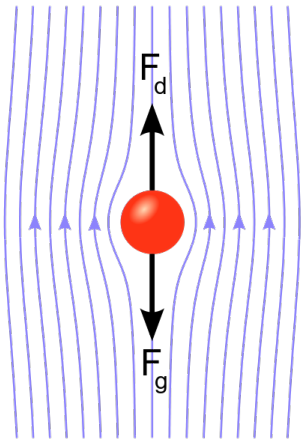

Figure 2: Stokes flow, the red sphere reaches a terminal velocity when the drag force is equal to the gravitational pull. Adapted from [40], with permission.

These equations are relatively simple, but are derived from the much more involved Navier-Stokes (NS) equations. These equations are partial differential equations that have been used to describe viscous flows with great success in fields ranging from ocean currents [41] to aerodynamics [42]. However, it is still unknown whether these equations always have a smooth solution[1] .

The NS equations can be simplified by eliminating terms that have a negligible effect, leading to different sets of equations that are valid in different 'flow regimes'. A system is typically identified to lie in a given regime by a dimensional analysis. This analysis naturally leads to the *Reynolds number*, which is the ratio between inertial and viscous forces,

$$\mathrm{Re} = \frac{\text{inertia}}{\text{viscosity}} = \frac{\rho u L}{\mu}, \tag{3}$$

where ρ is the density of the fluid, u the (relative) velocity of the fluid, L the characteristic length, and μ the viscosity of the fluid. In some cases, it may be unclear what the length scale is that governs the physics. For example, in the case of propagation by wings, different

[1] Whether the Navier-Stokes equations have a solution in general, unique or not, is such an intriguing problem that it has been pronounced one of the millenium prize problems [43].

length scales are available, such as chord length, wake width[2] and flapping amplitude [44]. However, in our case, there are no competing length scales, and thus our characteristic length equals the radius of the colloidal spheres, $L = r$. Clearly, this number was used by Sir George Gabriel Stokes in 1856 to simplify the full NS equations, but its importance was illustrated by Sir Osborne Reynolds in 1883 [45]. His experiments showed that the Reynolds number can be used to characterize flows into either laminar or turbulent, corresponding to a low or high Re, respectively. The transition from laminar to turbulent is not sharp, and the Reynolds number marking this transition depends strongly on the geometry of the system [46]. These limitations are minor remarks, however, compared to the implication of a universal characterization of flows. This was recognised by Sommerfeld in 1908 at the international congress of mathematicians (ICM), referring to this number by its current name [47].

As mentioned before, another use of this number is to reduce the NS equations to a simpler form. For example, $Re \approx 0$ leads to equation 1, if the following assumptions are met. The first assumption is that the flow is laminar, in which flow-lines[3] are smooth and adjacent, as in figure 2. Note that the laminar flow requires that the Reynolds number is lower than some critical value Re_c, which depends on parameters such as the geometry and boundary conditions of the flow, and even the molecular properties of the flowing fluid [48]. Considering fluid flow through a pipe, typical critical values are $Re_c \approx 2000$ [49], such that the laminar flow assumption is always fulfilled when $Re < 1$. The remaining assumptions were met by the definition of the system: The particle is spherical, the fluid is homogeneous, the surfaces are smooth and the sphere is suspended in an infinite fluid, meaning that there are no boundaries to take into account. This illustrates that the Reynolds number can characterize the flow regime of a wide range of systems.

Violating one of the above assumptions allows us to describe a more general system, at the cost of more complicated equations. For example, if there are multiple settling spheres in the system, then the flow that is induced by one sphere affects the other spheres. In 1905, as a by-product of the study of Brownian motion, Albert Einstein [50] proposed a correction of the viscosity of a solution due to a reduced mobility of the solvent surrounding the suspended particles. Applying this correction to equation 2 leads to a corrected sedimenting velocity

$$v_{s,E} = v_s(1 + \alpha\phi)^{-1}, \tag{4}$$

where $\alpha = 2.5$ for hard spheres, and ϕ the volume fraction occupied by these spheres. This expression is valid for hard spheres with a low buoyant density and with a large interparticle distance, relative to their radius. Around the same time, Marian Smoluchowski also studied Brownian motion, and proposed a number of corrections to Stokes' law in 1912 [51]. Most importantly, he proposed a correction like Einstein's, but based on another reasoning, leading to

$$v_{s,S} = v_s(1 - 2.32r/a), \tag{5}$$

[2]The chord length of a wing is the distance measured from front to rear tip. The wake width is related to the size of the low-pressure turbulent region behind the wing.

[3]Flow-lines are the paths that fluid particles follow. Fluid particles are an infinitesimal volume of fluid with a fixed mass, but are different from usual point particles in the sense that they can be compressed and deformed.

where a is the distance between two particles, such that $r/a \propto \phi^{1/3}$. This result follows naturally from a regular arrangement of spheres. The stochastic approach by Batchelor [52] lead to

$$v_{s,B} = v_s(1 - 6.55\phi), \tag{6}$$

which he claimed to be accurate up to first order in ϕ. Around the same time, Maude and Whitmore proposed the following relation [53], based on experimental observations.

$$v_{s,MW} = v_s(1 - \phi)^{\beta}, \tag{7}$$

where β is a function of particle shape, size distribution and Reynolds number. We observe that the *discrete*, particle-based, approach to study the settling behaviour of particles in a specific system is well-established. However, in order to be able to predict settling processes in a more general sense, a different, *continuum* approach is required [54, ch. 4]. In the continuum approach, we treat the volume fraction of settling particles as a continuous function of space. This greatly reduces the complexity of the model, and allows us to introduce interparticle attractions that are present in a gel.

In 1987, Buscall *et al.* [16] introduced the most coarse-grained continuum model that describes the gravitational collapse of colloidal gels. In this model, the system is divided into a homogeneous gel and a colloid-free region above it. We refer to this model as the *poro-elastic* model, after the forces that balance the gravitational stress. In this model, the gravitational stress is balanced against a viscous drag force due to solvent flowing through pores in the network, and an elastic stress developed in the network of particles [19]. This theoretical framework has recently been used to reproduce experimentally observed erythrocyte sedimentation rates. Rather than sedimenting immediately, erythrocytes also sustain gravitational stress without sedimenting for a finite time, which can be explained by regarding a blood sample as a gel [22]. The volume fraction of colloids that describes this physiological system is relatively high, implying that the system is in the creeping regime of sedimentation. That is, the compression or compactification of the network is slow, compared to the sedimentating rate of a red blood cell that is not supported by a network. Manley *et al.* [19] show that gels exhibit a different sedimentation behaviour at lower colloid volume fractions, which this model does not predict, as we will see in section 4. Typically, we lose information if we reduce the dimensionality of a problem, so we expect this approximation as *too* coarse-grained.

2.1 Recent advances

As the power and availability of computers increased, the discrete (very high dimensional) approach developed significantly and could be used to predict the collapse process of a gel. Particle-based simulations give us very detailed information on the dynamics of each particle in the system. In 2016, a study of Harich *et al.* [17] produced a diagram that describes the phase behaviour of colloidal gels. Part of their work was a Brownian dynamics simulation, with a square-well potential rather than the actual, *depletion*[4] potential. This choice is

[4]The attraction that is induced by depletion will be discussed in further detail in section 3.4.

justified by the extended law of corresponding states, as proposed in [55]. This law states that the *effective* range of a collection of potentials (including depletion and square well) can be quantified in terms of the *reduced* second virial coefficient. The second virial coefficient is a function of the pair interaction strength, and reduced means that it is normalized. The normalization is a division by the second virial coefficient of a hard sphere with diameter σ_{eff}, the effective hard-core diameter of the potential [56]. As an example, this law states that the two square well potentials in figure 3, assuming $V_0 = 5\,k_{\text{B}}T$ are corresponding states, since they have the same reduced second virial coefficient. Modeling the interparticle potential as a square well has the advantage that there is a clear definition of a bond. This is essential in the study of gels, since a collection of particles can only be called a network if the particles are bonded together. The Brownian dynamics simulation could thus be used to predict the phase behaviour of a colloid-polymer mixture, in particular whether the system gels or not. Harich *et al.* studied this system with attractions ranging from 0.01σ to 0.1σ, with σ the diameter of the colloids, and bond strengths[5] up to about 10 $k_{\text{B}}T$.

While the extended law of corresponding states work well to relate the phase behaviour induced by short-ranged potentials, it does not mean that the dynamics are the same. For example, in a 2018 Brownian dynamical simulation of freely draining[6] particles by Padmanabhan and Zia [21], similar phase behaviour but different collapse behaviours were reported. The focus of this study was to explain the delay behaviour of the collapse, which they did observe in their system of small particles. They used a Morse interaction potential,

$$V_{\text{Morse}} = V_0\left(\exp[-2a(r-\sigma)] - 2\exp[-a(r-\sigma)],\right) \tag{8}$$

with $V_0 \sim 5 - 6\,k_{\text{B}}T$ the well depth and (inverse) width parameter $a = 60/\sigma$, see figure 3. In this paper, it is proposed that pores are created and widened due to the fluid flow through the network. These pores decrease the viscous stress of fluid backflow that supports the network, thus allowing more fluid flow and faster pore widening. They propose this is a catastrophic process that underlies the sudden collapse of the network.

This proposition is supported by a Brownian dynamical study by Varga *et al.* [23], in which a stability criterion was introduced. This criterion makes a division between stable and unstable gels, and is based on the *aging* of the gel. Aging can be described by the competition between the following two simultaneous processes. The first is pore forming, decreasing the viscous drag of fluid backflow. The second is slow compactification, which increases the strength of the gel. This strength could become large enough to fully support its own weight [19], thus without the 'support' of fluid backflow. For stable (or strong) gels, the delay time associated with pore forming is larger than the characteristic time associated with this strengthening. Their settling behaviour is described as creeping sedimentation. In unstable (or weak) gels, the delay time until large pores are formed has lapsed before the network can support its own weight and thus rapid settling occurs.

[5] Bond strength refers to the BDE, or the 'well depth' V_0

[6] Freely draining or settling refers to the behaviour of a single particle in an infinite fluid. In this context, it means that particles experience a Stokes drag force as they move through the suspending fluid, but their movement does not affect the fluid. This implies that the fluid does not mediate (hydrodynamic) interactions between the colloidal particles.

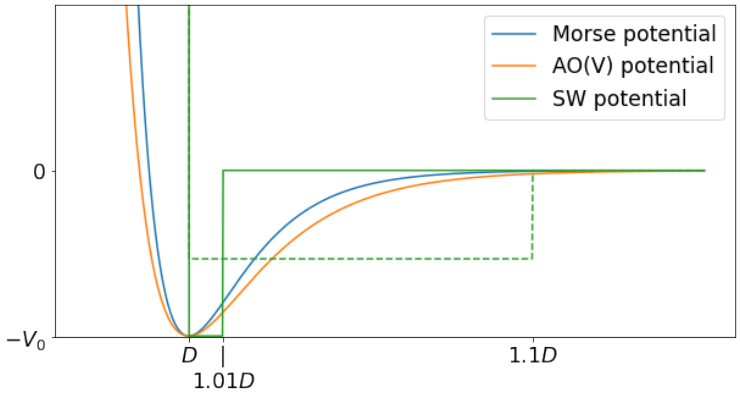

Figure 3: Visual representation of different potentials associated with the interparticle pair interaction of colloids, where V_0 is the well depth of the interaction (corresponding to the BDE). The Asakura-Oosawa(-Vrij)-interaction represents the effective attraction induced by depletion. It can be modeled by a generalized 'high exponent' Lennard Jones potential, see equation 9. The two square well potentials have the same reduced second virial coefficient, such that these potentials have the same *effective* interaction range.

The delay time

There is an important difference between the study of Padmanabhan and Zia [21] and most other BD simulations. They find a delay time, while other simulations capture only the rapid collapse and subsequent slow compactification. At this point, the source of this discrepancy *could* be the different interaction potentials. For comparison, we report the generalized 'high-exponent' Lennard-Jones potential that was used by Torre *et al.* [57].

$$V_{\mathrm{LJ}}^{\mathrm{he}} = V_0 \left[\left(\frac{D}{r} \right)^{96} - 2 \left(\frac{D}{r} \right)^{48} \right] \tag{9}$$

This is a smooth approximation to the generally accepted representation of depletion, the Asakura-Oosawa-Vrij (AOV) potential [58]. In figure 3, we see that the AOV potential is similar to the Morse potential. However, they reported no delay time either. In order to explain this discrepancy, we study the relative influence of gravitational and Brownian forces. We denote the time it takes for a particle to settle a distance equal to its radius r by τ_s, and the time to diffuse that same distance by τ_d. We express τ_d as the time corresponding to a mean squared displacement of r^2, such that $\tau_d \propto r^2/D$, with D the diffusion coefficient. The proportionality constant depends on the dimensionality of the problem, but is not relevant here. At the colloidal scale of our problem, we can express the diffusion coefficient using the Stokes-Einstein-Sutherland equation [59],

$$D = \frac{k_B T}{6\pi\mu r}. \tag{10}$$

We introduce the dimensionless gravitational Péclet number as the ratio of τ_d to τ_s,

$$\mathrm{Pe}_g = \frac{\text{diffusion time } \tau_d}{\text{settling time } \tau_s} \propto \frac{2\rho_b g r^2}{9\, r\mu} \frac{r^2}{D} = \frac{4\pi g \rho_b r^4}{3 k_B T}, \tag{11}$$

where we have used equation 2 to define the settling time as $t_s = r/v_s$. We observe that this number strongly depends on the size of the particles. Thus, when comparing the outcome of different studies, this must be taken into account. Harich *et al.* [17] studied particles with a radius of 326 nm in a suspending medium with a density difference of 253 kg m^{-3}. Assuming 'normal' conditions, $g = 9.81$ m s^{-2} and $k_BT = 4.11 \times 10^{-21}$, we find that $\mathrm{Pe}_g \approx 0.03$. Padmanabhan *et al.* [21] studied systems with $\mathrm{Pe}_g \sim 0.01 - 0.1$ and reported a delay time of the order of a hundred τ_d. The discrepancy is resolved by comparing the time scales. Using a typical value of $\mu \approx 10^{-3}$ Pa s, we find that $\tau_d \approx 2\,\mathrm{Pe}_g$ s. Since the delay times are expected to lie in a range of minutes to months [17], a delay time on the order of a second is quite likely to go unnoticed.

2.2 The role of hydrodynamic interactions

Another topic of debate in the context of gel dynamics is the role of hydrodynamic interactions. These are dynamic colloid-colloid interactions mediated by the suspending medium, and we will denote such interactions by the abbreviation HIs. They have been hypothesized to be one of the mechanics underlying the collapse of colloidal gels, which is why devote some of our attention to them here. While HIs do not significantly affect equilibrium structure [60], different effects of HIs on the dynamics of colloidal gels were reported [61, 57, 35, 62–64]. Gels that are formed by arrested phase decomposition are (highly) out-of-equilibrium systems, such that HIs can play a role in the formation of the structure [65] and affect mechanical properties. We highlight a few results below in chronological order.

In the 2016 study of Harich *et al.* [17], the collapse behaviour of colloidal gels was also studied in an experimental setup. They observed dense clusters forming at the top of the gel, and proposed that HIs play a role in the forming of these clusters. This was based on the inability of the Brownian dynamics simulations that excluded HIs to reproduce these. They also found experimental evidence that these clusters fall through the gel when their weight exceeds the yield strength, which was verified a few years later [27].

A normal mode analysis of colloidal gels in 2018 [36], in which systems with and without HIs were compared, led to the conclusion that short-ranged HIs have no significant influence. Long-ranged HIs were reported to play a central role in the viscoelasticity of the gel network, and play a smaller role at higher colloid volume fractions due to *screening*[7] effects. Electric field screening is due to induced flow of mobile charges, but the hydrodynamic 'field' *is* a flow. HIs are thus not screened by mobile particles, but only by fixed particles or boundaries [66, 67]. In the same year, Varga *et al.* [23] performed Brownian dynamical simulations with an attractive square well potential that includes long-ranged HIs. They kept track of vertical pores in the system, which allowed them to introduce (small) initial pores. They showed that their model reproduces experimentally observed delay times faithfully. This suggests that the exclusion of short-ranged HIs does not have a significant effect on the delay time of the collapse process.

More recently, in 2022, Turetta *et al.* [68] reported the same results on the effect of HIs, by

[7] You may have encountered the term screening in the context of the reduction of the effective strength of an electric field. It is explained by the induced flow of mobile charge-carriers, effectively increasing the density of opposing charges near an electric source. This limits the range of the induced interaction by the field.

comparing their Brownian dynamical studies without HIs, with long-ranged HIs and short-ranged HIs. They used the Hamaker equation [69] to model Van der Waals attraction between the colloids, and reported a colloid volume fraction of $\phi \approx 0.2$ above which they report the long-ranged HIs to be screened. Again, hydrodynamic screening should be interpreted as 'dominated by other interactions'. They also suggest that including short-ranged HIs decrease the aggregation rate, related to the aging of a gel. This is in sharp contrast to a more recent study by Torre *et al.* [57] which shows that short-ranged lubrication effects do have a significant effect at low ϕ, and that these effects *accelerate* the aging of a gel. Relatively recently, the seemingly contradictory reports on the effects of HIs were unified by the observation that these effects are dependent on the colloid volume fraction [70]. The authors also reported that on corresponding *structural times*, (i.e. times corresponding to percolation and the onset of aging,) the structural differences reported earlier [65] were not significant.

2.3 Kynch theory

The alternative, continuum, approach, also developed further with the increase of available computational power. The foundation could be the Kynch theory of sedimentation [71]. The fundamental assumption here is that the velocity of a sedimenting particle *only* depends on the local volume fraction. This assumption is shown to be reasonable if the particle propagation is relatively slow or considerably damped [71]. These constraints are not too stringent, such that this theory can successfully describe sedimenting spheres [72]. In fact, this theory seems to be the basis of most models of fluid-structure interactions [73–75]. In our system, a colloidal gel, the structure is the network of particles, and the fluid its suspending medium. The application of this theory justified by the damped propagation of particles. We expect their freedom of movement to be severely limited, due to their relatively strong attraction. Thus, Kynch theory will form the basis of our model in section 5.

3 Theory and background

At this point, we have defined a gel to be a *percolating*, i.e. sample-spanning, network of particles. The network is formed by bonds due to a short-ranged attractive potential between these particles. We are interested in the behaviour of these systems, in particular their collapse. In order to study this phenomenon, we need a description of the mechanics that govern this behaviour. These mechanics clearly depend on the structure and mechanical properties of the gel, partially determined by the mechanism that underlies the forming of the gel, and its preparation procedure [76, 77, 31, 78]. Before we dive into the specifics that underlie the formation of a colloidal gel, we discuss the stress-strain relationship.

3.1 The stress-strain relation

The stress-strain relation, or curve, is a macroscopic description of a material's physical strength. It relates the deformation of a material to its internal stress. It is an important tool in the classification of substances, which informs us of the state of matter they are in [79, 80]. The simplest cases are common states of matter such as solids, liquids and gases. The behaviour of a liquid is qualitatively different from that of a solid, but similar to that of a gas. Thus we limit our attention to differences between solids and fluids from here on. A solid responds *elastically*, thus 'bouncing back' if a given stress is removed. A fluid typically dissipates the energy of a stress[8], and removing the stress does not undo the deformation. This means that we can easily distinguish between solids and fluids by applying and removing a stress. However, mixtures do not necessarily behave as a single state of matter. A class of substances that often exhibits both types of stress response is the class of complex fluids. These are mixtures of substances of two different phases in coexistence, of which at least one is a fluid. Gels belong to the class of complex fluids and exhibit this particular stress response [81].

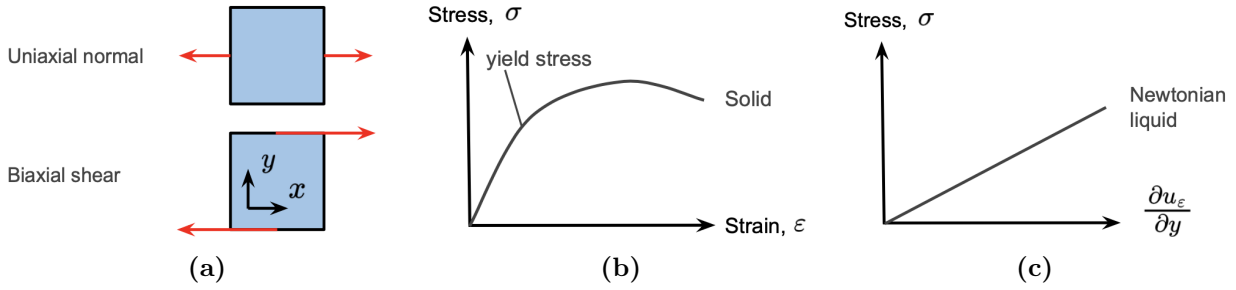

Figure 4: a) Different types of stress on a control volume. b) Typical stress-strain curve for a solid, the amount of stress for which the stress-strain curve of the solid is no longer linear is indicated by 'yield stress'. c) The stress response of a Newtonian fluid is expressed in terms of the deformation rate $\partial_y u_\varepsilon$, where x points in the direction of the deformation and y is normal to this direction, as indicated in a).

We illustrate this with a comparison to the typical stress-strain relation of solids and fluids. In order to appreciate the broadness of this relation, we consider its constituents in

[8]Note that there are a lot of different types of stress. A shearing stress is typically dissipated, but an incompressible fluid responds elastically to a compressing stress.

their full generality. Stress is the force per unit area, and when we consider a unit volume, it can be found to act in different ways on each set of faces. Stresses can act in a normal or a shear form, or as a mixture of these, and are thus not necessarily uniaxial[9], see figure 4a. Strain is the deformation associated with the applied stress and comes in many forms, such as compression, stretching, torsion, and rotation. In figure 4b, we see the typical stress response of a solid. This response is elastic; as soon as the applied stress is removed, the deformation is reverted, with a maximum stress known as the elastic limit. This type of yielding can only be determined by careful testing, but the proportionality limit can simply be read off from the stress-strain curve. This limit is indicated in figure 4b by 'yield stress', and corresponds to the maximum amount of stress up to which stress is proportional to strain.

In the case of fluids, the strain is only well-defined if the freedom of movement is constrained by impermeable walls. In the more general case, the freedom of movement allows dissipation of the energy that a stress introduces in the system. This is a viscous stress response, for which the stress-strain relationship is time- and space-dependent. This response is captured by a velocity gradient, that we will refer to as the *deformation rate*.

The most natural way to express deformation rate is in terms of shearing stresses, denoted by τ. We introduce the time-dependence by the rate of shear[10] $u_\varepsilon = \partial_t \varepsilon$. This is illustrated by an example, laminar fluid flow, parallel to a no-slip surface at $y = 0$, see figure 5. The space-dependence is captured by taking the spatial derivative of u_ε in the direction normal to the fluid flow, in this case $\hat{y}$, defining the deformation rate $\partial_y u_\varepsilon$. In the example of laminar flow, the deformation rate is simply the relative velocity of adjacent layers. These layers experience internal friction due to this motion, and the following relation was proposed by Newton

$$\tau = \mu \frac{\partial u_\varepsilon}{\partial y}, \tag{12}$$

where μ is the viscosity of the fluid. This surprisingly simple equation holds for most velocity gradients encountered in practice [83]. Fluids for which this linear relation holds accurately are referred to as *Newtonian* or 'simple' fluids.

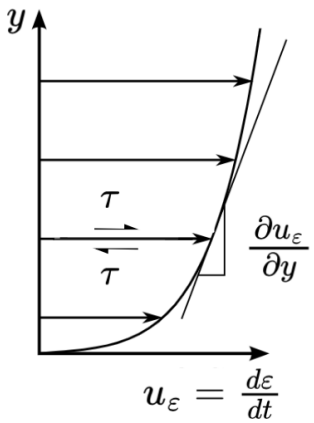

Figure 5: Laminar flow parallel to a no-slip boundary at $y = 0$, illustrating the deformation rate $\partial_y u_\varepsilon$. Shearing stresses are denoted by τ and the rate of shear by u_ε. Figure adapted from public domain [82].

The stress responses discussed above are thus fundamentally different, but some materials exhibit both viscous and elastic behaviour. These are known as viscoelastic materials, whose type of stress response depends on the magnitude of the applied stress [84]. As mentioned before, gels belong to this class of materials, where the elastic response is due to the structure of the network, with a given yield stress. For stresses larger than the yield stress, the network collapses, driving an opposing flow of the suspending fluid. The elastic response

[9]Note that this point of view is typical for fluid dynamics and deviates from the common idea of point masses.

[10]Note that shear is used to refer to the shearing strain, i.e. the displacement of a face of the control volume in its tangential direction.

thus corresponds to the stretching of bonds in the network under moderate stresses, and the viscous response to the fluid flow after these bonds break under higher stresses [85]. Thus the strength of the bonds play an important role in the transition point of the stress response.

In this thesis project, we will be mostly concerned with strain in the form of compression. Fluids are often assumed to be incompressible, and so is our suspending medium. However, the network of suspended particles *is* compressible, but resists compression, as shown by experiment [19, 17, 27]. Depending on the magnitude of the stress, the response is elastic or viscous. This type of viscosity is described by 'dilatational viscosity', and denoted by ζ [86, 87].

3.2 Types of gel

The macroscopic behaviour of a gel depends on a number of factors, of which we discussed the colloid radius r. Other important factors are the initial volume fraction of colloids ϕ_0 and the bonds between the colloidal particles [22, 19, 17, 24]. Here, we study the different macroscopic behaviours that gels can exhibit due to different bonds. The most important characteristic of a bond is its strength, often expressed as the bond dissociation energy (BDE). Its typical unit is $k_\mathrm{B}T$, where k_B is the Boltzmann constant and T the temperature. Bonds may be broken stochastically, due to the Brownian motion of the colloidal particles. The probability of bond breaking depends on the *thermal energy* corresponding to the kinetic energy of colliding molecules. The characteristic energy of a degree of freedom is one $k_\mathrm{B}T$, thus the thermal energy is typically a few $k_\mathrm{B}T$. A gel can already form with an attraction strength corresponding to a BDE just above the thermal energy[11]. However, such a network reorders on small time scales due to the high probability of bond breaking. This allows the system to quickly phase-separate into a dense region of attractive colloids and a dilute phase. This corresponds to the equilibrium state of the system, but not all gel systems reach equilibrium. For example, when the bonds are covalent [89, 90], these are often considered to be irreversible and thus the system does not change on experimentally available timescales. Note that covalent bonds are typically expressed in eV, where one $k_\mathrm{B}T \approx 25$ meV, such that the associated BDE is on the order of a hundred $k_\mathrm{B}T$ [91, 92]. The behaviour of gels that are formed by attractions with an intermediate BDE is less straightforward and will be at the focus of our attention. Examples of such bonds are depletion interactions (which we will discuss in further detail in section 3.4), hydrogen bonds and hydrophobic effects [93].

There are many examples of systems in which these interactions occur, allowing them to form gels, such as a dispersion of sterically stabilized colloidal silica in a liquid that poorly solvates the grafted chains [94, 95]. This system has the property that the gel formation is reversible with temperature as the control parameter. Gels are also studied in the context of biology, for example in the context of erythrocyte (i.e. red blood cells) sedimentation rate[12], one of the oldest medical diagnostic tools, with its origin in ancient times [22].

In order to characterize the behaviour of a gel in terms of the bonds, we must also take the range of these into account, which is defined in the following way. We consider the network

[11] The colloidal gels that form the focus of our study usually have a BDE higher than 4 $k_\mathrm{B}T$ [17]. At the nanoscale, systems with a BDE of ~ 2 $k_\mathrm{B}T$ can form a gel [88].

[12] Roughly speaking, a blood sample is drawn and the rate at which red blood cells sediment is determined [96]. It is generally used as a fast and cheap test to diagnose and monitor inflammatory activity [97].

particles to be spherical with a diameter σ and denote the radial interaction range by R. The range of the bonds is most naturally expressed in terms of the dimensionless variable $\xi = 2(R - \sigma)/\sigma$, the ratio of the attractive to the repulsive range of the interaction.

In systems with long-ranged interactions[13], the kinetics of phase separation are not arrested on any accessible experimental time scales. In this case a transient, continuously coarsening network is formed by the phase separation process of spinodal decomposition [98].

For systems with short-ranged interactions, however, spinodal decomposition is arrested. In this case, the mechanism through which the gel is formed plays an important role in the microstructure of the gel [99]. One such mechanism is an equilibrium process referred to as homogeneous percolation [100, 88], these gels are referred to as equilibrium gels [101]. From a thermodynamic perspective, these gels can be regarded as supercooled[14] liquids [102]. These gels are represented in the left panel of figure 6 and can be found in systems where the number of neighbors a particle can have is limited [103, 104]. An example of such a system is a suspension of patchy colloids [105]. Note that these systems are not in equilibrium, but can be continuously reached from an equilibrium state by increasing the interaction strength[15].

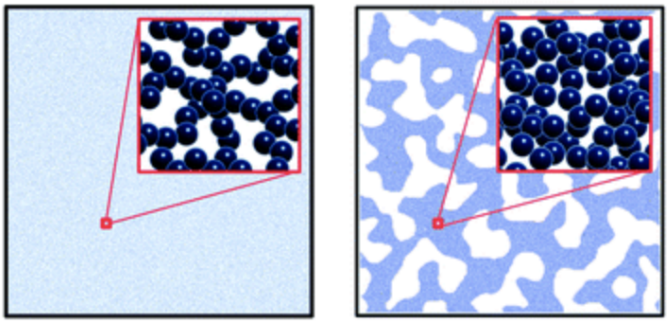

Figure 6: Different mechanisms of gelation lead to gels with a different microstructure. In the left panel, a typical equilibrium gel is depicted. In the right panel, we show a gel that is formed by arrested spinodal decomposition. Image adapted from [106], with permission.

The colloidal system that we study forms a gel through a different mechanism, arrested spinodal phase decomposition [107, 106]. This decomposition is initiated by a *quenching*[16], such that homogeneously distributed colloids suddenly experience an attractive interaction, and heterogeneous clusters start forming. Without quenching, thus gradually increasing interactions, these clusters can compactify and we would again observe a continuous phase

[13]Long-ranged in these systems means that the R has the same order of magnitude as D. In the referenced study, $\xi = 1.2$, rather than $\xi \approx 0.1$ for short-ranged systems.

[14]Supercooling a liquid is the process of lowering the temperature below its freezing point without it becoming a solid. Solidification is prevented by the absence of a seed crystal or nucleus around which a crystal structure can form.

[15]The interaction strength is expressed in terms of $k_{\mathrm{B}}T$, so lowering the temperature is a way of (gradually) increasing the interaction strength. This makes sense, since the bonds compete with collisions whose energy is related to the temperature.

[16]Quenching is a concept in materials science that describes a process where a workpiece is cooled rapidly such that undesirable states are thermodynamically favourable and kinetically accessible in a short window of time. In this case, it means that attractions are increased rapidly (by increasing the polymer concentration) such that the spinodal phase separation becomes kinetically inaccessible since the colloids are trapped in the network.

decomposition. By quenching, the compactifying of clusters is arrested, illustrated in the right panel of figure 6. We conclude that the gel state is in our case reached by a non-equilibrium transition from a fluid-like to a solid-like state, characterized by the sudden arrest of their dynamics.

3.3 Gelation through spinodal phase decomposition

The sudden arrest of dynamics in a colloidal gel is due to crowding or 'jamming', which traps them kinetically [108]. The generality of this process led to a unifying description in terms of a jamming phase diagram [109], see figure 7. It was further postulated that the attractive interactions might jam the system in a way similar to a confining pressure [110]. This implies that the phase behaviour of gelling systems can be described by such a diagram. The concept of jamming is commonly associated with the glass phase, and the network in gels is often described as 'glassy' [111]. There are some clear similarities between these phases. Both are nonergodic disordered systems [112], exhibiting static elasticity, and it can be difficult to distinguish between them experimentally [113]. However, despite their similarities, these are distinct systems. Most importantly, the elastic response of a glass is due to caging effects [114], where a gel's elastic response is due to a percolating network [115]. With these processes in mind, the aforementioned jamming phase diagram was updated to include the regions that are relevant to gelling systems [116], see figure 7. In this figure, two fluid phases have been distinguished, separated by the blue percolation line. On its right, the colloidal particles have a high enough volume fraction and attraction strength to form a network that spans the sample. Without phase separation, however, the dynamics are not arrested, and the network is transient, i.e. continuously changing [117]. If a percolating system is quenched deep enough into the spinodal region, then it (locally) immediately decomposes into high- and low-volume fraction regions, forming the branches of the self-supporting network. The depth of the required quench depends on the point of intersection between the arrested dynamics line and the binodal line, which in turn depends on the specific system. There are system that form a gel directly at the gas-liquid spinodal boundary, which do thus not require a quench [118, 119].

Colloidal systems

Here, we study the process of spinodal phase decomposition in terms of our colloidal system. As before, we study this process in terms of volume fraction and interaction strength. We quantify the interaction strength in terms of the reduced second virial coefficient b_2, as introduced in section 2. In doing so, we can use our model to describe a much wider class of systems[17]. This leads to a natural definition of *effective* interaction strength, $1 - b_2$. This is zero for a purely repulsive hard-core potential, and increases upon increasing interaction strength or range.

In our colloidal system, the interaction between colloids is due to the presence of polymers. These mediate an effective interaction that is commonly referred to as a depletion interaction, which we study in further detail in section 3.4. For now, we observe that the range of these

[17] According to the extended law of corresponding states, the binodals of all particles with a short-ranged attraction collapse onto a single curve in (ϕ, b_2)-space [55].

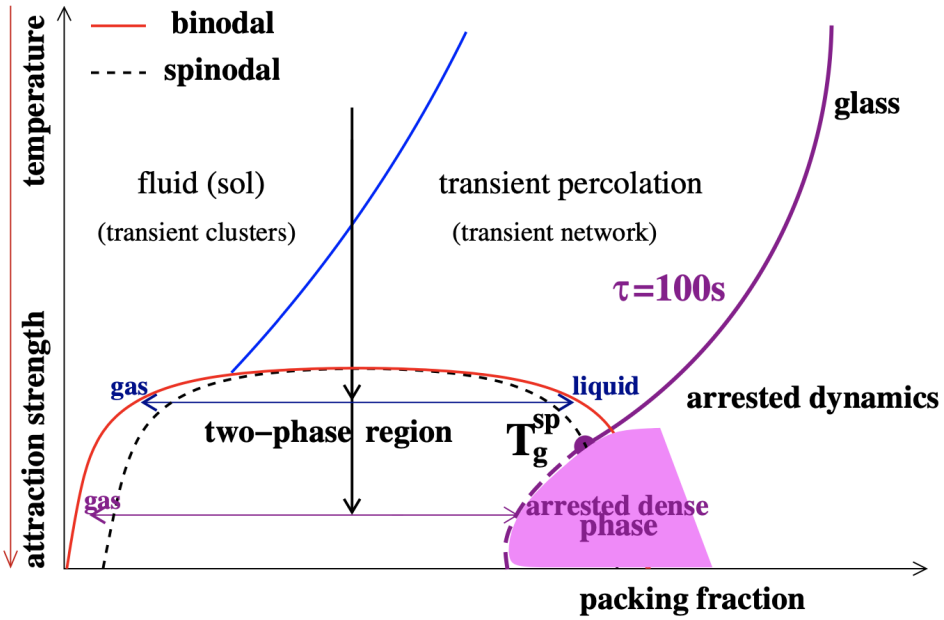

Figure 7: Jamming phase diagram. A fluid phase separates into a gas-liquid coexistence upon increasing interaction strength. Nonergodicity is quantified by a relaxation time of τ, indicated by the purple line. The black vertical arrows indicate an increase in attraction strength, showing that the phase separation dynamics are arrested upon a deep quench. Image reproduced from [93], with permission.

interactions depends on the size of the polymers. We are interested in systems with short-ranged interactions, which is determined by the ratio between colloid and polymer size. This means we will consider relatively large colloidal particles, with $r \sim 1$ µm.

Now we follow Harich *et al.* [17] in their study of the phase behaviour of colloidal suspensions. This results in a jamming phase diagram that resembles figure 7, in terms of the interaction strength $1 - b_2$, thus mirroring the vertical axis. We consider a colloidal suspension with an initially low colloid volume fraction and low interaction strength, compared to $k_B T$. Since the interaction is short-ranged, the colloids behave as a homogeneous fluid (if the system reaches equilibrium). This homogeneous fluid undergoes a phase separation for a given range of volume fractions.

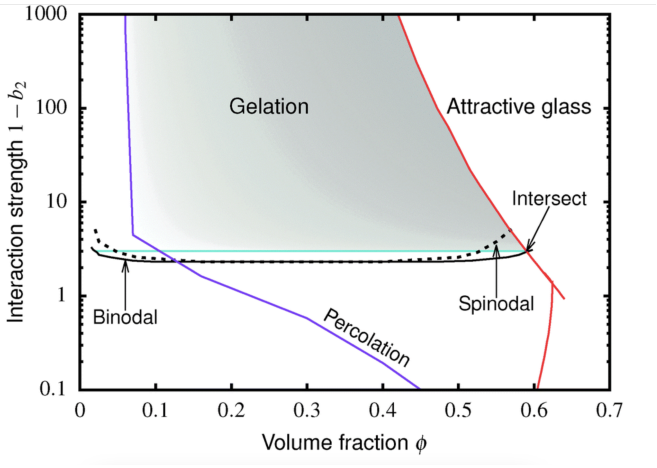

Figure 8: Phase diagram of colloidal suspensions based on theory. The shaded region indicates where a gel is formed. Reproduced from [17], with permission[18].

[18]Published by the Royal Society of Chemistry under a CC BY 3.0 Licence.

Whether this is via nucleation and growth or via spinodal decomposition, depends on the region in the phase diagram. In either region, the ultimate fate of the suspension is phase separation into a dense fluid and dilute gas. However, by quickly increasing the attraction / decreasing the temperature, in the spinodal region, you can cause the BDE to grow so large that clusters do not rearrange much internally. The onset of this process is indicated by the cyan line in figure 8.

In section 3.5, we will discuss this phase diagram in more detail. At this point, we observe that percolation can only occur for sufficiently high volume fractions. Increasing the volume fraction leads to dynamical arrest due to either repulsion (by caging) or attraction (by bonding), depending on the interaction [120, 121]. An unordered solid is formed due to dynamical arrest, which happens on the scale of clusters if the attraction strength is sufficiently high and the volume fraction sufficiently low [122–124]. These arrested clusters and chains of colloids grow and interconnect, leading to an unordered network that spans the sample if the volume fraction is sufficiently high [125–127]. The shaded area in figure 8 corresponds to the conditions under which this happens.

In order to get a feeling of the *actual* bond strengths in the system of interest, we report a few typical values in table 1. In this table, we report the well depth in $k_\mathrm{B}T$ of a square well potential that corresponds to the specified effective interaction strength $1 - b_2$ and well width. We specify the well widths in terms of the diameter D of the colloids. The attractions in the colloidal system are due to a depletion interaction, which we discuss in the following section.

	Effective interaction strength $1 - b_2$				
Well width	0.1	3	5	100	1000
$0.1D$	0.095	1.4	1.8	4.6	6.9
$0.01D$	0.74	3.5	4.0	7.0	9.3

Table 1: Well depths of a square well potential corresponding to the given parameters, expressed in $k_\mathrm{B}T$. The width of the well is expressed in terms of the colloid diameter D.

3.4 The depletion interaction

In the case of non-equilibrium gels, the attraction strength must be increased discontinuously. A discontinuous temperature change is experimentally not feasible on these scales, so a different method is needed. An interaction whose associated BDE can be tuned easily and discontinously is the depletion interaction [25], which we will discuss in further detail below. A typical system with such an interaction is the colloid-polymer mixture, also the most popular system to study gels in general [3].

Following Harich *et al.* [17], we study this model colloidal gel. The system is a colloid-polymer mixture in suspension, comprising colloidal hard-sphere particles and non-absorbing polymers. Due to the presence of polymers, the colloids experience an effective attraction. When the polymers are ideal, this attraction fits the Asakura-Oosawa-Vrij form and derives purely from configurational entropy.

This can be understood as follows. Consider the polymers with a radius of gyration r_g as non-interacting[19] spheres with radius r_g. The colloid-polymer interaction potential is then

$$V(r) = \begin{cases} \infty & \text{if} \quad r < D/2 + r_g \\ 0 & \text{if} \quad r \geq D/2 + r_g \end{cases} \tag{13}$$

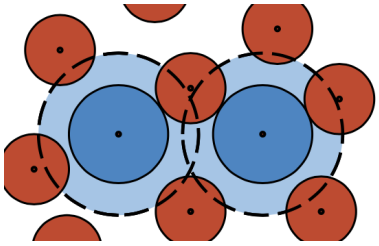

Figure 9: When colloids (dark blue) come close, their excluded volume (light blue) overlaps, such that polymers (red) have an increased free volume.

where r is the center-to-center distance between the colloid and the polymer. This means that there is a region around each colloid, which the polymers unable to occupy and we therefore refer to as an *excluded volume*. The overlap between two of these regions reduces the overall excluded volume in the system, increasing the entropy of the smaller polymer spheres. Following Vrij [128], we introduce a scaled distance $\tilde{r} = r/\overline{\sigma}$, where $\overline{\sigma} = D/2 + r_g$. Since we consider systems in which $r_g \ll D$, the net effect can be studied at the pair level and gives the following interaction potential

$$V(\tilde{r}) = -\frac{4}{3}\pi\overline{\sigma}^3 \left[1 - \frac{3}{4}\tilde{r} + \frac{1}{16}\tilde{r}^3\right] n k_{\mathrm{B}} T \quad \text{if} \quad r_g/\overline{\sigma} \leq \tilde{r} \leq 2, \tag{14}$$

where n is the number density of the polymers. This effective interaction potential is called the depletion potential, and was first described by Asakura and Oosawa in 1954 [129, 130]. The functional form, equation 14, was introduced by Vrij [128] in 1976 and verified experimentally a few years later [131]. The depletion interaction also has energetic contributions, which have been identified theoretically [132] and experimentally [133]. However, these contributions are explained by a nonuniform concentration of polymers (outside the excluded volume). We can assume this to be uniform for a system with a low concentration of ideal polymers with a small ratio of polymer-to-colloid radius $\xi = 2r_g/D$. In this case, the entropic effect dominates the effective interaction [134].

The system studied by Harich *et al.* [17] (as referred to before) contains colloidal particles with diameter $D = 652$ nm, and polymers with radius of gyration $r_g = 21$ nm, such that $\xi = 0.064$, and the depletion potential is an effective *pair*[20] potential, dominated by entropic effects. The strength of the interaction is tuned by adjusting the polymer concentration, typically with a BDE of the order of ten $k_{\mathrm{B}}T$. We stress that this interaction is strong enough to form an elastic network that can sustain itself against gravitational stress for some time that was referred to as the *delay time*[21].

[19] The polymers are considered to be non-interacting amongst themselves, which is a realistic assumption for low concentrations.

[20] We note that the excluded volume overlap may be a three-body effect if multiple colloids come close together such that there is a region where the excluded volumes of these overlap, but some geometry reveals that this requires $\xi \geq 2/\sqrt{3} - 1 \approx 0.154$ [134].

[21] We recall that the shelf life of a product is thus limited by the delay time of the gel, which motivates us to understand the parameters that influence the delay time.

With this interaction in mind, we observe that a quench is experimentally feasible for these systems. This quench corresponds to an instantaneous increase of polymers in the (homogenized) suspension of colloids. This is realized by vortex mixing the suspension after the addition of polymers, thus breaking any bonds that have already formed [135]. This results in a homogeneous system with an increased interaction strength, since it depends on the polymer concentration [136]. This is understood with the visual aid of figure 10. The polymers collide with the colloids from all directions, except if the distance between colloids r is small enough that their excluded volumes overlap. In that case, the polymer collision indicated by the arrows in figure 10 are not compensated, leading to a net force in the direction of r. This force is proportional to the polymer concentration (indicated by n_3 in the figure).

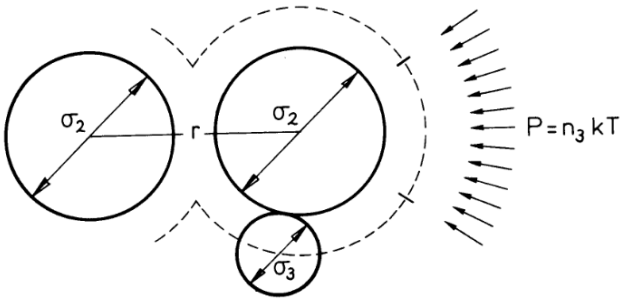

Figure 10: The arrows represent non-compensated pressure on colloids (spheres with radius σ_2) by collisions with polymers (spheres with radius σ_3). The excluded volume is indicated by a dashed line. Image reproduced from [128].

We note that we have studied the interaction between the colloids *only* in terms of polymer-mediated effects. Interactions mediated by the suspending medium, HIs, do not affect the equilibrium structure of the system [60]. However, the system we study is arrested and its relaxation toward equilibrium is slowed down considerably. In this case, HIs can have an influence on the structure, and the specifics of this influence have been studied extensively [61, 65, 57, 35, 62, 63]. Recently, it was found that when gravity does not play a role, the effect of HIs can be captured by a parameter described as the 'structural age'. At corresponding ages, the gel structures that have formed with and without HIs, are indistinguishable [70]. It should be noted that HIs cannot be completely ignored, since lubrication effects were later shown to affect the structure nontrivially [57].

3.5 The collapse of colloidal gels

Our work is not affected by the particular challenges of HIs as discussed above, since the reported effects mostly concern gelation rate and structure of the gel. Our starting point is simply the time point at which the gel is formed, and the structure will be captured in a parameter that corresponds to the strength of the gel. The initial structure is thus a suspension of colloids that have formed a sample-spanning network that is able to support itself by short-ranged attractions. The interparticle bonds may break, allowing the gel to restructure over time [137, 138], often referred to as 'aging'. A dynamic simulation of a comparable system of polydisperse nearly-hard Brownian hard spheres shows that this aging may play an important role in the collapse of gels [21]. The study suggests that the most important underlying process is particle migration and the growing of a capillary-like structural instability of the gel, as was also suggested by Varga *et al.* [23]. Hydrodynamic interactions may widen this pore, allowing the collapse to speed up. Another factor taken into consideration are the

interparticle attractions, producing a negative osmotic pressure[22] that causes the collapse of the gel. A negative osmotic pressure is also found in an attractive glass, where it cannot cause collapse due to steric hindrance; there is no freedom of movement of particles to move closer together. We conclude that collapse happens in case of a negative osmotic pressure at the bottom of the sample, and only when the volume fraction of colloids is low enough to have sufficient freedom of movement.

Harich *et al.* [17] studied the collapse of a colloidal gel under gravitational stress and found three different collapse behaviours for different initial conditions. The conditions that determine the collapse behaviour are colloid volume fraction, polymer volume fraction (which determines the colloid interaction strength through the depletion potential), and the diameter of the colloids [25]. These collapse behaviours are characterized by the time evolution of the gel's *height*, $h(t)$. To illustrate this concept, we consider the network at a local level. The network collapses (locally) when the gravitational stress exceeds the local yield stress of the network. This results in three distinct zones of behaviour: the supernatant, the falling zone, and the consolidating zone. The supernatant zone is the colloid-free region above the network, and the consolidating zone is the region where the local yield stress exceeds the gravitational stress of the network above it. The falling zone is where the network is collapsing, driven by gravitational force and balanced by viscous drag force due to fluid backflow [139].

With these three zones in mind, we can now define the height of the network as the interface between the supernatant and falling zone, leading to the gel's height profile $h(t)$, which is time-dependent. This height profile can be used to determine the characteristic delay time of the collapse and thus separates gels into their stability classes, according to the decay of the height profile [17, 26]. This allows use to distinguish between weak and strong gels. The height profile of a weak gel shows a collapse after a delay time, and strong gels compact slowly [17, 106, 93]. Colloidal gels have a tuneable interaction strength, typically of the order of ten $k_{\mathrm{B}}T$ [85, 125]. As a result of this, their collapse behaviour spans both the weak and strong gel class [17].

In figure 11(a), we see that a colloidal suspension with low interaction strength and colloid volume fraction, represented by the lighter shades of the gelation region in figure 12, sediments immediately. Harich *et al.* [17] explain this by the influence of gravity, they suggest that percolation in real systems happens at higher colloid volume fractions only. This would imply that the network is not space-spanning and thus the fluid backflow that would cause viscous stress if it was space-spanning now goes around the clusters that may have formed. In figure 11(b), where the initial colloid volume fraction is higher, we see an initial quiescent period in which nothing seems to happen (at this scale), after which the network collapses suddenly. In an experimental study that focuses specifically on the processes [27], it was found that two processes happen during the quiescent period. A layer of dense clusters forms at the top of the gel, which eventually fall through the gel, creating pores. At the same time, droplets of suspending medium are formed, creating pores as they move up through the gel. These pores grow until they are large enough to reduce resistance to fluid backflow significantly, leading to the sudden collapse. Another factor that contributes to the collapse

[22] We interpret the osmotic pressure as the minimum pressure difference between the colloid-rich and colloid-poor phase in order to prevent solvent flowing into the colloid-rich region. A negative osmotic pressure therefore indicates that solvent is pushed out of the colloid-rich phase, thus condensing this phase further.

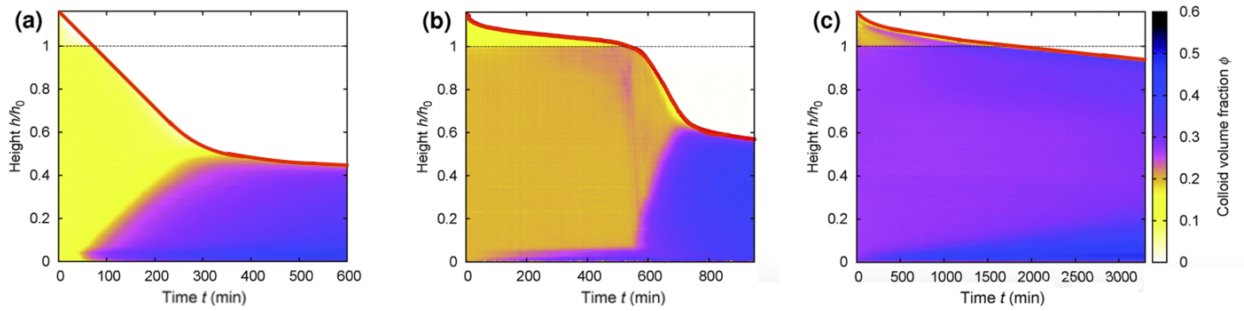

Figure 11: Time evolution of the volume fraction profile, $\phi(z,t)$, with $z = h/h_0$ the normalized height. The color bar on the right indicates the local volume fraction, and the red lines indicate the gel's height $h(t)$. The three different collapse behaviours are shown, and the horizontal dashed line at $z = 1$ indicates the meniscus. Reproduced from [17], with permission from the Royal Society of Chemistry[23].

rate is the negative osmotic pressure of the colloids. In figure C(c), where the initial volume fraction is increased further, the yield stress of the gel is high enough to prevent collapse, and it compactifies instead. This behaviour is observed at volume fractions above $\phi \approx 0.4$, where the freedom of movement of the colloids is presumably reduced enough such that pores cannot be formed.

With these different collapse behaviours in mind, we take another look at the phase diagram of colloidal gels, resulting in figure 12. This figure summarizes the experimental results of the study of Harich *et al.* [17]. We observe that the collapse behaviour of figure 11(a) does not correspond to a gel, since the volume fraction is not high enough to form a percolating network. This is indicated by arrow [2], showing a shift in the theoretical percolation line to the dotted purple line. This shift is motivated by the presence of gravity in real systems. The gravitational stress of a single particle is already larger than the yield stress of systems that lie in regime A in figure 12. The effect of gravity on the forming of gels has received less attention in computational studies, but recently study confirms this assumption. De Graaf *et al.* [141] report a criterion in terms of a critical colloid volume fraction, where buoyancy-driven flows dominate the dynamics rather than the mechanical strength of the forming network. The delayed collapse behaviour as in figure 11(b) corresponds to regime D in figure 12. The slow compactification as illustrated in figure 11(c) corresponds to regime B in figure 12. The red curve indicates the boundary between the glass phase and a dense gel, but regime B seems to extend beyond this boundary. It was suggested [140] that this boundary should be shifted according to arrow [1] for colloidal systems.

We have discussed a large body of experimental work that clearly indicate a delay time before the onset of a sudden collapse. Computationally, a lot of microscale information is available that has helped us to understand a gel's dynamics. However, computational studies have not reported a delay time that is larger than a few seconds. In this thesis project, we aim to build a theoretical model that aids our understanding of the mechanics underlying this delay time.

[24]This article is licensed under a Creative Commons Attribution 3.0 Unported Licence.

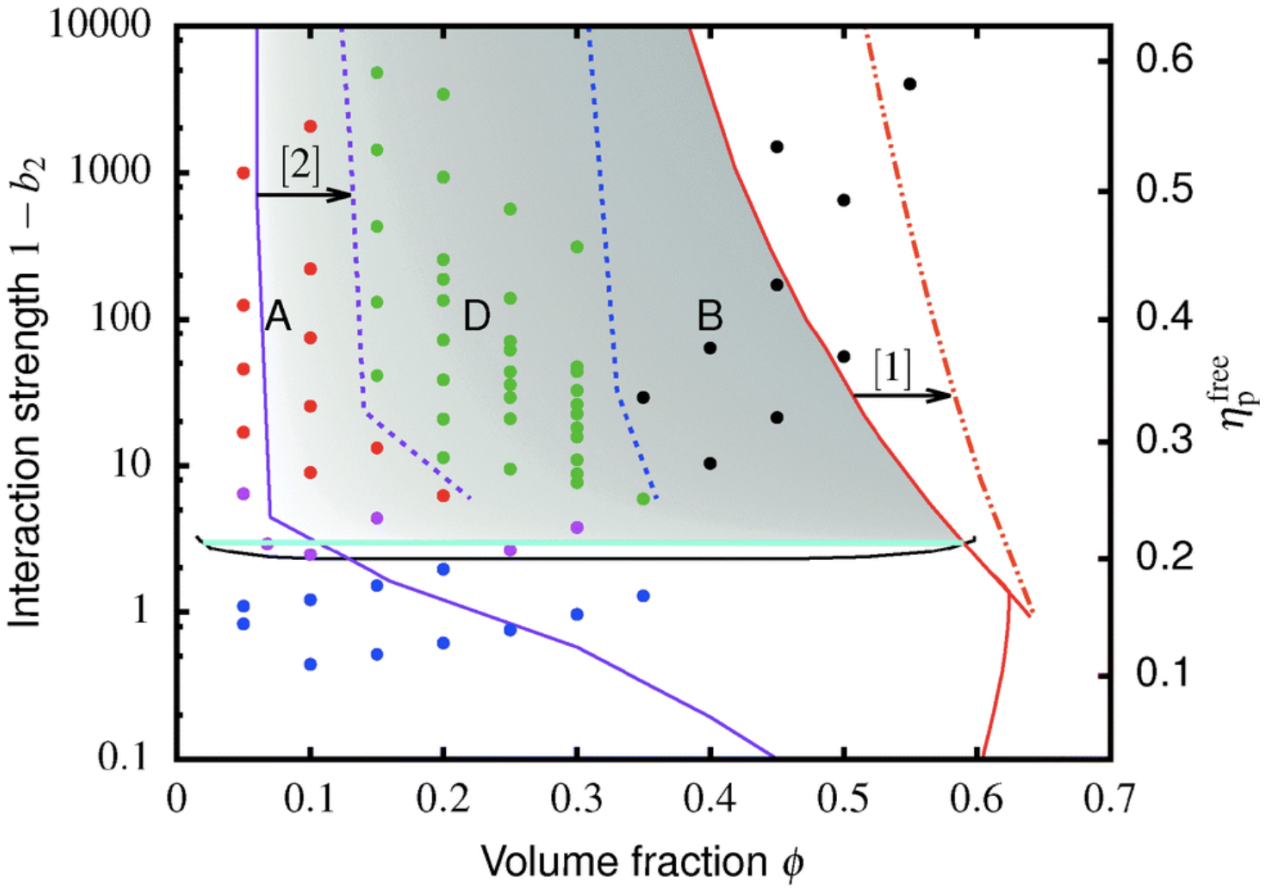

Figure 12: Phase diagram of colloidal suspensions based on experimental results. The black curve is the gas-liquid binodal from simulations, that was obtained using molecular dynamics simulations. The solid purple curve shows the percolation threshold, obtained from Brownian dynamics simulations. The solid red curves indicates where the glass transition takes place, as predicted using mode coupling theory. The cyan line is the tie line where the binodal intersects the glass transition curve. Arrow [1] indicates the proposed shift of the glass transition curve [140], and arrow [2] indicates that gelation does not coincide with the percolation under the influence of gravity. The colored dots correspond to different types of observed systems, where • is a homogeneous fluid, • is a gas-liquid coexistence, and •, • and • are gels with different collapse behaviours, discussed in further detail in section 3.5. Reproduced from [17], with permission from the Royal Society of Chemistry[24].

4 The space-homogeneous model

In this section, we explore the model for gel collapse presented by Darras *et al.* [22], who used it to succesfully capture the process of sedimentation of red blood cells. Note that this model traces its origins back to the poro-elastic model and the work of Manley *et al.* [19]. Red blood cells were experimentally observed to be stable against collapse during a delay time, which was added as a fit parameter in the model. The post-delay collapse can be regarded as an independent process [20], and it is this regime that is described particularly well by Darras' model.

This model balances the gravitational and viscous stresses. The former is due to a density difference between the colloids and solvent, driving the colloids downward, while mass conservation implies that solvent must flow upward (assuming that the colloids have a higher density). The viscous stress is due to the flow of solvent through the network of colloids, and is modeled by the Kozeny-Carman relation, which describes fluid flow through porous media.

4.1 Fluid flow through porous media

We consider the colloids to be a porous medium through which the solvent moves slowly. Following Darras, we choose to model the permeability k of this porous medium by a Kozeny-Carman relationship. This relationship was developed using the assumption that the porous medium can be described as an assembly of capillary tubes in which the Navier-Stokes equations apply [142]. The original work considered fluid flow through soils, and assumes laminar flow in the narrow capillaries [143]. Using Pouseuille's law for laminar flow, the required pressure difference Δp for a flow velocity u through a packed bed[25] of thickness l is

$$\frac{\Delta p}{l} = -\frac{32\mu l'}{D^2 \epsilon l} u. \tag{15}$$

Here, μ is the dynamic viscosity of the fluid, l' the average length of a capillary, D their average diameter, ϵ the void fraction of the packed bed (i.e. the volume fraction that is occupied by the fluid). Note that the velocity u is the superficial[26] velocity of the fluid, which is related to the average velocity of the fluid by $u = \epsilon \overline{u}$. A combination of assumptions and experimental observations allows us to express this as

$$\frac{\Delta p}{l} = -180 \frac{\mu}{d_s^2} \frac{(1-\epsilon)^2}{\epsilon^3} u, \tag{16}$$

where d_s is the diameter of the packing particles[27]. The diversity in porous media is reflected in the many ways that this relation has been reformulated. It did not take long for other models to appear, around the time that Kozeny published his work in Austria, a similar result was reported in England [144]. These relations share the feature that they depend on constants that must be determined through experiment. For example, in this case, the ratio

[25] A packed bed is a pipe that is filled with a packing material, in our case the packing material is the randomly arranged network of colloids.

[27] It was assumed that these are spherical.

of capillary length to the thickness of the bed $l'/l = 2.5$ has been observed experimentally, and is absorbed into the prefactor on the RHS of equation 16.

At the scale of our model, we can treat the the packed bed as homogeneous, and thus the left-hand side of equation 16 can be treated as a pressure gradient $\partial_z p$. Our model relies on a relation between the pressure gradient and the relative velocity of the fluid, but at this point we are interested in the permeability of the porous medium. We state Darcy's law [145] below, and note that this relation holds is valid in the low-Reynolds regime [146].

$$q = -\frac{k}{\mu}\frac{\partial p}{\partial z}. \tag{17}$$

We observe that the volumetric flux q is equal to the superficial velocity u defined above, such that we can derive an expression for the permeability from equation 16, leading to

$$k = \frac{d_s^2\,\epsilon^3}{k_0(1-\epsilon)^2}, \tag{18}$$

where we have absorbed the prefactors into k_0. Since we are interested in the colloidal phase rather than the fluid phase, we rewrite this in terms of the colloidal volume fraction ϕ. Note that we must normalise this volume fraction by ϕ_m, the volume fraction at which the colloidal phase is completely jammed. With this in mind, we substitute $1 - \epsilon = \phi/\phi_m$. Adopting Darras' notation, we have $d_s = a$, the diameter of the colloidal particles. This leads to the permeability of the colloidal phase,

$$k = \frac{a^{\,2}\,(1-\phi/\phi_m)^3}{k_0\,\phi^2}, \tag{19}$$

We note that this relation is semi-empirical, and as such, comes with a range of validity, which will be discussed more in the results subsection. From the aforementioned relationship, we note two important properties of the permeability: k diverges for small values of ϕ, and vanishes for values of ϕ near its maximum ϕ_m. Following Manley *et al.* [19], we use a different version of this relation. Note that it has the same properties as equation 19 at limiting values of ϕ,

$$k(\phi) = \frac{a^2\,(1-\phi/\phi_m)^3}{k_0\,\phi}. \tag{20}$$

This alternative is one of the numerous proposed corrections to the Kozeny-Carman relation [147]. Most importantly, it seems that the microstructure of the media plays a significant role [148, 149]. However, despite using only macroscopic variables and the many proposed corrections, the Kozeny-Carman model describes situations such as flow through packed beds of spheres particularly well [29]. This is also evident from the success of this model to fit experimental data of gravitational gel collapse [24, 19, 22]. We will discuss the permeability in further detail in section 4.4.

4.2 Theoretical framework

In this section, we model the gel as a system that consists of two parts: there is a colloid-poor region, and a colloid-rich region. This model is highly coarse-grained, allowing us to

set the colloid volume fraction ϕ to zero in the colloid-poor region (so it can be treated as a pure Newtonian solvent), and to assume spatial homogeneity in the colloid-rich region. The division into two distinct regions is justified by the assumption that the attraction between colloids suppresses diffusion, leading to a sharp boundary. A sharp, asymptotic boundary is also observed experimentally [24].

Figure 13 shows a diagram representing the experimental setup that is modeled: The initial configuration is a cuvette of height $h_0 = 10$ cm, with an initial volume fraction of colloids ϕ_0 in the range 0.1 to 0.7. The height of the interface decreases under gravitational stress, forming a colloid-free region (indicated as a gray area). In this model, the interface height h and colloid volume fraction ϕ are functions of time only.

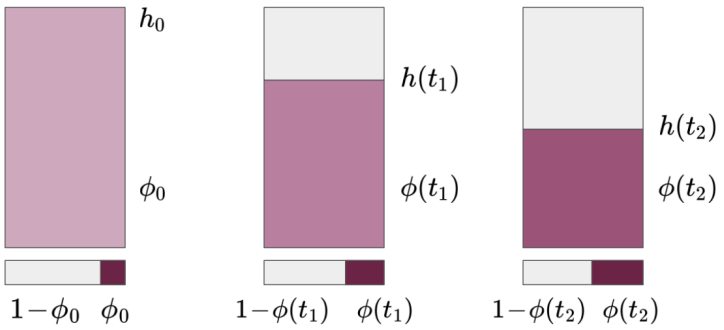

Figure 13: Diagram showing the time evolution of the space homogeneous model where time evolves from left to right. A darker shade indicates a higher colloid volume fraction ϕ, grey indicates colloid-poor regions. The bars at the bottom represent the boundary layer between the colloid-rich and colloid-poor region. In this boundary layer, we indicate the colloid and solvent volume by purple and grey regions, respectively.

If we assume that the horizontal area of the cuvette is A, the volume of the colloid-rich region is $h(t)A$, and volume conservation of the colloids implies that $h(t)A\phi(t)$ is constant. Since we assume that the colloids and solvent have a constant density ρ_c and ρ_s, respectively, this corresponds to mass conservation. We conclude that mass conservation of the colloidal phase implies

$$h(t)\phi(t) = h_0\phi_0. \tag{21}$$

In this simple model, the only external force is gravity, pulling the colloids down (note that we assume a positive buoyant density $\rho_b = \rho_c - \rho_s > 0$), thus increasing the colloid-poor volume. Total volume conservation dictates that an equal volume of solvent particles must cross the interface from the colloid-rich region. We study this in further detail using the representation of the boundary layer at the bottom of each cuvette in figure 13. We set the height of this boundary layer equal to δh, the change of interface height during a time interval δt. Thus if the interface changes height, this corresponds to a volume of $\phi A\delta h$ moving down. Since the colloid-rich phase is homogeneous, the solvent phase occupies the horizontal area $(1-\phi)A$, and moves up with a velocity v (relative to the interface). The upward moving volume of solvent must be equal to the downward moving colloidal volume, such that

$$(1-\phi)Av\delta t = \phi A\delta h. \tag{22}$$

Dividing both by $A\delta t$ and taking the limit $\delta t \to 0$, we find

$$(1-\phi)v = -\phi\frac{dh}{dt}. \tag{23}$$

Now we balance the forces that are involved in this model; the gravitational force must be balanced by a stress gradient, so $\partial\sigma/\partial z = \rho g$. In the absence of colloids, the only contribution to stress is the isotropic response of hydrostatic pressure, $\partial p_0/\partial z = \rho_s g$, where p_0 is the hydrostatic pressure and ρ_s the density of the solvent. This is the equilibrium solution, where the solvent is at rest. The addition of colloids with buoyant density $\rho_b > 0$ increases the gravitational force, which must be balanced by an 'excess stress gradient'. Here we can either follow Darras *et al.* [22] by using the constitutive relation as described by Manley *et al.* [19], $\sigma = \sigma_e - (1-\phi)p$, where σ, σ_e refer to the total and elastic stress. The $(1-\phi)$ factor was included by Manley *et al.* to take into account that only the solvent is driven by the pressure. Instead, we take this into account later and follow Buzzacarro *et al.* [24], using the constitutive relation $\sigma = \sigma_e - p$. The experimentally observed elastic modulus in comparable systems is about two orders of magnitude too small to balance gravitational force with elastic stress [22], so we set $\sigma_e = 0$ in this model. This leads to the equation

$$-\frac{\partial p}{\partial z} = \rho_b g \phi. \tag{24}$$

Treating the colloids as a porous medium through which the solvent moves slowly, we use the reasoning from section 4.1. There, we found the following expression for the permeability k,

$$k(\phi) = k_0^{-1}\, a^2(1-\phi/\phi_m)^3/\phi, \qquad (\text{ 20, repeated})$$

where k_0 is a prefactor that depend on the microstructure of the gel, a is the diameter of the colloidal particles and ϕ_m is the maximum volume fraction of the colloidal phase. In the case of red blood cells, we have $\phi_m \approx 0.86$ [22]. We also recall Darcy's law, which describes the fluid flow through a porous medium in response to a pressure gradient,

$$(1-\phi)\left(v - \frac{dh}{dt}\right) = -\frac{k}{\mu}\frac{\partial p}{\partial z}, \qquad (\text{ 17, repeated})$$

where μ is the viscosity of the fluid and k is the permeability of the porous medium. These relations form a closed set that can be written compactly as below. Note that this becomes an ordinary differential equation using the relation $\phi(t) = \phi_0 h_0/h(t)$, which we will solve analytically. Note that Stokes' law provides an expression for the sedimentation time of a single sphere that has reached terminal velocity, which we denote by $t_s = 9\mu h_0/(2\rho_b g a^2)$. The parameters h_0 and t_s are thus given by the experimental conditions, and k_0 is a free parameter that can be used to fit to experimental data. We combine equations 17, 20, 21, 23 and 24, which leads to

$$\frac{dh}{dt} = -\frac{\rho_b g a^2}{k_0 \mu}(1-\phi/\phi_m)^3 = -\frac{9h_0}{2t_s k_0}(1-\phi/\phi_m)^3. \tag{25}$$

4.3 Analytical solution

We will solve equation 25 analytically below. In order to keep things clear, we absorb all constants into a fit parameter $c = \rho_b g a^2/(k_0 \mu)$, such that $c(1-\phi_0/\phi_m)^3$ is the initial velocity of the interface. Note that $h = \phi_0 h_0/\phi$ such that $\phi_m = \phi_0 h_0/h_m$, where we define h_m as the minimum height of the interface, thus corresponding to the highest volume fraction of the colloidal phase. This results in

$$\frac{dh}{dt} = -c\left(1 - \frac{h_m}{h}\right)^3 = -c\frac{(h-h_m)^3}{h^3}. \tag{26}$$

We split the differential equation in parts that depend only on h or t, and integrate over t:

$$\int \frac{h^3}{(h-h_m)^3}\frac{dh}{dt}dt = \int -c\,dt. \tag{27}$$

We define the function f to be equal to the above, observe that the left-hand side is an integral over h, and change variable to $z = h - h_m$:

$$\begin{aligned} f(z) \equiv \int \frac{(z+h_m)^3}{z^3}dz &= \int 1 + \frac{3h_m}{z} + \frac{3h_m^2}{z^2} + \frac{h_m^3}{z^3}dz, \\ &= z + 3h_m\log(z) - \frac{3h_m^2}{z} - \frac{h_m^3}{2z^2}. \end{aligned} \tag{28}$$

We move the constant of integration to the right-hand side of equation 27, which becomes

$$= -c\,t + C, \tag{29}$$

with C the constant of integration, determined by the initial parameters ϕ_0 and h_0: consider $t = 0$, then $C = f(z_0)$, where $z_0 = h_0 - \phi_0 h_0/\phi_m$ is the initial height above the minimum height. As discussed above equation 25, Stokes' law states that $c = 9h_0/(2k_0 t_s)$. Now we define another function g that depends on the dimensionless variables $z' = z/(\phi_0 h_0)$ and $t' = t/(\phi_0 t_s)$. We substitute these relations into equations 28 and 29 to find

$$\begin{aligned} g(z') \equiv f(z)/(\phi_0 h_0) - 3/\phi_m\log(\phi_0 h_0) &= z' + 3/\phi_m\log(z') - \frac{3}{\phi_m^2 z'} - \frac{1}{2\phi_m^3 z'^2}, \\ &= -\frac{9}{2k_0}t' + C', \end{aligned} \tag{30}$$

where C' is determined as before, giving $C' = g(z' = z_0/(\phi_0 h_0)) = g(z' = 1/\phi_0 - 1/\phi_m)$. This indicates that the process of gel collapse in this model can be described by a master curve that is independent of the initial configuration. It satisfies $g(z') = -9t'/(2k_0) + g(1/\phi_0 - 1/\phi_m)$, where ϕ_0 can be interpreted as a parameter that determines the part of the master curve that describes the corresponding process.

Based on the theory of the gravitational collapse of colloidal gels, we expect qualitatively different collapse behaviours for different initial conditions. However, equation 30 illustrates that this model describes the same process at different times. This requires that k_0 is a

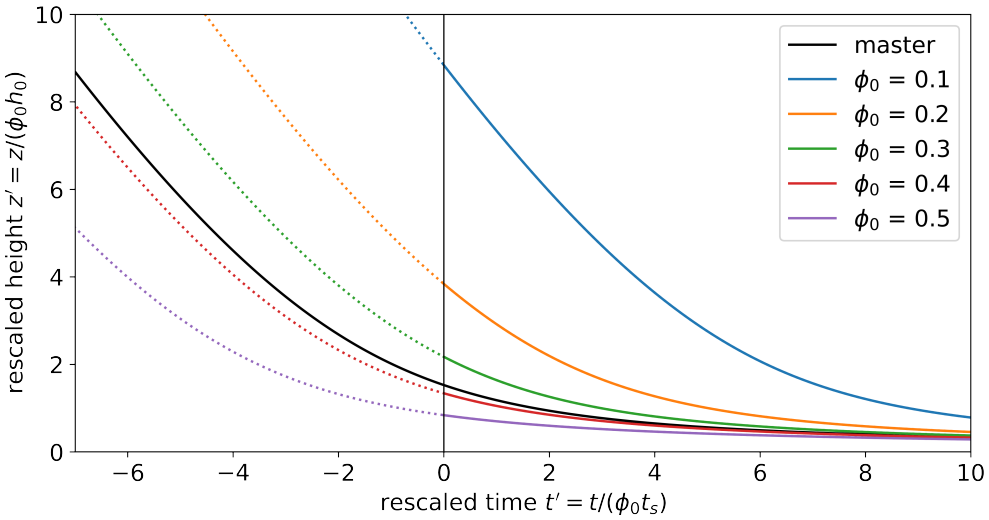

Figure 14: The master curve, i.e. equation 30 with $C' = 0$, represented by the solid black curve. Shifting the master curve to the right by $2k_0C'/9$ represents experimental conditions with ϕ_0 as indicated in the legend. Times before $t = 0$ have no physical meaning. We have set $k_0 = 2$, $\phi_m = 0.86$ and $h_0 = 10$ cm.

constant and that the Kozeny-Carman relation that we used is valid in the range of volume fractions that we study. If this is the case, then once k_0 is determined, equation 30 produces the solid black curve in figure 14, with an offset given by C', leading to the dashed curves. The initial conditions are the cuvette height h_0, the sedimentation time of a single sphere t_s, and the initial colloid volume fraction ϕ_0. The regular time and height are obtained by a few transformations, first shifting the curve by C', according to the initial volume fraction, as shown in figure 14. Then we obtain the regular variables, using the relations $z = z' \cdot (\phi_0 h_0)$ and $t = t' \cdot (\phi_0 t_s)$. Then we take into account that z is the interface height above the minimum h_m by a final shift.

4.4 Results

Since the analytical solution that we found is an inverse function of a result that one would call natural (where height would be given as a function of time), some care needs to be taken in specifying domains, as the maximum values of z and z' depend on ϕ_0, h_0 and ϕ_m. From equation 25, we can conclude that the only relevant parameters are ϕ_0, h_0, t_s, ϕ_m and k_0. In the example of the sedimentation of red blood cells, these parameters are found to be[28] [22].

We reproduce the result as found by Darras *et al.* [22], which corresponds to the red line in figure 15. For lower initial volume fractions of colloids, we see that the interface height falls rapidly until the gel has almost completely collapsed. Higher initial volume fractions seem to

[28]Some of the parameters are provided in supplemental material, which can be found at *https://arxiv.org/pdf/2108.13841.pdf*

[29]Note that Darras *et al.* reported the value of $\gamma = k_0/R^2$, where R is the ratio of the average channel width to the colloid radius a. We have defined our problem in terms of the colloid radius, and accordingly, R^2 is absorbed into our definition of k_0.

Experimental conditions							Fit parameters	
ϕ_0	h_0	t_s	μ	ρ_b	g	a	ϕ_m	k_0
0.45	0.04 m	4.78 hours	1.2 mPa s	80 kg m^{-3}	9.81 m s^{-2}	4 µm	0.86	0.42

Table 2: The parameters that were used by Darras *et al.* [22] to model the sedimentation of red blood cells. Initial colloid volume fractions ranged from 0.15 to 0.45, where the latter was reported to represent a physiological value of red blood cell volume fraction in a blood sample. All experiments were performed using a sample of height h_0, solvent viscosity μ, buoyant density of the colloids ρ_b, gravitational acceleration g and colloid radius a. Using Stokes' law, these parameters correspond to a sedimentation time of t_s. Among their results were the reported values of the maximum packing fraction ϕ_m and permeability k_0[29].

only display slow sedimenting behaviour. This was also observed experimentally [17], so this model seems to predict this outcome correctly, but we must note that these parameters lie outside the range that our model can correctly describe. The problem is that the interface height decreases faster than a sedimenting sphere at terminal velocity would. Since this model only assumes gravitational force to drive the collapse, this is an unphysical result.

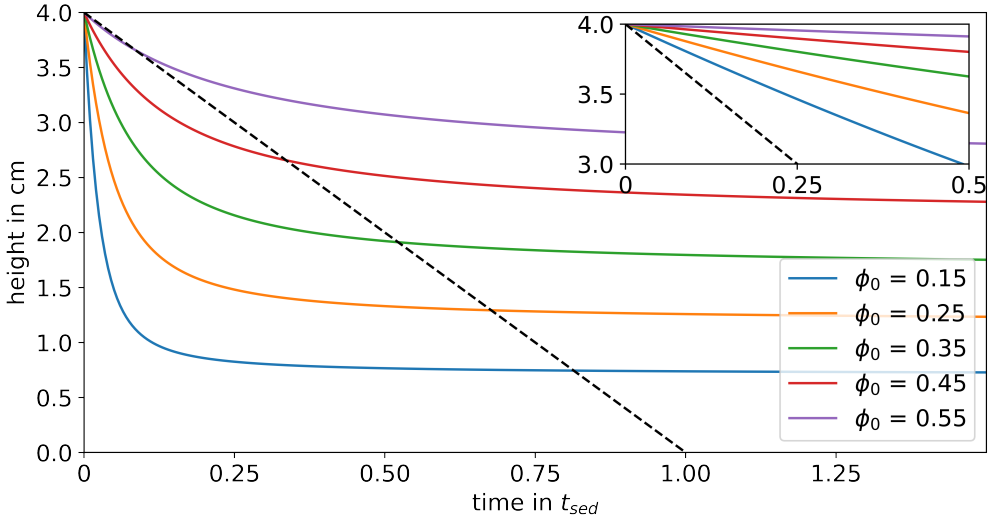

Figure 15: Interface height plotted against time for different initial volume fractions, using the model proposed by Darras [22]. Other parameters are given in table 2. The dashed black line represents a single falling sphere that starts falling at terminal velocity at $t = 0$. We see that the interface drops faster than a single sphere for $\phi_0 < 0.45$. The inset shows the initial behaviour of the model that is described by equation 25 with $k_0 = 9/2$.

We recall equation 25 and observe that we can easily derive an expression for the initial velocity of the interface, as mentioned in section 4.3.

$$\left.\frac{dh}{dt}\right|_{t=0} = -\frac{\rho_b g a^2}{k_0 \mu}(1-\phi_0/\phi_m)^3 = -\frac{9v_s}{2k_0}(1-\phi_0/\phi_m)^3, \tag{31}$$

where we have used v_s to denote the sedimentation velocity of a single colloidal particle.

Since k_0 is an empirical constant, we can exploit this freedom to make sure that the initial velocity of the interface is physical.

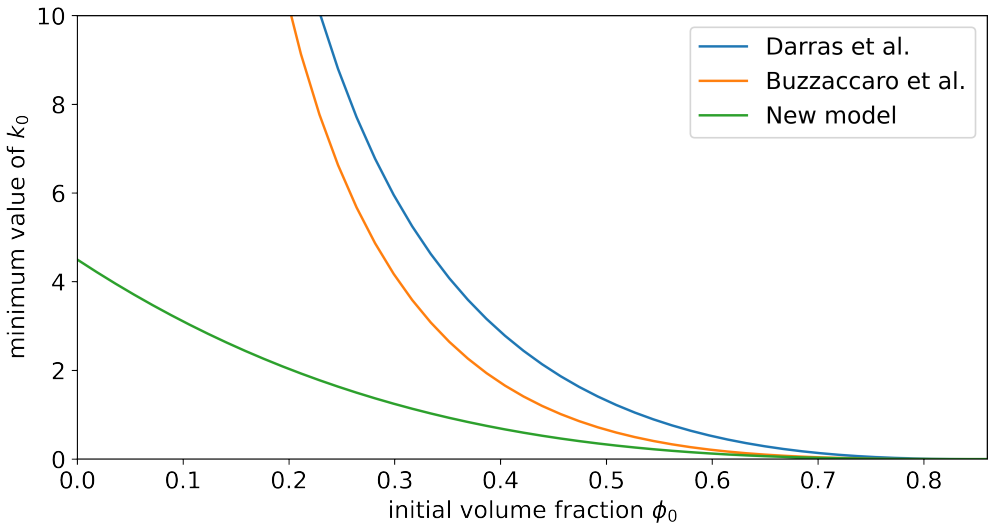

Figure 16: The minimum value of k_0 for the initial velocity of the interface to lie below that of a single sedimenting colloid, plotted against initial colloid volume fraction ϕ_0.

We consider the initial velocity to have a maximum, corresponding to the terminal velocity of a sedimenting sphere under the same conditions (viscosity, colloid diameter, buoyant density, and gravitational acceleration). Equation 31 thus provides a relation between k_0 and ϕ_0, and we can derive similar expressions for each model, which is plotted in figure 16. We see that the choice of constitutive relation (described by the blue and yellow lines) does not affect the outcome much: the minimum value of k_0 diverges as ϕ_0 goes to zero. This limits the range of applicability of this model. Using the Carman-Kozeny relationship of equation 20, however, allows us to describe the full range of initial conditions (meaning $0 < \phi_0 < \phi_m$). This relation leads to the model decribed by relation 25, and is shown in the inset of figure 15. The minimum value of k_0 derived from equation 31 is indicated in green in figure 16, and we see that if $k_0 = 9/2$, then the interface will not drop faster than a single sedimenting sphere. As discussed in section 4.1, it is not straightforward to find an expression for the permeability of porous media. In our case, the porous medium is an out-of-equilibrium network of particles under gravitational stress. We conclude our discussion of this model by the observation that approximating k_0 to be a constant corresponds to ignoring the microstructure of the network. However, if we limit our study of gel collapse to the macroscopic interface height, the space homogeneous model can be used to describe some of the behaviour that is also found experimentally. These behaviours are the fast collapse and the sedimenting phase, but this model is not able to capture the delay of the collapse behaviour. It is important to observe that the fast collapse and sedimenting phase are described by a single equation, while the underlying physics of these phases are completely different.

5 The space-dependent model

We have seen that the space-homogeneous model can model gel collapse macroscopically, but it has its limitations. The most important is that it provides no insight in the physical processes that cause the delay of the collapse. We propose to let ϕ depend on height and time, based on the experimental observation that concentration profiles are height-dependent [17, 150, 27, 24]. Our hypothesis is that the collapse delay is caused by a stress response generated by the colloidal phase. The network can have different stress-bearing properties [151], and we consider viscous, visco-elastic and elastic stresses. The viscous stress modulus of colloidal gels is reported to be smaller than the elastic modulus [152], and the viscous response is dominated by Darcy flow [19]. The elastic response is due to the jammed percolating network [153]. In our system, the attraction that causes the jamming is the depletion interaction [154]. We model this as an effective interaction, the osmotic pressure. It is more difficult to represent visco-elastic stresses due to their complex nature, but some success has recently been achieved [87]

5.1 Osmotic pressure

The osmotic pressure has been claimed to induce the phase separation process that underlies gel formation [21]. While this is not a generally accepted idea, it is worth pursuing the influence it has on the dynamics of the gel. The osmotic pressure Π is often regarded as an excess pressure in a specific type of solution. This solution consist of two containers that are connected by a semipermeable membrane, in one of which the solute is present. For entropic reasons, the solvent has a tendency to move to that container, effectively invoking a pressure difference in the two containers. The osmotic pressure is thus the pressure difference, once equilibrium has been reached [155]. This situation is illustrated in figure 17 to the right.

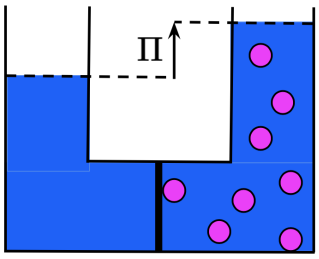

Figure 17: Classical interpretation of osmotic pressure Π. The thick vertical line is a semipermeable membrane and the pink spheres depict solute particles.

In our case, the solute is the colloidal phase, and the solvent is the polymer-liquid mixture. Using Newton's third law, we consider the pressure that the solvent exerts on the colloidal particles. With this frame of reference in mind, figure 17 can be interpreted in the following way. A positive osmotic pressure tends to disperse the colloidal particles, and a negative osmotic pressure tends to push them closer together. Using the methodology of the classical interpretation, we explore a few different ways to express the osmotic pressure.

The following discussion is based on the works of Jacobus Henricus van 't Hoff (1852 - 1911), one of the founders of modern physical chemistry [156]. He expressed the osmotic pressure in the following way,

$$\Pi = iNk_BT/V, \tag{32}$$

where i is the Van 't Hoff index, N the number of solute particles in a volume V. For non-electrolytes dissolved in water, we have that $i \approx 1$ [157]. We observe that equation 32 only holds for low concentrations N/V, and note the similarity to the ideal gas law. In order to capture a larger range of concentrations, Van 't Hoff also proposed a correction to this equation based on a power series in $c = N/V$,

$$\Pi = \Pi_0 + Ac^2, \tag{33}$$

where A is an empirical parameter. We observe the resemblance of this idea to the virial expansion, which we will use later on.

5.1.1 The Van der Waals equation

We continue our discussion with the works of another Dutch Nobel prize laureate, Johannes Diderik van der Waals (1837-1923). In his thesis [158], he proposed a correction to the ideal gas equation of state. If we apply his idea to the osmotic pressure relation above, we find

$$\Pi = \frac{Nk_BT}{(V-b)} - \frac{aN^2}{V^2}, \tag{34}$$

where b takes an excluded volume effect into account, and a describes the strength of attractions. Both parameters are experimentally determinable, substance-specific constants. By the similarity between the depletion potential and molecular attractions (We refer to the similarity between the Morse and depletion potential in figure 3), we use the original expression for b. That is, $b = 2N\sigma^3\pi/3$, where σ is the diameter of the particles, such that the excluded volume is four times that of the volume of the colloidal particles. We study the system in terms of the volume fraction $\phi = \pi\sigma^3 N/(6V)$, such that $b = 4\phi V$. We observe that the osmotic pressure diverges for $\phi \to 0.25$, which is undesirable. In an attempt to consolidate theory with experiment, we redefine $b = \phi V/\phi_m$, such that this behaviour occurs near the maximum volume fraction. Now we express the Van der Waals-type osmotic pressure as

$$\Pi = \frac{6k_BT}{\pi\sigma^3(1-\phi/\phi_m)}\phi - \frac{36}{\pi^2\sigma^6}a\phi^2 \tag{35}$$

We observe that the osmotic pressure can have an unrealistically large negative value for large values of a and $\phi \sim 0.5\phi_m$. More than a hundred alternative equations of state followed [159], each improving Van der Waals' expression in a given range of circumstances [160]. Here, we choose one that allows negative pressure, which is realistic in our case, but is bounded in a reasonable way.

5.1.2 The Dieterici equation

The Dieterici equation is a theoretically based alternative equation of state [161]. The attraction is modeled as a multiplicative factor rather than additive, and the parameter a appears in an exponential. It is given by the following expression,

$$\Pi = \frac{Nk_BT}{V-b}\exp\left[-aN/(k_BTV)\right]. \tag{36}$$

We use the same assumptions as above to define b and rewrite in terms of ϕ,

$$\Pi = \frac{6k_BT\phi}{\pi\sigma^3(1-\phi/\phi_m)} \exp\left[-6a\phi/(\pi\sigma^3 k_BT)\right]. \tag{37}$$

It is worth noting that this can be improved further by replacing the repulsive part of this equation by the Carnahan-Starling equation of state for hard spheres [162]. This does not have a large influence on the magnitude of the pressure, but justifies our choice of b as an approximation to the hard-sphere model. The work of Sadus, which shows that the Dieterici approach leads to more accurate predictions than the Van der Waals approach [162], was challenged by Cachadina *et al.* [163]. Sadus showed their comments to be valid, but to have no significant influence on the predictions [164]. Since we are mostly interested in the order of magnitude of the (osmotic) pressure, we conclude that this model is good enough for our purposes.

5.1.3 Osmotic attractive parameter

In order to study the effect of the osmotic pressure on our system, we must find an expression for the attractive parameter a. We do so by expanding the expressions in terms of the number density $N/V = n = 6\phi/(\pi\sigma^3)$,

$$\Pi = k_BT\left(n + n^2/n_m\right) - an^2 + \mathcal{O}(n^3), \tag{35, expanded}$$

$$\Pi = k_BT\left(n + n^2/n_m\right)\left(1 - an\,/(k_BT)\right) + \mathcal{O}(n^3). \tag{37, expanded}$$

We denote the maximum number density by n_m. These equation are equal up to the second order term. This makes sense, since both expressions are valid in the low-n regime. Also, the virial expansion is useful in the low density regime, and this is what lets us establish a value for the parameter a. For completeness, we write the virial expansion up to the second order term in our variables,

$$\Pi = k_BT\left(n + B_2(\mu,T)n^2 + \mathcal{O}(n^3)\right). \tag{38}$$

Now we can express a in terms of ϕ_m and B_2,

$$a = k_BT(1/n_m - B_2). \tag{39}$$

We recall the definition of B_2,

$$B_2 = -\frac{1}{2}\int d\boldsymbol{r} r^2 \left(\exp\left[-\phi(r)/(k_BT)\right] - 1\right), \tag{40}$$

$$= -2\pi\sigma^3 \int dr^* r^{*2} \left(\exp\left[-\phi(r^*)/(k_BT)\right] - 1\right), \tag{41}$$

where $\phi(r)$ denotes the depletion potential between the colloids, and we defined a dimensionless distance $r^* = r/\sigma$. We can use these relations to predict the value of the attractive parameter a, which we then use to express Π for a larger range of ϕ. We validate this approach by another work of Sadus [165], in which he showed that determining B_2 from the repulsive and attractive parameters, gives accurate predictions [165].

We denote the integral on the right-hand side of equation 41 by $B^* = -B_2/(2\pi\sigma^3)$, and define the dimensionless osmotic attraction parameter $a^* = a/(k_BT\sigma^3) = \pi(1/(6\phi_m) + B^*)$. Table 3 shows a few values in the range of attraction strengths that is typical for our system.

V_0	B^*	a^*
3	0.169	1.35
4	0.849	3.49
5	2.49	8.63
6	6.51	21.3
7	16.6	52.9
8	42.0	133

Table 3: Dimensionless values of the second virial coefficient B^* and osmotic attraction parameter a^*, calculated for different well depths of the depletion potential V_0, expressed in k_BT.

Now we can express the osmotic pressure Π by expression 37, using the values of a as given in table 3. This expression can be interpreted as the stress-strain relationship, where we interpret the volume fraction as a strain. This is because an increase in volume fraction corresponds to a decrease of occupied volume of that phase, thus corresponding to a compression. The resistance of a substance to compression is characterized by the bulk modulus K [166]. It is defined as the ratio of the infinitesimal pressure increase to the resulting relative decrease of the volume, in our case

$$K = \phi \frac{\partial \Pi}{\partial \phi}. \tag{42}$$

However, we will find that the osmotic pressure contributes in terms of the (inverse) osmotic compressibility,

$$\beta = \frac{\partial \Pi}{\partial \phi}. \tag{43}$$

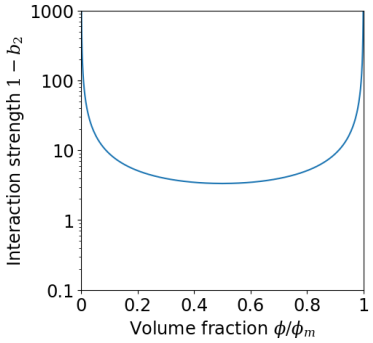

Figure 18: Spinodal line that follows from equation 44.

In figure 19, Π and β are plotted for the Dieterici equation of state for a few typical values of V_0, the well depth of the depletion potential. For comparison, the compressibility predicted by the Van der Waals equation of state is also shown on the right, using dashed lines. The inset shows the agreement in the low-ϕ regime. We also observe a large negative compressibility for intermediate values of ϕ and $V_0 \geq 5k_BT$. We observe that a negative compressibility is unphysical for most ordinary materials [167]. Since the Van der Waals equation of state was developed to model for real gases, we consider it to be invalid in this regime and consider only the Dieterici equation.

Thus, we focus on the results that follow from the Dieterici equation, the full lines in figure 19. We observe that the osmotic pressure is minimized by a phase separation for a certain range of ϕ and V_0, as can be seen from negative slopes in the top left panel.

This phase separation corresponds to the gelation process of arrested phase separation in a certain sense. At low interaction strength, $V_0 = 3$, we observe no phase separation, corresponding to a homogeneous mixture. For intermediate interaction strengths, $V_0 \approx 4$, figure 19 suggests that the osmotic pressure would drive a phase separation. We find the boundaries of the regions of negative compressibility by calculating the zeros of the ϕ-derivative of equation 37. We find that

$$\phi_\pm = \frac{\phi_m}{2}\left(1 \pm \sqrt{1 - \frac{2\pi}{3a^*\phi_m}}\right) = \frac{\phi_m}{2}\left(1 \pm \sqrt{1 - \frac{4}{1 + 6B^*\phi_m}}\right). \tag{44}$$

We can compare these values to the spinodal line in the phase diagram by Harich *et al.*,

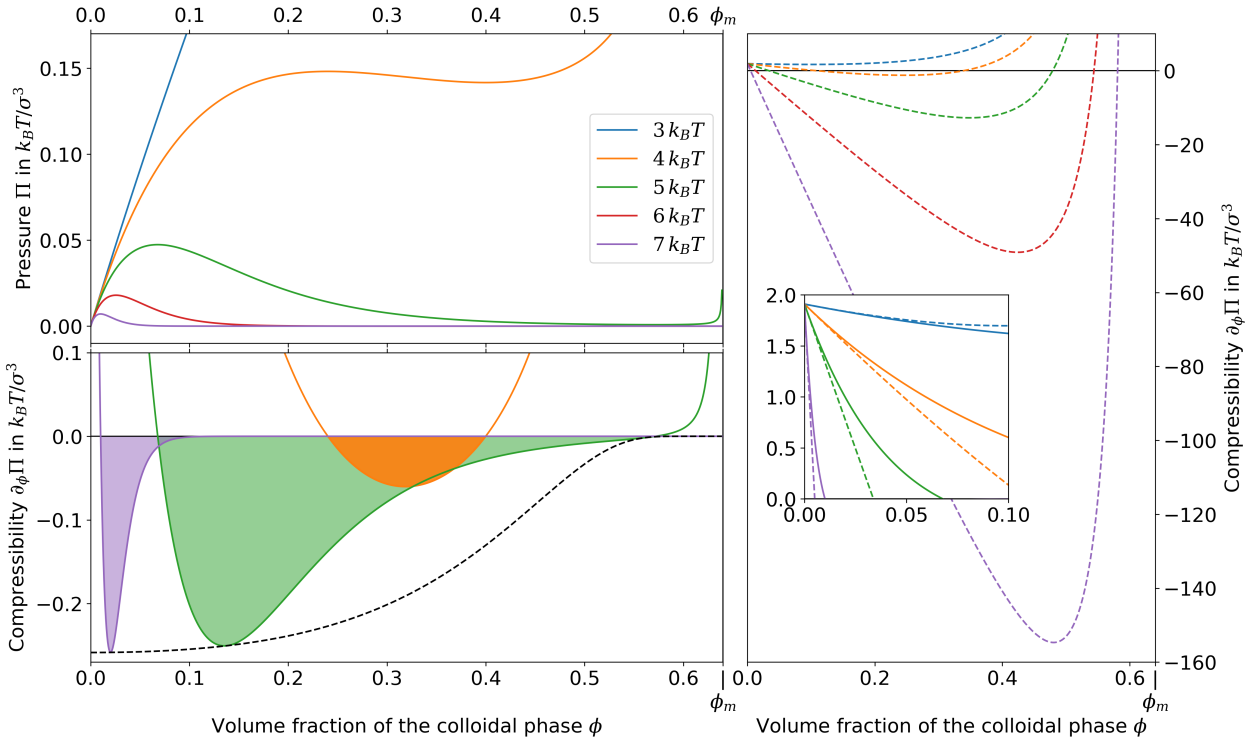

Figure 19: Top left panel: osmotic pressure for different well depths V_0 of the depletion potential, as indicated by the legend. Lower left panel: compressibility corresponding to these pressures, the colored areas corresponds to a negative compressibility, and the dashed black line to its minimum (for any interaction strength). The full lines correspond to the Dieterici equation of state (eq 37). For comparison, those corresponding to the VdW equation (eq 35) are plotted on the right, and the inset show correspondence in the low-ϕ regime.

figure 8. Observing that $1 - b_2 = 1 + 3B^*$, we find a qualitative correspondence between the spinodals, visually supported by figure 18. At higher interaction strength, the osmotic pressure favors a separation into a very dense phase, close to the maximum packing fraction, and a colloid-poor phase. The 'separating strength' as predicted by the osmotic pressure is small, as can be seen from the near-zero value of $\partial_\phi\Pi$ in the intermediate-ϕ range for higher values of V_0. Again, this corresponds to the experimental observation that this phase separation is arrested due to crowding effects. We conclude that the osmotic pressure is a good candidate for explaining the (macroscale) dynamics of a gel. We will discuss its role in further detail after providing additional information on the space-dependent model.

5.2 Theoretical framework

In this section, we present the theory that is used to describe the behaviour of colloidal particles in a Newtonian liquid. We work in the quasi-hydrostatic regime, and use the correspondingly simplified Cauchy momentum equations, see appendix A.2. In order to describe space inhomogeneities, we let ϕ be a function of time t and space z, where z is the vertical distance from the bottom of the sample. Note that we make use of a continuum model, which describes collective behaviour rather than that of a single particle. For example,

when we speak of the colloid velocity, we refer to the average velocity of the colloidal phase in a given unit volume. In our model, a unit volume is a horizontal slice of the sample, with a height that we refer to as *grid size*.

5.2.1 Mass conservation

Similar to the homogeneous model, we consider a binary mixture consisting of a solid colloidal phase and a liquid phase. The volume fraction of the solid phase is again ϕ, and volume conservation implies that we have a liquid volume fraction $\phi_l = 1 - \phi$. The height and time dependence of these variables are implicit to ease the notation. The respective (constant) densities of these phases are ρ_c and ρ_l, and mass is conserved by the following continuity equations,

$$\int_V dV \partial_t \left[\rho_l(1-\phi)\right] = -\int_{\partial V} d\boldsymbol{A} \cdot \left[\rho_l(1-\phi)\boldsymbol{v}_l\right], \tag{45}$$

$$\int_V dV \partial_t \left[\rho_c\phi\right] = -\int_{\partial V} d\boldsymbol{A} \cdot \left[\rho_c\phi\boldsymbol{v}_c\right]. \tag{46}$$

Note that these equations hold for any volume V, but we will apply them to horizontal slices of the sample. Vector quantities are indicated by bold characters, and '$\cdot$' indicates the inner product. The velocities of colloid and liquid phase are indicated by $\boldsymbol{v}_c$ and $\boldsymbol{v}_c$, respectively. Note that the densities[30] of both phases are assumed to be constant, such that equation 46 can be written as

$$\int_V dV \frac{\partial \phi}{\partial t} = -\int_{\partial V} d\boldsymbol{A} \cdot [\phi \boldsymbol{v}_c]. \tag{47}$$

This shows that ϕ only changes in time by flow-mediated flux though the boundaries of the control volume, and thus it is our goal to integrate this equation in time. That leaves us with the task of defining the velocity $\boldsymbol{v}_c$, for which we will need to study the local momentum equations. Taking a closer look at the mass continuity equations provide us with a divergence-free velocity. We recall the divergence theorem,

$$\oint_{\partial V} d\boldsymbol{A} \cdot \boldsymbol{f} = \int_V dV\, \boldsymbol{\nabla} \cdot \boldsymbol{f}, \tag{48}$$

such that adding equations 45 and 46 results in

$$\int_V dV \partial_t\, 1 = -\int_{\partial V} d\boldsymbol{A} \cdot \left[\phi\boldsymbol{v}_c + (1-\phi)\boldsymbol{v}_l\right],$$

$$\int_V dV\, 0 = -\int_V dV\, \boldsymbol{\nabla} \cdot \left[\phi\boldsymbol{v}_c + (1-\phi)\boldsymbol{v}_l\right]. \tag{49}$$

This suggests the definition of a volume-fraction weighted velocity $\boldsymbol{\omega}$ as in equation 50 below. Equation 49 holds for *any* volume V, so we can drop the volume integral, which shows $\boldsymbol{\omega}$ to be divergence-free.

$$\boldsymbol{\omega} = \phi\boldsymbol{v}_c + (1-\phi)\boldsymbol{v}_l \tag{50}$$

$$\boldsymbol{\nabla} \cdot \boldsymbol{\omega} = 0 \tag{51}$$

We note that this simplifies significantly in one spatial dimension, equation 51 implies that $\boldsymbol{\omega}$ is constant (in space). Mass conservation implies the boundary condition[31] $\boldsymbol{\omega}(t,0) = 0$, since colloids and liquid are not able to permeate the bottom. These conditions combined imply $\boldsymbol{\omega}(t,z) = 0$, such that

$$(1-\phi)(\boldsymbol{v}_l - \boldsymbol{v}_c) = -\phi\boldsymbol{v}_c - (1-\phi)\boldsymbol{v}_c = -\boldsymbol{v}_c \tag{52}$$

The careful reader may observe that equation 52 violates Galilean invariance, since a velocity difference is equated to a velocity, which can only hold in a specific reference frame. However, this equation does not need to be Galilean invariant, since the reference frame was fixed by the boundary condition $\boldsymbol{\omega}(t,0) = 0$.

5.2.2 Momentum balance

In order to integrate equation 49 in time, we need an expression for the velocity of the colloidal phase, $\boldsymbol{v}_c$. We express the total density of the mixture as

$$\rho_m(\phi) = \phi\rho_c + (1-\phi)\rho_l = \rho_l + \rho_b\phi, \tag{53}$$

where ρ_b is the buoyant density of the colloidal particles. Using the density as a weighting factor[32], we define the average momentum of the mixture as

$$\boldsymbol{u} = \frac{\rho_c\phi\boldsymbol{v}_c + \rho_l(1-\phi)\boldsymbol{v}_l}{\rho_m(\phi)}. \tag{54}$$

Using the above definitions, we express the momentum balance equation of this system as

$$\frac{d}{dt}\int_V dV\,\rho_m(\phi)\boldsymbol{u} = \int_V dV\,\left(\rho_m(\phi)\boldsymbol{g} + \boldsymbol{\nabla}\cdot\boldsymbol{\sigma}\right), \tag{55}$$

where $\boldsymbol{g}$ is the gravitational acceleration, and $\boldsymbol{\sigma}$ the stress tensor. First we consider the simplified case of a colloid-free system, where $\phi = 0$, in equilibrium, where $d/dt\,\boldsymbol{u} \approx 0$ on the scale we treat the system. In this case, we can neglect the left hand side and we recognise this as the hydrostatic case, where $\boldsymbol{\sigma} = -p\boldsymbol{I}$, with p is the hydrostatic pressure, and $\boldsymbol{I}$ the identity matrix. We say that gravity introduces an external stress, that is redistributed internally according to the divergence of $\boldsymbol{\sigma}$.

In the quasi-hydrostatic limit, the left-hand side of equation 55 can also be neglected, which is discussed in further detail in appendix A.2. However, in this regime, the fluid is not necessarily static, and possible strain must be accounted for in the stress response. This contribution is defined in terms of the rate-of-strain tensor $\boldsymbol{\varepsilon}(\boldsymbol{\nabla u}) = 1/2\left(\boldsymbol{\nabla u} + (\boldsymbol{\nabla u})^{\mathrm{T}}\right)$, with the dynamic viscosity coefficient μ as a prefactor. In appendix A.2, we show that an incompressible fluid does not have other contributions. The gel network also has an

[30] The *mass* densities are constant, not to be confused with a constant volume fraction.

[31] Recall that ϕ, $\boldsymbol{v}_c$ and $\boldsymbol{v}_l$ all have an implicit time- and height-dependence.

[32] It it worth noting that this choice is by no means unique. Other choices of weighting have a different physical interpretation and have different mathematical expressions. However, outcomes with the same physical interpretation are independent of this choice.

explicit contribution to the stress tensor, and we model this as an elastic (non-Newtonian) contribution, the osmotic pressure. This is a ϕ-dependent term that is zero when $\phi = 0$, leading to the following equation

$$\boldsymbol{\nabla} \cdot \boldsymbol{\sigma} \equiv -\boldsymbol{\nabla} p + 2\mu \boldsymbol{\nabla} \cdot \boldsymbol{\varepsilon} + \boldsymbol{\nabla} \Pi(\phi) = -\boldsymbol{\nabla} p + 2\mu \boldsymbol{\nabla} \cdot \boldsymbol{\varepsilon} + \partial_\phi \Pi(\phi) \boldsymbol{\nabla} \phi. \tag{56}$$

We observe that the osmotic pressure does indeed vanish in colloid-free systems. Now we divide equation 55 into the separate contributions of the different phases. We introduce the momentum-exchange terms $\boldsymbol{\Sigma}_{ij}$ between phases $i, j \in \{l, c\}$, where l and c refer to the liquid and colloidal phase, respectively.

$$\frac{d}{dt} \int_V dV \rho_c \phi \boldsymbol{v}_c = \int_V dV \left(\rho_c \phi \boldsymbol{g} + \boldsymbol{\Sigma}_{cc} + \boldsymbol{\Sigma}_{cl} \right) \tag{57}$$

$$\frac{d}{dt} \int_V dV \rho_l (1-\phi) \boldsymbol{v}_l = \int_V dV \left(\rho_l (1-\phi) \boldsymbol{g} + \boldsymbol{\Sigma}_{ll} + \boldsymbol{\Sigma}_{lc} \right) \tag{58}$$

Since we are working within in the quasi-hydrostatic regime, the left-hand sides of these equations can be neglected. Newton's third law states that any momentum that is transferred from phase i to j must be equal to the momentum that phase j receives from phase i, so $\boldsymbol{\Sigma}_{cl} = -\boldsymbol{\Sigma}_{lc}$. Substituting equation 56 into equation 55 and subtracting equations 57 and 58, we identify

$$\boldsymbol{\Sigma}_{ll} = \boldsymbol{\nabla} \cdot (-p\boldsymbol{I} + 2\mu\boldsymbol{\varepsilon}) \quad \text{and} \quad \boldsymbol{\Sigma}_{cc} = \boldsymbol{\nabla} \Pi(\phi). \tag{59}$$

Now we take a closer look at the momentum exchange between the different phases. In section 4.1, we studied fluid flow through porous media, where we found a relation between pressure and fluid flow. We interpret the gradient of this pressure as a force that comes from microscale dynamical friction between the different phases. Darcy's law provides a coarse-grained description of this friction, and we write it in terms of this force,

$$\boldsymbol{F}_D = \mu \frac{(1-\phi)(\boldsymbol{v}_l - \boldsymbol{v}_c)}{k(\phi)}, \tag{60}$$

where μ is the viscosity of the liquid phase. As in section 4.1, $k(\phi)$ is a scalar function that depends on the microstructure of the porous medium, in this case the colloidal phase. Based on the discussion in that section, we write

$$k(\phi) = \frac{\sigma^2}{k_0} \frac{(1-\phi/\phi_m)^3}{\phi}. \tag{61}$$

Recall that k_0 is a scaling constant, σ is the (mean) particle diameter, and ϕ_m the maximum packing fraction of the colloids. We use Darcy's law to model the dynamical friction contribution of the momentum exchange terms, complemented by a hydrostatic contribution, such that

$$\boldsymbol{\Sigma}_{cl} = -\phi \boldsymbol{\nabla} p + \boldsymbol{F}_D. \tag{62}$$

Using this definition, we can remove the hydrostatic contribution from the momentum balance equations. First, we drop the $\boldsymbol{\varepsilon}$, since we are in the quasi-hydrostatic regime, see

appendix A.2. Then, we multiply equation 57 by $(1-\phi)$ and equation 58 by ϕ and subtract the latter from the former. This leads to

$$\boldsymbol{F}_D = -(1-\phi)\left[\phi\rho_b\boldsymbol{g} + \boldsymbol{\nabla}\Pi(\phi)\right] \tag{63}$$

and using equation 60, we write

$$\boldsymbol{v}_c - \boldsymbol{v}_l = \frac{\sigma^2}{k_0\mu\phi}\left(1-\frac{\phi}{\phi_m}\right)^3\left[\rho_b\phi\boldsymbol{g} + \boldsymbol{\nabla}\Pi(\phi)\right] \tag{64}$$

If we consider the case of a single sedimenting colloid, where $\phi \to 0$, we wish to recover Stokes' law, stating that $\boldsymbol{v} = 2\rho_b\sigma^2\boldsymbol{g}/(9\mu)$, where $\boldsymbol{v}$ is the (terminal) velocity difference. This verifies the form of equation 61, and we conclude that $k_0 = 9/2$ in the colloid-free limit. We conclude the theoretical part of this model by the velocity of the colloidal phase, which we find by combining equations 52 and 64.

$$\boldsymbol{v}_c = \frac{(\phi-1)\sigma^2}{k_0\mu\phi}\left(1-\frac{\phi}{\phi_m}\right)^3\left[\rho_b\phi\boldsymbol{g} + \boldsymbol{\nabla}\Pi(\phi)\right] \tag{65}$$

Combining the above with equation 47 leads to the partial differential equation that we want to integrate numerically. Before we discuss the computational challenges of this problem, we compare this to the space homogeneous model.

5.2.3 Comparison to the space homogeneous model

We observe that in the space-dependent model, we treat ϕ as a local variable. In the space homogeneous model, it can be treated as the average of this local variable. This suggest a correspondence between these models, and a way of comparing these is through the interface height, which we will do explicitly in the results section. Another way of comparing these models is to assume space homogeneity in the current model and compare variables that have the same physical interpretation. We will do so below, where we write the space dependence of ϕ explicitly to differentiate between the colloid volume fraction that does and does not depend on space. The assumption of homogeneity implies that $h(t) = \phi_0 h_0/\phi(t)$ again, such that $\dot{h}(t) = -\phi_0 h_0\dot{\phi}(t)/\phi^2(t)$, so we have that

$$\dot{\phi}(z,t) = \begin{cases} 0 & \text{if } z > h(t) \\ \dot{h}(t)\phi^2(t)/(\phi_0 h_0) & \text{if } z \leq h(t) \end{cases} \tag{66}$$

We substitute this into the left-hand side of equation 47 and integrate over the colloid-rich region to find

$$\begin{aligned} \int_V dV \frac{\partial\phi(z,t)}{\partial t} &= h(t)A\dot{h}(t)\phi^2(t)/(\phi_0 h_0) \\ &= A\phi(t)\dot{h}(t), \end{aligned} \tag{67}$$

where A is the horizontal area of the sample. Now we equate this to the right-hand side of equation 47,

$$\begin{aligned} &= -\int_{\partial V} d\boldsymbol{A} \cdot [\phi \boldsymbol{v}_c(z,t)] \\ &= A\phi v_c(h,t), \end{aligned} \tag{68}$$

where the minus sign is canceled by the opposite directions of $\boldsymbol{A}$ and $\boldsymbol{v}_c$. The only nonzero contribution to the surface integral is from the interface, since either $\boldsymbol{A}\cdot\boldsymbol{v}_c = 0$ or $\boldsymbol{v}_c(0,t) = 0$. We conclude that under the assumption of space homogeneity, the velocity of the colloids at the interface is equal to the time derivative of the interface height. The expression for the time derivative of the interface height in the space homogeneous model is equation 25, repeated here for convenience,

$$\dot{h}(t) = -k(\phi)\rho_b g\phi/\mu. \tag{25, repeated}$$

In the space-dependent model, the velocity of the colloids near the interface is expressed by equation 65. Note that $\boldsymbol{\nabla}\Pi(\phi) = 0$ under the assumption that $\boldsymbol{\nabla}\phi = 0$, such that

$$v_c = -(1-\phi)k(\phi)\rho_b g\phi/\mu. \tag{69}$$

We observe that these results differ by a factor $(1-\phi)$, which is still surprisingly close, given the approximations and different approaches. However, the space dependent model is not solvable analytically, as soon as the distribution of colloids is no longer homogeneous. This means that we can calculate the first time step analytically, and from there, we must use numerical methods. Following the idea of Torre *et al.* [87], this will also serve as a method to verify the accuracy of our integration scheme by comparing the analytical and numerical result of the first time step.

5.3 The space-dependent discretization scheme

This introduces vectorial variables, which are typeset in bold, where the size of the vector corresponds to the amount of boxes, and height indicates which box we are referring to. Note that height was defined differently in section 4, where it referred to the height of the interface. Here, we define it to be the distance from the bottom of the sample.

The space-dependent theoretical framework requires an appropriate discretization scheme in order to produce physically realistic results. The appropriateness of the discretization scheme can be expressed in terms of a few conditions. The most important of these are conservativeness, boundedness and transportiveness. Besides these, the *accuracy* is an important characteristic, usually given in terms of the Taylor series truncation error of the approximation (a more detailed discussion can be found in appendix B).

In terms of this study, *conservativeness* corresponds to volume conservation of the colloids[33]. For this reason, we chose to apply an integration scheme that lies in the class of finite volume methods (FVMs). This name of this method refers to a discretization in which the

[33]Note that the total volume is a parameter of our system, such that colloid volume conservation implies solvent volume conservation.

space is divided into small volume elements (or cells) that constitute the mesh of elements on which the equations are solved [168]. This method has been extensively used in several engineering fields, such as fluid mechanics [169], heat and mass transfer [170] or petroleum engineering [171], since it can be used on arbitrary geometries, does not require a structured mesh and leads to robust schemes [172]. Most importantly, numerical fluxes going into a cell is equal to the flux coming out of its neighboring cell along an adjoining boundary. In other words, fluxes through a common face of adjacent control volumes are represented in a consistent manner, which is not in general true for all discretization methods.

The *boundedness* criterion states that (in the absence of sources[34]), the internal nodal values of property ϕ should be bounded by its boundary values. In the current context, this is understood to be a limitation on the local colloid volume fraction, such that $0 < \phi_n < \phi_{\max}$. Realizing that the numerical scheme is a set of algebraic equations, we can express boundedness in terms of these coefficients. An essential requirement for boundedness is that all coefficients have the same sign, with the following physical implication. An increase of ϕ at a given node and time step should result in an increase of ϕ at neighboring nodes at the next time step [173]. The values of the coefficients are determined by the specific problem and the choice of discretization scheme. This means that the boundedness condition limits parameters that define the system, which we will discuss in more detail in appendix C. In the context of our *transient*[35] problem, the boundedness property is generalized to the requirement of *stability*, which means that a solution does not 'blow up', i.e. grow unbounded. In this case, a similar requirement in terms of the coefficients leads to a restriction of the time step size in terms of the grid size, which we will discuss in further detail in section 5.3.3. This condition is not sufficient to guarantee stability, and a more sophisticated mathematical approach called *Von Neumann* stability analysis is required, discussed in more detail in appendix D.

The *transportiveness* requirement can be explained as the ability of the discretization scheme to take the relative influence of nodes into account [174]. Rather than FDMs, where direction is usually taken into account based on a static assumption based on the space variable (where 'up' may be defined as the positive or *forward*[36] direction), FVMs typically take the flow direction into account. This will be discussed in further detail in section 5.3.2.

5.3.1 Finite volume methods

To introduce the finite volume method, we use the visual representation that is claimed to be foundational to its development by the Imperial College group in the 1960s [175], the tank-and-tube model. This analogy relates computational grid points to tanks that are continuously stirred, making sure that ϕ is uniform in each tank. The tanks are connected by tubes that transport the fluid between tanks, representing convective flow, as illustrated in figure 20. In this analogy, diffusive transport is represented by permeable tank walls.

[34] Sources correspond to the creation or destruction of colloids, often used take boundary conditions into account. In our case of non-permeable walls, we do not need sources at all.

[35] Transient or unsteady is the opposite of steady, which is used to describe a system in equilibrium. It is important to note that equilibrium does not imply that the system is static, i.e. nothing happens. An example of a steady system is a solution in a pipe, where the diffusion of a high concentration is balanced by convection through the pipe, such that the concentration profile is constant.

[36] See appendix B for more details

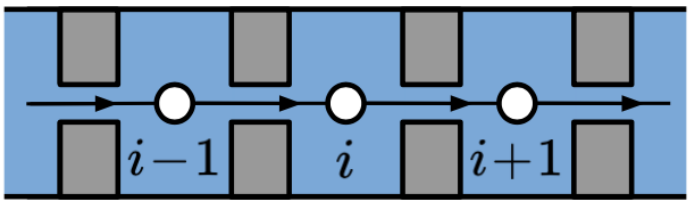

Figure 20: Visual representation of the tank-and-tube model as introduced in 1969 [176].

The mathematical description of the FVM is given below, from which we will see the similarities with this model. The basis of the FVM is to define a local balance equation in terms of divergences, which is to be integrated over the cell volume. This volume integral is converted to a surface integral of fluxes through the cell boundaries using the divergence theorem. Since the flux through a common boundary of adjacent cells is defined in exactly the same way, this method is guaranteed to be conservative.

We give the full derivation of this method of an example problem, general one-dimensional convection, i.e. diffusion-free flow. In section 5.2.2, we will show that the problem of interest is of this category. In our example, we study the general differential equation that describes this problem,

$$\frac{d\phi}{dt} + \frac{df}{dx} = 0, \quad t \geq 0 \tag{70}$$

where ϕ represents the state variable of interest and depends on space x and time t. f is a function of ϕ, and describes the flux of ϕ. Since this is a one-dimensional problem, we discretize space in the following way. We consider ϕ to be a function of the cell average of cell i at time point t, defined as the following line integral,

$$\overline{\phi_i}(t) = \frac{1}{x_{i+} - x_{i-}} \int_{x_{i-}}^{x_{i+}} \phi(x,t)dx \tag{71}$$

where x_{i+} and x_{i-} denote the upper and lower cell boundaries of cell n. By integrating equation 70 with respect to time, we discretize the time evolution of ϕ.

$$\phi(x,t_2) = \phi(x,t_1) + \int_{t_1}^{t_2} \frac{df}{dx}dt \tag{72}$$

Now we integrate this expression over cell i to find a relation between cell averages of ϕ at different times.

$$\begin{aligned}\overline{\phi_i}(t_2) &= \frac{1}{x_{i+} - x_{i-}} \int_{x_{i-}}^{x_{i+}} \left(\phi(x,t_1) + \int_{t_1}^{t_2} \frac{df}{dx}dt\right) dx \\ &= \overline{\phi_i}(t_1) + \frac{1}{x_{i+} - x_{i-}} \int_{x_{i-}}^{x_{i+}} \int_{t_1}^{t_2} \frac{df}{dx}dt\, dx\end{aligned} \tag{73}$$

Now we assume that f is well-behaved in such a way that we can change the order of integration, and we define the cell width of cell i as $\Delta x_n = x_{i+} - x_{i-}$.

$$= \overline{\phi_i}(t_1) + \frac{1}{\Delta x_i} \int_{t_1}^{t_2} \int_{x_{i-}}^{x_{i+}} \frac{df}{dx} dx\, dt$$

In one dimension, we evaluate f at the integration limits. In higher dimensions, we apply the divergence theorem, $\int_V \nabla \cdot f dV = \oint_{\partial V} f \cdot dS$, also reducing the problem to the boundaries of the cells.

$$= \overline{\phi_i}(t_1) + \frac{1}{\Delta x_i} \int_{t_1}^{t_2} f(\phi_{i+}) - f(\phi_{i-}) dt$$

Finally, since ϕ does not change during a time step[37], we assume f to be constant in the time interval $\Delta t = t_2 - t_1$. This leads to the following integration scheme:

$$\overline{\phi_i}(t_2) = \overline{\phi_i}(t_1) + \frac{\Delta t}{\Delta x_i} \left(f(\phi_{i+}) - f(\phi_{i-}) \right) \tag{74}$$

Note that no approximations we made during this derivation, so the solution will be exact in the limit of $\Delta t \to \infty$, however not for the state variable ϕ, but for its cell averages. We note the similarity with the tank-and-tube representation (see figure 20), where f in equation 74 represents the convective flow through a tube. This is a common feature for all integration schemes that belong to the class of FVMs, with some freedom in choosing the flux values at cell boundaries, and this may in fact greatly affect the performance of the algorithm [173]. In convection-diffusion problems, the choice of integration scheme may affect the ability to solve the problem at all [177].

5.3.2 Upwind-biased integration schemes

In appendix C, we study the convection-diffusion problem more thoroughly, providing the theoretical justification of the reasoning in this section. Here, we repeat the governing equation of this problem,

$$\frac{d\phi}{dt} = \frac{d}{dx}(\rho u \phi) - \frac{d}{dx}\left(\Gamma \frac{d\phi}{dx} \right), \tag{75}$$

where we note that our current discussion will be mostly limited to the steady case, in which $\frac{d\phi}{dt} = 0$. Most of the reasoning here applies equally well to the transient case, which we will discuss later on.

[37] Note that this is a physical assumption when time steps are small enough.

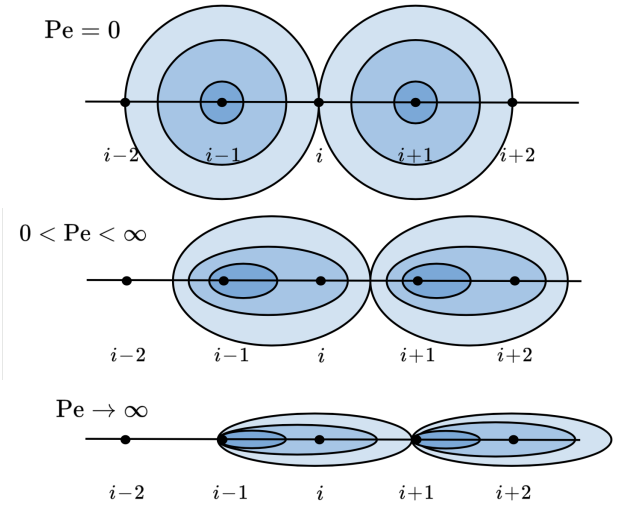

Figure 21: Density distribution in the vicinity of two sources located at grid points $i-1$ and $i+1$, for different Péclet numbers.

The most important parameter in this problem is the Péclet number, which is defined as follows:

$$\mathrm{Pe} = \frac{\text{convective transport rate}}{\text{diffusive transport rate}} = \frac{\rho u}{D}$$

In the case of interest, mass transfer, u is the local flow velocity and $D = \Gamma/L$ the diffusion coefficient in terms of the characteristic length L. For our purposes, the characteristic length is the cell size, which allows us to tune the Péclet number, being limited by the increase of computational cost of decreasing cell size. The Péclet number is an interesting parameter because is it related to the domain of dependence, the 'source cells' that have influence on a given cell.

This concept is illustrated in figure 21. When there is no fluid flow, the only contribution to the mass transport is diffusion, and the concentration profile consists of concentric rings around the source. Upon increasing convective flow, the profiles will become more 'smeared out' in the direction of the flow, which illustrates that the influence of the sources decreases in the 'upstream' cells, and increases in 'downstream' cells. The ability of an integration scheme to take this dependence into account is called the *transportiveness* property.

It is important to note that we have thus far considered the diffusion to have a negligible effect, such that $D \approx 0$, and $\mathrm{Pe} \to \infty$. If the convective flow is uniform with velocity u to the right and $D = 0$, equation 74 applies, and figure 20 illustrates our problem well. The flux $f(\phi_{i+})$ at the boundary between tanks i and $i+1$ is simply $\rho u \phi_i$. This is to be compared to the central difference (CD) scheme, where it is defined as $\rho u(\phi_i + \phi_{i+1})/2$. Looking at figure 21, and considering points $i-1$ and $i+1$ to be neighboring cells with point i their boundary, we see that the CD scheme is a good approximation for low Péclet numbers, and is even exact for $\mathrm{Pe} = 0$, the purely diffusive case. In appendix B, we study how the accuracy of our solution depends on the choice of integration scheme. We find that the CD scheme has a higher accuracy than the upwind-biased difference (UD) scheme, but in appendix C.1, we show that the CD scheme is not bounded for $\mathrm{Pe} > \mathrm{Pe}_c$. These schemes can be combined by determining a critical value of Pe_c above which the UD scheme is used, and the CD scheme below[38] Pe_c, which utilises the favourable properties of both [178]. This idea was further developed to provide the exact solution to the steady-state convection-diffusion problem [179, 173].

[38]Note that the Péclet number becomes negative for convective flow to the left in a completely symmetric way, so this condition actually separates the domains $|\mathrm{Pe}| > \mathrm{Pe}_c$ and $|\mathrm{Pe}| < \mathrm{Pe}_c$

Since our problem is currently diffusion-free, we will use the UD scheme. We can also increase the accuracy of this scheme by incorporating the ϕ values of next-nearest neighbors. For our currently discussion of steady problems, this is pretty straightforward. The increase of accuracy is discussed in appendix B. Here we demonstrate how these schemes define the value of our state variable ϕ at the cell boundaries, ϕ_{i-}, which will in turn define the flux through that boundary, according to $f(\phi_{i-})$ in equation 74. We have already seen that the upwind scheme corresponds to $\phi_{i-} = \phi_{i-1}$, and we will consider the linear upwind difference (LUD) scheme, in which $\phi_{i-} = (-\phi_{i-2} + 3\phi_{i-1})/2$. An even higher accuracy is achieved using the quadratic upstream interpolation for convective kinetics (QUICK) scheme [180], with the definition $\phi_{i-} = (-\phi_{i-2} + 6\phi_{i-1} + 3\phi_i)/8$.
The nomenclature linear and quadratic is illustrated in figure 22, in which the horizontal distance corresponds to the distance on the grid, and the height of vertical lines correspond to the value of ϕ.

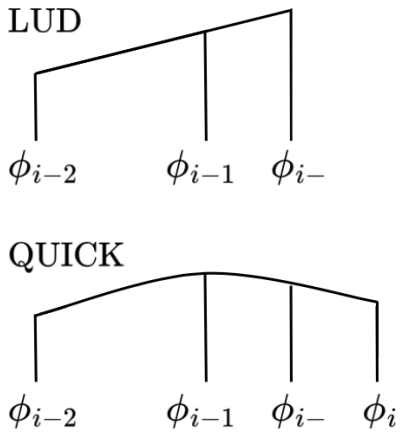

Figure 22: Visual representation of $f(\phi_{i-})$ for the LUD and QUICK scheme. The heights of the vertical lines correspond to ϕ values.

It should be noted that we use a uniform grid, such that cells have equal sizes and boundaries lie exactly in the middle of grid points. Under these conditions, we see that in the LUD scheme, ϕ_{i-} is the linear interpolation of ϕ_{i-1} and ϕ_{i-2}. In the QUICK scheme, we consider the quadratic profile that passes through the three points ϕ_{i-2}, ϕ_{i-1} and ϕ_i, and define ϕ_{i-} as its height at the cell boundary.

We have now seen that the relation between the Péclet number and the domain of dependence can be used to define schemes that meet the transportiveness requirement, independent of the type of flow. This cleared the path to more accurate schemes by considering next-nearest neighbors as well, which have the drawback that they have stability issues under certain conditions, leading to unbounded results [173]. There are methods to overcome these issues for steady problems [181], and many other stable schemes with higher accuracy have been developed without great increase in computational cost [182–186]. We will however not pursue that here, since we are interested in the unsteady problem, which comes with new stability criteria.

5.3.3 The convection-dominated unsteady flow equation

As in the previous section, we attempt to illustrate the reasoning that underlies our choice of integration scheme, with a theoretical justification provided in appendix D. We start our discussion with equation 75 again, but now we do not assume $\frac{d\phi}{dt} = 0$. Instead, we first consider the diffusion-free case, i.e. $\Gamma = 0$, and later on introduce a diffusive term.

Discretizing equation 75 presents us with more options if we do not consider the time derivative of ϕ to be zero. Similar to the space discretization, we can define this derivative in terms of surrounding nodes, with a weighting depending on the problem. Adding time as a dimension, we could follow a similar procedure, but we only consider *explicit*, i.e. time-

forward[39], schemes. The simplest and most natural way to discretize a time step is first-order time-forward. This corresponds to the discretization of a steady problem, where one iteration is replaced by a time step of duration δt. In general, we discretize $\phi(x,t)$ in space and time at cell i and time step n in the following way,

$$\phi_i^n = \frac{1}{\delta x}\int_{x_{i-}}^{x_{i+}} \phi(x,t_n)\,dx. \tag{76}$$

The most important parameter in the current discussion is the Courant-Friedrichs-Lewy (CFL) number $\sigma = a\,\delta t/\delta x$, where a is the convective velocity. In our case, (mass transport, equation 75,) we have that $a = \rho u$. Note that δt and δx refer to computational step sizes. The CFL number is restrained to be smaller[40] than one for most schemes, known as the CFL condition. This condition stems from the Von Neumann analysis of explicit[41] schemes. This analysis is based on a Fourier analysis of the spatial error terms of the numerical solution, providing a thorough method for the analysis of accuracy of numerical schemes. A further explanation and application to several schemes is provided in appendix D.

Even though the Von Neumann analysis is quite mathematical, the CFL condition has a very clear physical interpretation. The real system has a convective velocity a, and thus propagates a distance $a \cdot \delta t$ during each time step. With this in mind, we define the 'domain of influence' as the inverse of the domain of dependence introduced before. This means that the domain of influence of a grid point P is the region containing all grid points that have P in their domain of dependence. The visual representation of this region for a diffusion-free equation is indicated by the light blue area in figure 23. The discretized solution also has a natural velocity that is described well by a domain of influence. This domain is the collection of grid points that are (directly or indirectly) related by the discretized equation. As an example, we consider the scheme that is spatially first order upwind biased, first order time-forward (FOU), which is given by[42]

$$\phi_i^{n+1} = \phi_i^n - a\frac{\delta t}{\delta x}\left(\phi_i^n - \phi_{i-1}^n\right). \tag{77}$$

The domain of influence of this scheme is indicated in red in figure 23.

We see that the CFL condition can be written as a requirement on the mesh ratio $\delta t/\delta x$. This ratio must be chosen such that the domain of influence of the differential equation is contained in that of the discretized equation. This means that the FOU scheme is stable if we choose large enough δx and small enough δt. However, choosing a larger δx results in a larger diffusive error, which is not desirable. Choosing δt smaller results in a longer computation time by the increased number of required iterations. Also, the error grows due to the increased number of iterations. Due to these limitations, first order schemes may give unwanted results, and are even claimed to be useless for convection-dominated problems [187, p. 311]. We note

[39] Explicit or time-forward means that all nodes in the future have a weighting of zero.

[40] Like the Péclet number, the CFL number can also become negative in a completely symmetric way. Note that upwind-biased schemes require that $a > 0$ and thus $\sigma > 0$ for stability.

[41] Note that the less natural alternative, an *implicit* scheme, is often much more stable. This allows larger time steps, but each step is computationally much more expensive. For a system of N nodes, a matrix of dimension N^2 must be inverted for every step.

[42] Note that this corresponds to equation 74 with $f(\phi_{n-}) = a\phi_{n-1}$ and $f(\phi_{n+}) = a\phi_n$.

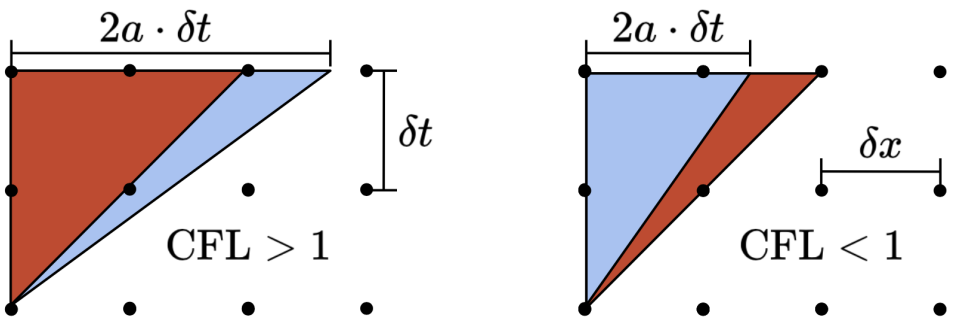

Figure 23: Illustration of the domain of influence of equation 75 with $\rho u = a$, indicated by the blue area. The numerical domain of influence of the FOU scheme is indicated by the red area. The CFL condition is met when the blue domain is contained within the red domain.

that this is not in agreement with the error analysis of steady problems, since the type of error we discuss here can be termed 'overdamping'. For steady problems, this desirably suppresses numerical errors and transients, but in the unsteady case, it creates a numerical diffusion. A solution to this problem lies in higher-order schemes, that typically have a larger 'accuracy region' in terms of δx. A more detailed discussion is given in appendix E.1.

5.3.4 The second-order upwind scheme

Following the discussion above, we present a scheme that has a higher order of accuracy. We have already seen the FOU scheme that is second order accurate in space and upwind-biased, but only first order accurate in time. Due to its historical significance in the field of CFD, we follow the work of Lax and Wendroff [188]. In 1960, they introduced the first scheme with two time levels that is second order accurate in space *and* time. The derivation is based on a Taylor expansion in time up to second order, so we start with

$$\phi_i^{n+1} = \phi_i^n + \delta t \, (\phi_t)_i^n + (\delta t)^2/2 \, (\phi_{tt})_i^n + \mathcal{O}(\delta t^3), \tag{78}$$

where the subscript t indicates a time derivative. The second order accuracy in time comes from the third term on the right hand side. We replace the time derivatives by equivalent spatial derivatives using the differential equation $\phi_t = -a\phi_x$, and for the double time derivative we observe that

$$\phi_{tt} = (-a\phi_x)_t = -a(\phi_t)_x = a^2\phi_{xx}. \tag{79}$$

Using these substitutions, equation 78 is written in terms of spatial derivatives,

$$\phi_i^{n+1} = \phi_i^n - a\delta t \, (\phi_x)_i^n + (a\delta t)^2/2 \, (\phi_{xx})_i^n + \mathcal{O}(\delta t^3). \tag{80}$$

The Lax-Wendroff scheme follows by the substitution of the second-order accurate central definitions of $(\phi_x)_i^n = (\phi_{i+1}^n - \phi_{i-1}^n)/(2\delta x)$ and $(\phi_{xx})_i^n = (\phi_{i+1}^n - 2\phi_i^n + \phi_{i-1}^n)/(\delta x)^2$. We are interested in an upwind-biased scheme, however, and thus use the upwind-biased, second-order accurate definitions

$$(\phi_x)_i^n = (3\phi_i^n - 4\phi_{i-1}^n + \phi_{i-2}^n)/(2\delta x), \tag{81}$$
$$(\phi_{xx})_i^n = (\phi_i^n - 2\phi_{i-1}^n + \phi_{i-2}^n)/\delta x^2. \tag{82}$$

We recall that $\sigma = a\delta t/\delta x$, leading the the following scheme,

$$\phi_i^{n+1} = \phi_i^n - \sigma/2\left(3\,\phi_i^n - 4\,\phi_{i-1}^n + \phi_{i-2}^n\right) + \sigma^2/2\left(\phi_i^n - 2\,\phi_{i-1}^n + \phi_{i-2}^n\right). \tag{83}$$

This scheme is time-forward, upwind biased, and second order accurate in space and time. It is commonly referred to as the second-order upwind biased (SOU) scheme, and was introduced by Warming and Beam in 1976 [189]. Comparing this to the FOU scheme, we conclude that the higher order temporal accuracy is achieved by an additional term that resembles diffusion. Note that the space indices are off when comparing this term to actual diffusion, proportional to the central definition of $(\phi_{xx})_i^n$. Besides the higher order of accuracy, the SOU scheme also has a larger region of stability, expressed by the slightly more lenient CFL condition $\sigma < 2$. The stability analysis that underlies this claim can be found in appendix E. In terms of a FVM scheme, we define the volume fraction at the lower boundary as

$$\phi_{i-}^n = \sigma/2\left(3\,\phi_{i-1}^n - \phi_{i-2}^n\right) - \sigma^2/2\left(\phi_{i-1}^n - \phi_{i-2}^n\right). \tag{84}$$

From the above equation, we clearly see the correspondence with the LUD scheme, with an additional term that ensures second order accuracy in time.

5.3.5 Introducing diffusive terms in upwind biased schemes

In the FOU scheme, equation 77, we can easily implement a diffusive term. Naturally, these depend on $(\phi_{xx})_i^n$, such that we can generally express a diffusive term as

$$\Gamma(\phi_{i+1}^n - 2\phi_i^n + \phi_{i-1}^n)\delta t^2/\delta x^2, \tag{85}$$

where Γ is some parameter that describes the magnitude of the diffusion. From the analysis in appendix E, it follows that this term does not influence the accuracy of the scheme. However, for the SOU scheme, this is not the case. The alternative definition of $(\phi_{xx})_i^n$ as in equation 82 does not provide a solution, as the prefactor is fixed, while we need a free parameter. We choose to model the diffusive term as

$$\Gamma(\phi_{i+1}^n - 3\phi_i^n + 3\phi_{i-1}^n - \phi_{i-2}^n)\delta t^2/\delta x^2, \tag{86}$$

corresponding to $(\phi_x)_{i-}^n = \phi_i^n - 2\phi_{i-1}^n + \phi_{i-2}^n$ in terms of a FVM scheme. In our system, the term that corresponds to actual diffusion is due to the osmotic pressure, such that $\Gamma \propto \partial_\phi \Pi$. In appendix E, we provide a more detailed discussion of implementing diffusive terms without affecting the accuracy of the scheme. We also show that the choice of implementation, together with the magnitude of the diffusion influences the stability of the scheme. It will turn out that stability requires the CFL number σ to be bounded by a parameter that depends on the Péclet number.

5.3.6 Implementation

We have discussed the theory of both the physics and the computation at length, but there is still a gap to bridge. Most of our discussion on the computational part concerned linear schemes, but the velocity of the colloidal phase, equation 65, is clearly not. We overcome this difficulty in the following way. Each time step consist of two steps, of which the first is the computation of the colloidal velocity v_c. We consider this velocity to be constant during each time step, and we observe that it is defined at the centers of the cells. We define the velocity of the colloids at the boundary of neighboring cells in the following way. We regard the cells as tubes through which the colloids move with a velocity given by v_c. The weighted velocity is then given by $(\phi_1 v_c(\phi_1) + \phi_2 v_c(\phi_2))/(\phi_1 + \phi_2)$. Using this velocity, we apply our discretization techniques to equation 47 in order to numerically integrate the colloidal volume fraction in time. Since this equation is linear in ϕ, we can use the integration schemes that we have discussed in this section. It is important to observe that σ is now space-dependent and defined as $v_c \delta t/\delta x$.

In order to keep track of the interface height, we define a threshold volume fraction below which we consider a cell to contain no gel network. After each time step, we compare ϕ in the cells below the interface to this threshold and update the interface height accordingly.

5.4 Results

In this section, we present the results of the numerical computations that we performed, using the different models as discussed in the previous sections. Before we discuss these results, we take a closer look at the role of the osmotic pressure in our model.

5.4.1 Osmotic pressure

When we limit the spatial dependence to one dimension, our model is described by equation 65, repeated here for convenience.

$$\boldsymbol{v}_c = \frac{(\phi-1)\sigma^2}{k_0 \mu \phi}\left(1-\frac{\phi}{\phi_m}\right)^3 [\rho_b \phi \boldsymbol{g} + \boldsymbol{\nabla}\Pi(\phi)] \qquad \text{(65, repeated)}$$

From this equation, it is readily observed that we have two contributions that determine the dynamics of our system, the first of which is an external gravitational stress. This stress is partially internally redistributed by osmotic pressure and the remainder causes relative flow of the suspending liquid. We are interested in the magnitude of the osmotic stress, compared to the gravitational stress.

The first term in the square brackets of equation 64 is of the order of $10^4\,\mathrm{kgm^{-2}s^{-2}}$. The second term is equal to $\partial_\phi \Pi \boldsymbol{\nabla}\phi$, where $\boldsymbol{\nabla}\phi$ is of the order of one. From figure 19, we observe that the magnitude of the osmotic energy density $\partial_\phi \Pi$ is of the order of $k_B T/\sigma^3$. In our system, we have that $T \approx 300\,\mathrm{K}$ and $\sigma \approx 10^{-6}$, such that $k_B T/\sigma^3 \approx 4 \times 10^{-3}\,\mathrm{kgm^{-2}s^{-2}}$. Since the stress contribution of the osmotic pressure is seven orders of magnitude smaller than that of the gravitational stress, we expect this to have a negligible role in the dynamics of a gel.

It is worth noting that the osmotic energy density diverges near ϕ_m, which would ensure that $\phi(z,t) < \phi_m$. We will observe peaks of local colloid volume fraction in that range, so

the osmotic pressure may play a role in explaining the dynamics in that range. Also, there is experimental evidence for dense clusters, so these peaks are physical results. However, these clusters are reported to have a colloid volume fraction of $\sim 1.1\phi_0$ [27, 18], much lower than ϕ_m.

We conclude that the osmotic pressure is expected to have a negligible effect on the dynamics of a real gel, of which ϕ is bounded well below ϕ_m. Te verify this claim, we numerically integrated equation 47 for a few initial conditions in the range $\phi_0 \in [0.1, 0.5]$. We expressed $\boldsymbol{v}_c$ by equation 65 and used the FOU scheme, in which diffusive terms are easily implemented, with and without an osmotic contribution to the stress. The divergence of the osmotic energy density was modeled as $\partial_\phi \Pi(\phi) = 10^8$ for $\phi - \phi_m < 10^{-15}$, since $\partial_\phi \Pi(\phi_m < 10^{-15}) \approx 10^8$, with $V_0 = 6$. We integrated over 5×10^6 time steps, approximately 14 real hours, and saved the volume fraction profile $\phi(z)_t$ each 10^5 time steps.

Visually, no differences were detectable in the local volume fraction, when plotted against height at different time steps. Comparing the numerical values of a few macroscopic variables that we calculate from $\phi(z)_t$, we found that the differences are indeed negligible. We denote the average volume fraction by ϕ_{av} and use superscripts in and ex to denote including and excluding osmotic effects, respectively. Note that we expect $\phi_{\text{av}}^{in,ex} \approx \phi_0$, since otherwise the scheme is not conservative. We find that $(\phi_{\text{av}}^{in,ex} - \phi_0)/\phi_0 < 10^{-8}$, as expected. Then we compare the maximum local volume fraction, $\phi_{\max}$, which we expect to be bounded by ϕ_m. We find that $|\phi_{\max}^{in} - \phi_{\max}^{ex}|/\phi_m < 10^{-4}$, and observe that these deviations are damped. We conclude that the osmotic pressure has a very small effect on the dynamics of our model of gel collapse, and expect that the influence on the dynamics of a real gel is negligible.

During our observations, we found that $\phi_{\max}^{in,ex}$ exceeds ϕ_m, up to about 20%. Our model does not provide a physical explanation for the peaks exceeding ϕ_m. We conclude that either the integration scheme is not bounded, or the theoretical model is missing an element. We will come back to this point in section 6.

5.4.2 Volume fraction profiles

In our study of the collapse of colloidal gels, we choose to use typical values as given in table 4. Our numerical units are chosen such that the parameters that appear in our computations have values close to one. Our numerical units are $M = 10^{-6}$ kg, $L = 10^{-3}$ m, and $T = 10^2 s$. In order to study the time evolution of a collapsing gel, we plot the volume fraction profile of

ρ_b	g	σ	μ	k_0	v_s
$10^3\,\text{kg/m}^3$	$10\,\text{m/s}^2$	$10^{-6}\,\text{m}$	$10^{-3}\,\text{Pa s}$	1	$10^{-5}\,\text{m/s}$

Table 4: Typical values of parameters for a colloidal gel. The simulation units were chosen such that the resulting settling velocity v_s in those units is one.

the colloidal phase at a number of time steps. Doing so, we see the following typical behaviour. Initially, the colloidal phase is homogeneous throughout the sample, and detaches from the top of the sample under gravitational stress. The bulk of the gel settles freely, such that an observer at rest with respect to this part of the gel would not observe anything except for a constant fluid flow through the pores. At the bottom, this freely settling part forms a

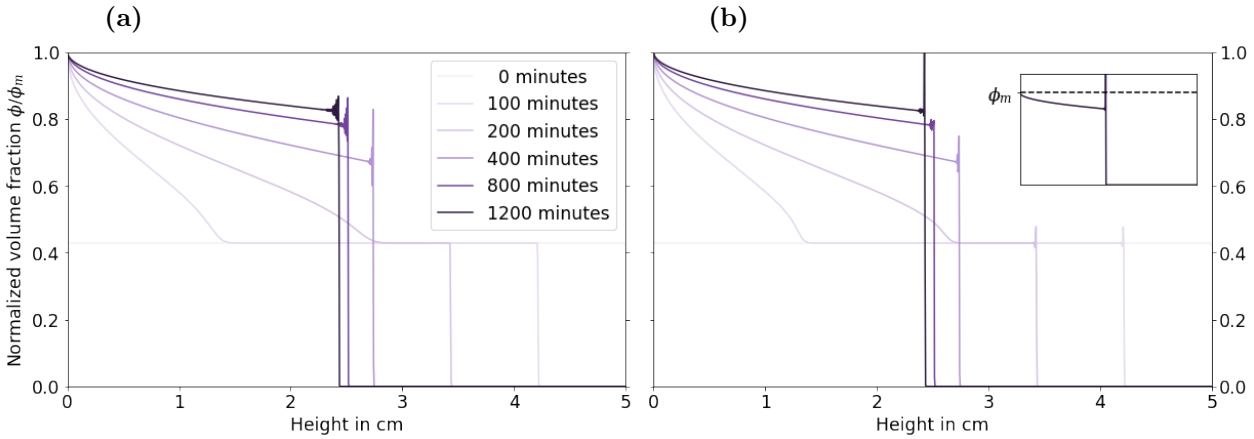

Figure 24: The volume fraction profile $\phi(z,t)$ plotted against height z at different times, as indicated in the legend. This figure shows a setup with initial homogeneous volume fraction $\phi_0 = 0.3$. Note that the peaks at the top of the gel can exceed the maximum volume fraction ϕ_m (not shown here). a) Using the FOU scheme, there are no visible peaks at the top of the freely settling bulk. Once this phase has completely collapsed into the compacting regime, large peaks appear near the gel-supernatant interface. b) Using the SOU scheme, we observe a peak at the top of the freely settling bulk. Once this phase has completely collapsed into the compacting regime, the peaks appear smaller than those produced by the FOU scheme. However, the inset shows that this scheme also produces unrealistic peaks, i.e. $\phi > \phi_m$.

region of higher volume fraction. The compacting region at the bottom grows as the packing fraction grows closer to its maximum value ϕ_m, and the top of the gel moves down with the velocity of the freely settling bulk. The freely settling bulk thus becomes smaller and eventually disappears. This process can be thought of as a building that collapses after the walls suddenly lose their ability to support the structure. After this relatively fast collapse, the system now consists of a dense, compacting gel and a supernatant region. This process is illustrated in figure 24, for two different integration schemes. In both cases, the initial configuration of $\phi_0 = 0.3$ is indicated by a very light horizontal line, since the colloids are initially distributed homogeneously. At increasing times, i.e. darker lines, we see that the freely settling part of constant ϕ collapses into a dense, compacting phase.

In the following discussion, we will use the shorthand 'interface' to refer to the interface of the colloid-rich and colloid-poor phase. At that point, the most interesting behaviour seems to happen, the forming of a dense layer. Using the FOU scheme, this is mostly suppressed until the freely settling part has collapsed into the compacting region. When the initial volume fraction ϕ_0 is high enough, that is $\phi_0/\phi_m \approx 0.5$, peaks can be observed instanteneously. Using the SOU scheme, we observe peaks at the interface instantaneously, when $\phi_0/\phi_m \gtrsim 0.3$.

5.4.3 Volume fraction peaks

At this point, it is not clear whether the peaks in volume fraction are numerical defects or physical effects. In appendix D.2, we saw that the using the FOU scheme tends to numerically diffuse results. If the peaks show up naturally when using this scheme, this would support the claim that these peaks are not defects. We study the origin of these peaks by zooming in

and using a much finer grid, corresponding to 10^{-7} m, and reduce the time step size to 10^{-3} s in order to meet the CFL requirement. We also keep track of the fluxes across the boundaries of adjoining cells in order to find out how these peaks grow. We define the colloidal flux $\boldsymbol{J}_c$ as

$$\boldsymbol{J}_c(\phi) = \phi \boldsymbol{v}_c \models \frac{-(1-\phi)\sigma^2}{k_0 \mu} \left(1 - \frac{\phi}{\phi_m}\right)^3 \rho_b \phi \boldsymbol{g}, \tag{87}$$

where we used $\models$ to indicate that equality only holds when gradients are negligible. This is because the values of ϕ and $\boldsymbol{v}_c$ at boundaries of the boxes are computed according to a numerical scheme. When gradients are negligible, all numerical schemes should reduce to the equation above (and they do).

This also allows us to qualitatively discuss the origin of the peaks at the interface. Assuming that approximation 87 holds, we can plot the local flux as a function of ϕ, see figure 25. We have given the local (volume) flux in terms of the bare gravitational velocity

$$v_b = \frac{\sigma^2 \rho_b g}{k_0 \mu}, \tag{88}$$

corresponding to the velocity of colloids in a suspending medium where $\phi \approx 0$. Note that a volume flux has units of velocity, thus we can express it in terms of the bare gravitational velocity v_b.

In order to explain the origin of the volume fraction peaks, we consider an example. We start with a homogeneous mixture with a colloidal volume fraction $\phi_0 = 0.4$. As gravity starts to empty the top cell, its volume fraction decreases, and the flux across its boundary starts to increase. In the cell below, the flux coming in thus exceeds the flux going out, increasing the local volume fraction. This increase reduces the outgoing flux, and thus a peak grows until the fluxes are balanced again. This implies that the top cell is emptied out far enough, corresponding to the left side of the peak in figure 25. Based on this, we would expect peaks to occur when $\phi_0 \gtrsim \phi_m/3$. We recall that the SOU scheme produces visible peaks near the interface when ϕ_0 is larger than approximately $0.15\phi_m$. The FOU scheme damps these peaks for lower volume fractions, but they show when $\phi_0 \gtrsim \phi_m/2$. We conclude that the origin of these peaks lies in the theoretical framework, and that these are highlighted or suppressed, depending on the choice of numerical scheme.

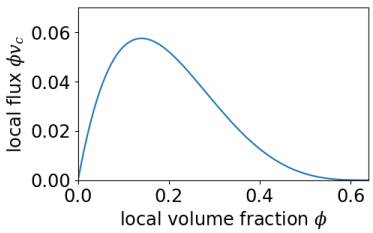

Figure 25: Plot of $\boldsymbol{J}_c$, expressed in terms of v_b.

In our computations, we keep track of the *actual* flux, which depends on the numerical scheme that is used. We normalise this by the 'bare gravitational flux' $\boldsymbol{J}_g = \boldsymbol{J}_c(\phi_0)$. This is the amount of colloids that moves across the boundaries of the boxes if the colloids occupy a volume fraction ϕ_0. Thus we expect that the actual flux of colloids $\boldsymbol{J}_c = \phi \boldsymbol{v}_c$ is close to $\boldsymbol{J}_g$ initially, and eventually decreases as the volume fraction decreases. Depending on ϕ_0, there may be an initial increase in $\boldsymbol{J}_c$. In figure 26, we see the first few time steps of the numerical integration, plotted at time intervals of 60 ms.

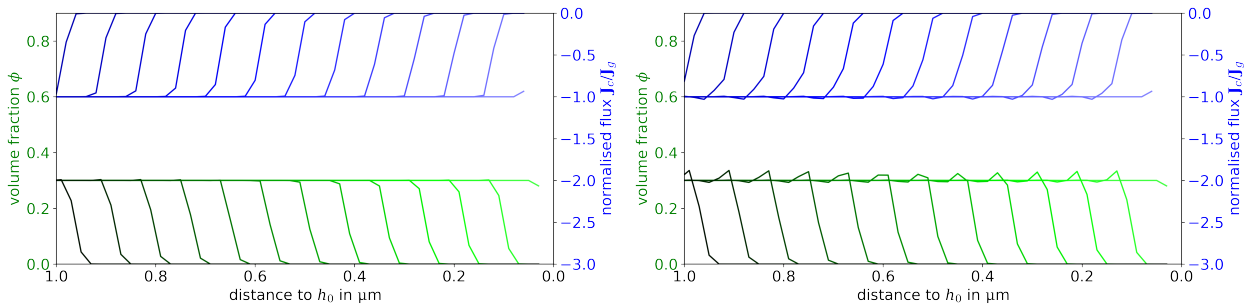

Figure 26: Initial collapse behaviour, where darker colors correspond to later times, at intervals of 60 ms. The colloidal volume fraction is shown in green, and is defined at the centers of cells. The normalised flux is shown in blue, and is defined at the boundaries of the cells, hence the offset. a) The FOU scheme does (eventually) produce a peak at the interface, evidenced by the slight bump in the four darkest green lines. b) The SOU scheme shows a much more pronounced peak, and is also clearly visible in terms of the normalised flux.

5.4.4 Time evolution of the interface

From the volume fraction profiles, we can determine the height of the interface at each time step. That way, we can compare the results of this model to the space-homogeneous model. Also, we compare the time evolution of the interface height to experimental results, such as the work of Harich *et al.* [17]. In order to determine the height of the interface, we can choose to define it as the lowest grid point where ϕ is lower than some cutoff value c. We define $\phi_{\text{cut}} = c\phi_0$, with some constant $c \in [0, 0.5]$. This range of c is justified by the steep decline of ϕ at the interface, as can be seen in figure 24. Here, we let $c = 0$, $k_0 = 1$ and $\phi_m = 0.7$, and keep track of the interface height for different initial volume fractions ϕ_0. The resulting data is plotted in figure 27 as full lines. For comparison, we have repeated the results from the space homogeneous model with the same parameters as dotted lines with corresponding colors. In the left panel, we observe a qualitative correspondence of the different models. However, there is a sharper transition between the fast collapse and sedimenting regime in the space-dependent model. It is important to obbserve that this transition is still smooth.

Also, the progression of the interface in the space-dependent model is linear in time, with a slope equal to $\boldsymbol{v}_c$. Taking a closer look at the initial behaviour, shown in the panel on the right, we observe a delay time of ~ 5 minutes, which increases with ϕ_0. Another important observation is that the interface height may drop below the theoretical minimum h_m, which can be explained by the peaks in volume fraction. These peaks allow an unphysically large amount of colloids to reside in the bottom of the sample, thus occupying less space than physically possible. Since the width of these peaks seems to be constant, they have a larger relative influence when the total amount is smaller (corresponding to a lower ϕ_0).

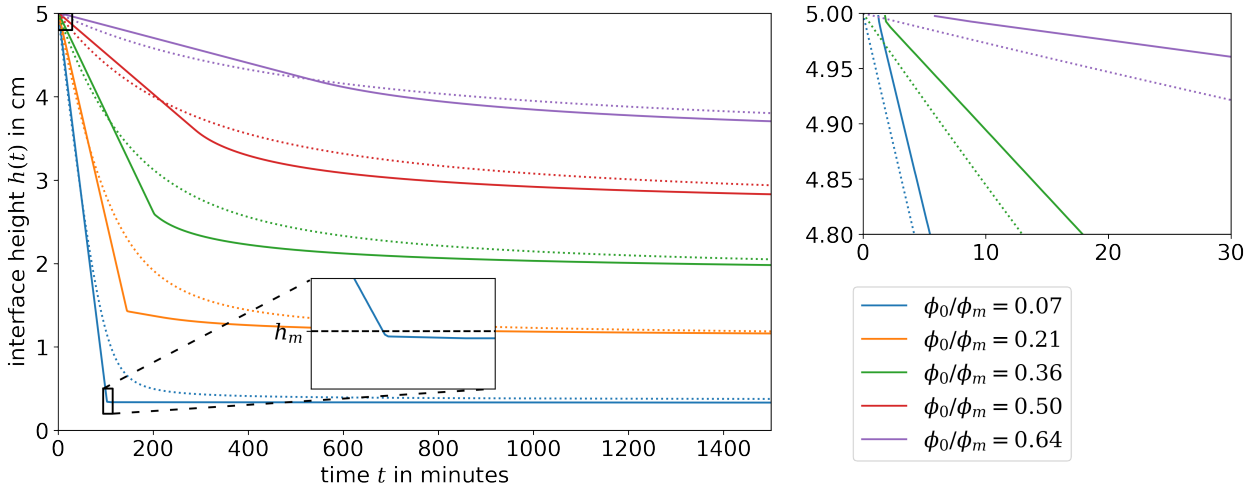

Figure 27: Comparison of the time evolution of the interface height for the space-dependent (full lines) and -independent (dotted lines) model. We have matched parameters such that equal colors, corresponding to given initial volume fractions as indicated by the legend, describe the same system. The interface height decreases linearly until it corresponds to the height of the dense debris at the bottom of the sample. Especially for small ϕ_0, this transition is sudden, but the inset shows that it is smooth. For small enough ϕ_0, the interface height may drop below the theoretical minimum h_m. On the right, we show a selection of these volume fractions in the region indicated by the black box on the top left. We see a small delay time before the top of the gel detaches from the top of the sample for the space-dependent model.

5.4.5 Delay times

In order to explain the nature of this delay time, we observe how it depends on the parameters of our system. We define the delay time t_d as the amount of time required for the volume fraction of the top cell to fall below $0.2\phi_0$. We have observed the delay time to depend on the initial volume fraction, and we expect that the grid size should also play a role. The right panel of figure 28 clearly shows that the delay time is simply a result of the discretization of the problem.

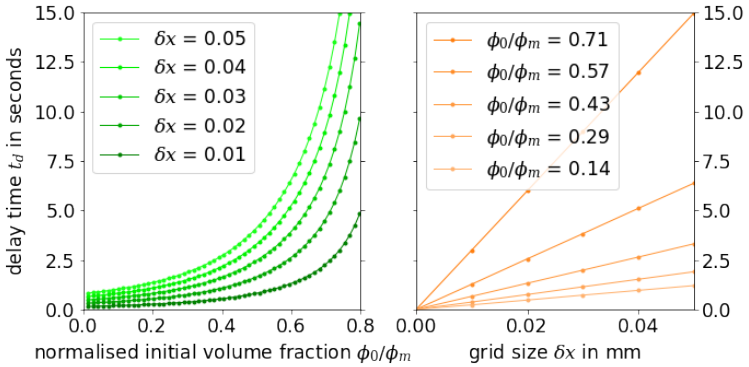

Figure 28: The delay time t_d as a function of initial volume fraction ϕ_0 and grid size δx. The dots correspond to data points, the lines serve to guide the eye.

6 Discussion

We have reproduced the space-homogeneous model from the existing literature. We found that it captures one of the three collapse behaviours (slow sedimentation) that are found in experiments. We also see that different definitions of the permeability led to the same qualitative behaviour, but some choices limit the range of applicability of the model. At the coarse-grained level of this model, we are not concerned about this.

We improved upon this coarse-grainedness by treating the colloidal volume fraction as a height-dependent field. This model captures captures another collapse behaviour, the fast collapse that is followed by a slow compactification. This is characterized by low initial volume fractions, and a sharp transition from a linear decay of interface height to exponential. This corresponds to the experimental results from [17, 27], amongst others.

This model also lead to numerical challenges that are typically found in problems with large gradients (i.e. the gel interface). This leads to peaks in the volume fraction profile that are higher than its maximum, which we expect to be due to the discontinuity of the colloidal velocity. This problem is encountered more often in problems where fluid and structure are coupled, and another numerical scheme could provide a solution [73–75, 190].

However, it is important to note the following. In our study of numerical schemes, we found that the FOU scheme causes (severe) artificial diffusion in time-dependent problems such as this one. In that case, we should not expect these peaks, but they do still arise. Also, refining the grid does not smooth out these peaks. This suggests that the origin of these peaks lie in the theoretical framework rather than the numerical scheme.

Another important result of this work is the exclusion of the osmotic pressure as a possible candidate to cause the delay time. It was also proposed that this pressure drives the rapid collapse after the delay [21]. However, it is a few orders of magnitude too small to play a significant role.

Similar to the osmotic pressure, other forces are easily implemented, once the effective contribution is determined. A successful example of this shows that a visco-elastic force causes delay times (much) larger than the grid artifacts [87].

7 Summary and outlook

In this thesis project, we have studied a space-homogeneous model that is able to capture the time evolution of the interface of gels. Since this model is very coarse-grained, it was possible to solve it analytically. The outcome of this model is a stretched exponential decay of interface height as a function of time. This was confirmed by others to agree with experimental data for the range of initial conditions that corresponds to strong gels.

The space-dependent model we studied is more complex and we found no analytical solution. Solving this convection-dominated model came with more computational challenges. Most of these challenges have been dealt with, and only minor numerical artifacts remained. This led to results that are in agreement with experimental data for a wider range of initial conditions.

These numerical artifacts are the volume fraction peaks near the interface. A different numerical scheme, the WENO-JS scheme, performs well for convection-dominated problems, and specifically near interfaces [190]. This adjustment of the model could improve the correspondence to experimentally observed volume fraction profiles.

Another feature of this model was illustrated by the discussion of the influence of the osmotic pressure. Once the *effective* contribution of a given microscopic force has been determined, it is immediately obvious whether it plays a significant role or not.

One obvious way to further improve upon this model is to incorporate the horizontal spatial dependence of the volume fraction. This would allow us to account for (vertical) pores and dense debris falling through the network. Also, we can include shear forces, which are quite likely to be larger than those associated with uniform compression. This is because compression is distributed through the (bulk) network, but shear forces could affect a single strand. Another advantage of this model is the ability to initialize the system with a much wider range of initial configurations.

A The Cauchy momentum equation of fluid motion

In this appendix, we derive the simplified momentum balance equations that follow from the full Navier-Stokes equation, the convective form of the Cauchy momentum equation for incompressible fluids. The momentum equation reads [191]

$$\frac{D\boldsymbol{u}}{Dt} = \frac{1}{\rho}\boldsymbol{\nabla}\cdot\boldsymbol{\sigma} + \boldsymbol{f}, \tag{A.1}$$

where ρ is the density of the fluid, σ the stress tensor and $\boldsymbol{f}$ an external stress, in our case this will be the gravitational stress $\boldsymbol{g}$. On the left-hand side, we have defined a material derivative

$$\frac{D\boldsymbol{u}}{Dt} \equiv \partial_t\boldsymbol{u} + \boldsymbol{u}\cdot\boldsymbol{\nabla}\boldsymbol{u} \simeq \partial_t\boldsymbol{u} + \partial_t\boldsymbol{x}\cdot\boldsymbol{\nabla}\boldsymbol{u} = \frac{d\boldsymbol{u}(\boldsymbol{x},t)}{dt}. \tag{A.2}$$

We see that the material derivative is related to the total time derivative of $\boldsymbol{u}$, and is equal when the path $\boldsymbol{x}(t)$ is chosen such that $\dot{\boldsymbol{x}} = \boldsymbol{u}$. Being a bit more precise here will turn out to be useful, and we make this statement more rigorous in the following way. We start with the Reynolds transport theorem for a (compressible) fluid element [192],

$$\frac{d}{dt}\int_{\Omega(t)} \boldsymbol{f}\, dV = \int_{\Omega(t)} \frac{\partial \boldsymbol{f}}{\partial t}\, dV + \int_{\partial\Omega(t)} (\boldsymbol{v}_b\cdot\boldsymbol{n})\, \boldsymbol{f}\, dA, \tag{A.3}$$

where Ω denotes the volume of the fluid element. It is an important observation that this volume is time-dependent, since if it were not, the second term on the right would vanish. This becomes clear from the definition of $\boldsymbol{v}_b$, the velocity of the boundary, with $\boldsymbol{n}$ its outward-pointing normal vector. If Ω is time-independent, then obviously $\boldsymbol{v}_b\cdot\boldsymbol{n} = 0$. We also note that the Reynolds transport theorem holds for any scalar-, vector- or tensor valued function $\boldsymbol{f}$ [193]. Letting $\Omega(t)$ be the volume of a fluid element, the boundaries obey $\boldsymbol{v}_b\cdot\boldsymbol{n} = \boldsymbol{u}\cdot\boldsymbol{n}$, with $\boldsymbol{u}$ the velocity of the fluid element [194]. Using the identity $(\boldsymbol{b}\cdot\boldsymbol{n})\boldsymbol{a} = (\boldsymbol{a}\otimes\boldsymbol{b})\cdot\boldsymbol{n}$, absorbing $\boldsymbol{n}$ into dA and applying the divergence theorem leads to

$$\frac{d}{dt}\int_{\Omega(t)} \boldsymbol{f}\, dV = \int_{\Omega(t)} \frac{\partial \boldsymbol{f}}{\partial t} + \boldsymbol{\nabla}\cdot[\boldsymbol{f}\otimes\boldsymbol{u}]\, dV. \tag{A.4}$$

Finally, we observe that $\boldsymbol{\nabla}\cdot[\boldsymbol{a}\otimes\boldsymbol{b}] = (\boldsymbol{a}\cdot\boldsymbol{\nabla})\,\boldsymbol{b} + (\boldsymbol{\nabla}\cdot\boldsymbol{a})\,\boldsymbol{b}$. This implies that the total time derivative is equal to the material derivative exactly when the fluid element is incompressible. Now we turn our attention to the right-hand side of equation A.1, and assume our fluid to be Newtonian. In this case, the stress tensor σ can be expressed as the sum of a viscosity term $\boldsymbol{\tau}$, the deviatoric stress, and an isotropic pressure term $-p\boldsymbol{I}$, the volumetric stress. For a Newtonian fluid, the viscous stress tensor depends linearly on the the rate-of-strain tensor $\boldsymbol{\varepsilon}(\boldsymbol{\nabla}\boldsymbol{u}) = 1/2\left(\boldsymbol{\nabla}\boldsymbol{u} + (\boldsymbol{\nabla}\boldsymbol{u})^{\mathrm{T}}\right)$ [195]. Note that $\boldsymbol{\nabla}\boldsymbol{u}$ is the deformation rate as introduced in section 3.1. The most general form of the viscous stress tensor $\boldsymbol{\tau}$ for a homogeneous and isotropic Newtonian fluid is [196]

$$\boldsymbol{\tau}_N = \lambda(\boldsymbol{\nabla}\cdot\boldsymbol{u})\boldsymbol{I} + 2\mu\boldsymbol{\varepsilon}, \tag{A.5}$$

where μ is the dynamic viscosity coefficient, related to the shear viscosity of the fluid. λ is the second viscosity coefficient, or volume viscosity, related to the dilatational viscosity ζ [86]. This relation is found in the following way. We use that $\mathrm{tr}(\boldsymbol{\varepsilon}) = \boldsymbol{\nabla} \cdot \boldsymbol{u}$ to separate $\boldsymbol{\tau}_N$ into an isotropic and deviatoric part. The total Newtonian contribution to the stress is now defined as

$$\boldsymbol{\sigma}_N = -p\boldsymbol{I} + (\lambda + 2/3\mu)(\boldsymbol{\nabla} \cdot \boldsymbol{u})\boldsymbol{I} + 2\mu\left(\boldsymbol{\varepsilon} - 1/3(\boldsymbol{\nabla} \cdot \boldsymbol{u})\boldsymbol{I}\right). \tag{A.6}$$

From this equation, we observe that isotropic dilatations of a volume element produce a viscous stress. We conclude that the dilatational viscosity coefficient ζ is in this case equal to $\lambda + 2/3\mu$. For incompressible fluids, the second terms in equation A.6 is zero, since $\boldsymbol{\nabla} \cdot \boldsymbol{u} = 0$. Also for compressible fluids, this term seems to be negligible. Stokes suggested [197] that $\zeta = 0$, now known as Stokes' hypothesis, and has become common practice in the study of compressible fluids [195]. However, in our case, it is worth taking a closer look at the meaning of this term. We see that $\zeta \boldsymbol{\nabla} \cdot \boldsymbol{u}$ can be interpreted as the difference between the hydrostatic pressure p and the normal stresses on a fluid element. This difference is usually referred to as the *mechanical pressure*, and is considered to be due to the time lag of thermodynamic equilibrium in a motion that implies isotropic dilatation of that element [195]. Torre *et al.* [87] show that this pressure, or dilatational viscosity, turns out to play a very important role in explaining the delay time of a gel's collapse. However, this type of viscosity is zero for incompressible fluids, and thus has a different origin. The dilatational viscosity is due to the presence of the colloidal phase in this case. Following the reasoning of Torre *et al.*, we define the total stress tensor as

$$\boldsymbol{\sigma} = -p\boldsymbol{I} + \mu\boldsymbol{\varepsilon} + \boldsymbol{\sigma}_c, \tag{A.7}$$

where $\boldsymbol{\sigma}_c$ is the network contribution to the stress. They define this tensor as

$$\boldsymbol{\sigma}_c = \lambda(\phi)\left(\boldsymbol{\nabla} \cdot \boldsymbol{v}_c\right)\boldsymbol{I}, \tag{A.8}$$

where λ denotes the bulk viscosity, and $\boldsymbol{v}_c$ the velocity of the colloidal phase. This term closely resembles[43] the previous definition of the bulk viscosity and can thus also be considered as a source of mechanical pressure. We note that this definition of $\boldsymbol{\sigma}$ ensures Galilean invariance, since it only depends on spatial derivatives of the flow velocity. We combine the equations A.1, A.2 and A.7 to reproduce the Navier-Stokes equation of an incompressible fluid [198, 86], with a network stress contribution $\boldsymbol{\sigma}_c$ in a gravitational field $\boldsymbol{g}$. Note that this equation holds for a single, incompressible phase.

$$\partial_t \boldsymbol{u} + \boldsymbol{u} \cdot \boldsymbol{\nabla}\boldsymbol{u} = \frac{1}{\rho}\boldsymbol{\nabla} \cdot (-p\boldsymbol{I} + \boldsymbol{\sigma}_c + 2\mu\boldsymbol{\varepsilon}) + \boldsymbol{g} \tag{A.9}$$

A.1 The general form of the momentum equation

In section 5, we expressed equation A.9 in terms of the mixture and the separate components. Then we ignored the inertial terms (the left-hand sides) to arrive at the relations in

[43] Observe that this term depends on the velocity of the colloidal phase rather than the velocity of the fluid phase.

equation 59. Here, we provide the details on the same computation if we cannot a priori assume that we are in the quasi-hydrostatic regime. We repeat equations 55, 57 and 58 here,

$$\frac{d}{dt}\int_V dV \rho_m(\phi)\boldsymbol{u} = \int_V dV\left(\rho_m(\phi)\boldsymbol{g} + \boldsymbol{\nabla}\cdot\boldsymbol{\sigma}\right), \tag{55, repeated}$$

$$\frac{d}{dt}\int_V dV \rho_c\phi\boldsymbol{v}_c = \int_V dV\left(\rho_c\phi\boldsymbol{g} + \boldsymbol{\Sigma}_{cc} + \boldsymbol{\Sigma}_{cl}\right), \tag{57, repeated}$$

$$\frac{d}{dt}\int_V dV \rho_l(1-\phi)\boldsymbol{v}_l = \int_V dV\left(\rho_l(1-\phi)\boldsymbol{g} + \boldsymbol{\Sigma}_{ll} + \boldsymbol{\Sigma}_{lc}\right). \tag{58, repeated}$$

We recall the definitions of the volume-fraction-weighted density $\rho_m = \phi\rho_c + (1-\phi)\rho_l$ and density-weighted mixture velocity $\boldsymbol{u} = \left(\phi\rho_c\boldsymbol{v}_c + (1-\phi)\rho_l\boldsymbol{v}_l\right)/\rho_m(\phi)$. First, we focus on the left-hand sides of the above equations. From the preceding section, we know that we must be careful with time derivates of integrals. As in section 5, we consider the following

$$\frac{d}{dt}\int_V dV \rho_c\phi\boldsymbol{v}_c + \frac{d}{dt}\int_V dV \rho_l(1-\phi)\boldsymbol{v}_l - \frac{d}{dt}\int_V dV \rho_m(\phi)\boldsymbol{u}. \tag{A.10}$$

We apply the Reynolds transport theorem in the form of equation A.4,

$$\int_V dV \frac{\partial\left(\rho_c\phi\boldsymbol{v}_c\right)}{\partial t} + \frac{\partial\left(\rho_l(1-\phi)\boldsymbol{v}_l\right)}{\partial t} - \frac{\partial\left(\rho_m\boldsymbol{u}\right)}{\partial t} + \boldsymbol{\nabla}\cdot\left[\rho_c\phi\boldsymbol{v}_c\otimes\boldsymbol{v}_c + \rho_l(1-\phi)\boldsymbol{v}_l\otimes\boldsymbol{v}_l - \rho_m\boldsymbol{u}\otimes\boldsymbol{u}\right], \tag{A.11}$$

where all terms belong to the same integral. The time derivatives cancel, and there is a correspondence between the terms in the square brackets. We multiply the first two of these terms by $1 = (\phi\rho_c + (1-\phi)\rho_l)/\rho_m$ and expand $\boldsymbol{u}$,

$$\begin{aligned}\boldsymbol{\nabla}\cdot\left[\rho_c\left(\phi\rho_c + (1-\phi)\rho_l\right)/\rho_m\phi\boldsymbol{v}_c\otimes\boldsymbol{v}_c\right] + \boldsymbol{\nabla}\cdot\left[\rho_l\left(\phi\rho_c + (1-\phi)\rho_l\right)/\rho_m(1-\phi)\boldsymbol{v}_l\otimes\boldsymbol{v}_l\right] - \\ \boldsymbol{\nabla}\cdot\left[\left(\rho_c\phi\boldsymbol{v}_c + \rho_l(1-\phi)\boldsymbol{v}_l\right)\otimes\left(\rho_c\phi\boldsymbol{v}_c + \rho_l(1-\phi)\boldsymbol{v}_l\right)/\rho_m\right].\end{aligned} \tag{A.12}$$

We observe that the outer product is linear, which allows us to separate the above in the following way,

$$\begin{aligned}\boldsymbol{\nabla}\cdot\left[\left(\phi^2\rho_c^2 + \phi(1-\phi)\rho_c\rho_l\right)/\rho_m\boldsymbol{v}_c\otimes\boldsymbol{v}_c\right] + \boldsymbol{\nabla}\cdot\left[\left(\phi(1-\phi)\rho_c\rho_l + (1-\phi)^2\rho_l^2\right)/\rho_m\boldsymbol{v}_l\otimes\boldsymbol{v}_l\right] - \\ \boldsymbol{\nabla}\cdot\left[\rho_c^2\phi^2/\rho_m\boldsymbol{v}_c\otimes\boldsymbol{v}_c\right] - \boldsymbol{\nabla}\cdot\left[\rho_c\rho_l\phi(1-\phi)/\rho_m\boldsymbol{v}_c\otimes\boldsymbol{v}_l\right] - \\ \boldsymbol{\nabla}\cdot\left[\rho_c\rho_l\phi(1-\phi)/\rho_m\boldsymbol{v}_l\otimes\boldsymbol{v}_c\right] - \boldsymbol{\nabla}\cdot\left[\rho_l^2(1-\phi)^2/\rho_m\boldsymbol{v}_l\otimes\boldsymbol{v}_l\right].\end{aligned} \tag{A.13}$$

This leads us to the following rather symmetrical expression

$$\begin{aligned}\boldsymbol{\nabla}\cdot\left[\rho_c\rho_l\phi(1-\phi)/\rho_m\boldsymbol{v}_c\otimes\boldsymbol{v}_c\right] - \boldsymbol{\nabla}\cdot\left[\rho_c\rho_l\phi(1-\phi)/\rho_m\boldsymbol{v}_c\otimes\boldsymbol{v}_l\right] - \\ \boldsymbol{\nabla}\cdot\left[\rho_c\rho_l\phi(1-\phi)/\rho_m\boldsymbol{v}_l\otimes\boldsymbol{v}_c\right] + \boldsymbol{\nabla}\cdot\left[\rho_c\rho_l\phi(1-\phi)/\rho_m\boldsymbol{v}_l\otimes\boldsymbol{v}_l\right].\end{aligned} \tag{A.14}$$

We exploit this symmetry by introducing the velocity difference $\boldsymbol{\delta v} = \boldsymbol{v}_c - \boldsymbol{v}_l$. We conclude that equation A.10 can be expressed as

$$\boldsymbol{\nabla}\cdot\left[\rho_c\rho_l\,\phi(1-\phi)/\rho_m\boldsymbol{\delta v}\otimes\boldsymbol{\delta v}\right] \tag{A.15}$$

On the right-hand side of the equations, nothing has changed and we refer to section 5 for a more detailed derivation. Here, we state that

$$\boldsymbol{\nabla} \cdot [-p\boldsymbol{I} + 2\mu\boldsymbol{\varepsilon} + \boldsymbol{\sigma}_c + \rho_c\rho_l\phi(1-\phi)/\rho_m \boldsymbol{\delta v} \otimes \boldsymbol{\delta v}] = \boldsymbol{\Sigma}_{ll} + \boldsymbol{\Sigma}_{cc}\,, \tag{A.16}$$

where the last term in brackets is the additional term that appears when we cannot assume that our problem lies within the quasi-hydrostatic regime. This non-Newtonian stress response is due to the presence of the colloidal phase and is thus captured in $\boldsymbol{\Sigma}_c c$. Also, for notational convenience, we will use $\tilde{\boldsymbol{\sigma}}_c = \boldsymbol{\sigma}_c + \rho_c\rho_l\phi(1-\phi)/\rho_m \boldsymbol{\delta v} \otimes \boldsymbol{\delta v}$.

Now we wish to follow a similar procedure as in section 5 to eliminate the pressure dependence, but we must take the time derivatives into account. We observe that

$$\frac{d}{dt}\int_V dV \rho_c\phi\boldsymbol{v}_c = \int_V dV \rho_c \frac{\partial \phi \boldsymbol{v}_c}{\partial t} + \rho_c\left(\boldsymbol{\nabla}\cdot\phi\boldsymbol{v}_c\right)\boldsymbol{v}_c + \rho_c\phi\left(\boldsymbol{v}_c\cdot\boldsymbol{\nabla}\right)\boldsymbol{v}_c, \tag{A.17}$$

and recall that $\int_V dV \partial_t\phi = -\int_V dV \boldsymbol{\nabla}\cdot\rho_c\phi\boldsymbol{v}_c$ by mass conservation. Using the chain rule for the partial time derivative, we find

$$\frac{d}{dt}\int_V dV \rho_c\phi\boldsymbol{v}_c = \int_V dV \rho_c\phi \frac{\partial \boldsymbol{v}_c}{\partial t} + \rho_c\phi\left(\boldsymbol{v}_c\cdot\boldsymbol{\nabla}\right)\boldsymbol{v}_c. \tag{A.18}$$

This has a clear correspondence to the material derivative, which we explicitly state to be $D_t^i = \partial_t + \boldsymbol{v}_i\cdot\boldsymbol{\nabla}$, with $i = c, l$. This gives us the following alternative expressions for the left-hand sides of equations 57 and 58,

$$\frac{d}{dt}\int_V dV \rho_c\phi\boldsymbol{v}_c = \int_V dV \phi D_t^c\left[\rho_c\boldsymbol{v}_c\right] \tag{A.19}$$

$$\frac{d}{dt}\int_V dV \rho_l(1-\phi)\boldsymbol{v}_i = \int_V dV (1-\phi) D_t^l\left[\rho_l\boldsymbol{v}_l\right] \tag{A.20}$$

Now we can eliminate the pressure dependence in the following way. We substitute these into equations 57 and 58, and divide the former by ϕ and the latter by $(1-\phi)$, both inside the integral. Now we subtract the second relation from the first to arrive at the following

$$D_t^c\left[\rho_c\boldsymbol{v}_c\right] - D_t^l\left[\rho_l\boldsymbol{v}_l\right] + \frac{\mu\boldsymbol{\delta v}}{\phi k(\phi)} = \rho_b\boldsymbol{g} + \frac{\boldsymbol{\nabla}\cdot\tilde{\boldsymbol{\sigma}}_c}{\phi} - \frac{2\mu\boldsymbol{\nabla}\cdot\boldsymbol{\varepsilon}}{1-\phi} \tag{A.21}$$

A.2 The quasi-hydrostatic regime

We set out to simplify this equation by expressing the terms in equation A.21 as nondimensional variables. In order to do so, we study the procedure that is used to nondimensionalize equation A.9. This leads us to a set of parameters that is typically used to characterize the flow regime and then apply these ideas to equation A.21. We introduce the nondimensional variables as given in table 5.

$\boldsymbol{u}^* \equiv \boldsymbol{u}/u_0$	$t^* \equiv tu_0/r_0$	$\boldsymbol{\nabla}^* \equiv r_0\boldsymbol{\nabla}$	$\rho^* \equiv \rho/\rho_0$	$\boldsymbol{g}^* = \boldsymbol{f}/g$
$\mu^* \equiv \mu/\mu_0$	$\lambda^* \equiv \lambda/\mu_0$	$\boldsymbol{\varepsilon}^* \equiv \boldsymbol{\varepsilon} r_0/u_0$	$\boldsymbol{\sigma}^* \equiv \boldsymbol{\sigma} r_0/(\mu_0 u_0)$	$p^* \equiv p/(\rho_0 g r_0)$

Table 5: Overview of parameters that are involved in the nondimensionalization of equation A.9. Note that the characteristic force is the gravitational force, and the dimensions of the pressure are based on the hydrostatic pressure equation. The viscosity coefficients λ and μ have the same dimensions and thus scale with the same scaling coefficient μ_0.

Inserting the above relations into equation A.9 in order to express it in terms of nondimensional variables, we find

$$\begin{aligned}
\frac{u_0^2}{r_0}\frac{\partial \boldsymbol{u}^*}{\partial t^*} + \frac{u_0^2}{r_0}\boldsymbol{u}^*\cdot\boldsymbol{\nabla}^*\boldsymbol{u}^* &= \frac{1}{\rho_0\rho^* r_0}\boldsymbol{\nabla}^*\left(-\rho_0 g r_0 p^*\boldsymbol{I} + \frac{u_0\mu_0}{r_0}\boldsymbol{\sigma}_c^* + \frac{u_0\mu_0}{r_0}2\mu^*\boldsymbol{\varepsilon}^*\right) + g\boldsymbol{g}^*; \\
\frac{u_0^2}{r_0 g}\left(\frac{\partial \boldsymbol{u}^*}{\partial t^*} + \boldsymbol{u}^*\cdot\boldsymbol{\nabla}^*\boldsymbol{u}^*\right) &= \frac{1}{\rho^*}\boldsymbol{\nabla}^*\left(-p^*\boldsymbol{I} + \frac{u_0\mu_0}{\rho_0 r_0^2 g}\left(\boldsymbol{\sigma}_c^* + 2\mu^*\boldsymbol{\varepsilon}^*\right)\right) + \boldsymbol{g}^*. \qquad \text{(A.22)}
\end{aligned}$$

We identify the first coefficient as the square of the Froude number Fr [199], a dimensionless quantity that is defined as the ratio of the flow inertia to the external field. It is defined as

$$\mathrm{Fr} = \frac{u}{\sqrt{gL}} = \frac{u_0}{\sqrt{gr_0}}, \qquad \text{(A.23)}$$

where the second equality relates the number to its current use. In the quasi-hydrostatic limit, we have that $\mathrm{Fr} \to 0$, such that we may neglect the left-hand side of equation A.22. We verify that our system lies in by the quasi-hydrostatic regime in the following way. The typical velocity in our system is that of a single sedimenting sphere in a viscous fluid. From Stokes' law, we observe that $u_0 \sim \rho_0 g\sigma^2/\mu_0$. Note that σ denotes the diameter of a colloidal particle, such that $\sigma \sim 10^{-6}$ m, and $\rho_0 \sim 10^3$ kg/m, $g \sim 10$ m/s^2, and $\mu_0 \sim 10^{-3}$ Pas. This leads to $\mathrm{Fr} \sim 10^{-4}$, and the prefactor on the left-hand side of equation A.22 is the square of the Froude number. This implies that we can safely assume the inertial contribution to be negligible, and thus we can use the quasi-hydrostatic limit. Now we turn our attention to the prefactor of the stress terms in equation A.22. We define the ratio of the colloid diameter and r_0 as $\alpha = \sigma/r_0$. In that case, we have

$$\frac{u_0\mu_0}{\rho_0 r_0^2 g} = \frac{\sigma^2}{r_0^2} = \alpha^2, \qquad \text{(A.24)}$$

and we observe that $\alpha \to 0$ corresponds to the hydrostatic limit where $\boldsymbol{\nabla}p = -\rho\boldsymbol{g}$.

Now we use these ideas to study equation A.21. We divide this equation by ρ_b and let $\rho = \rho_b$, and observe that all velocities are of the same order of magnitude, thus all scaling with u_0. We note that $k(\phi) \sim \sigma^2$, such that $k^*(\phi) = k(\phi)/\sigma^2$. Now we apply the substitutions of table 5 to find

$$\begin{aligned}
\frac{u_0^2}{r_0 g}\left(D_t^{c*}\left[\rho_c/\rho_b\boldsymbol{v}_c^*\right] - D_t^{l*}\left[\rho_l/\rho_b\boldsymbol{v}_l^*\right]\right) + \frac{\mu_0 u_0}{\rho_0 g\sigma^2}\frac{\mu^*\boldsymbol{\delta v}^*}{\rho^*\phi k^*(\phi)} = \\
\boldsymbol{g}^* + \frac{u_0\mu_0}{\rho_0 r_0^2 g}\left(\frac{\boldsymbol{\nabla}^*\cdot\boldsymbol{\sigma}_c^*}{\phi} - \frac{2\mu^*\boldsymbol{\nabla}^*\cdot\boldsymbol{\varepsilon}^*}{1-\phi}\right) + \frac{u_0^2}{r_0 g}\boldsymbol{\nabla}\cdot\left[\rho_c\rho_l\phi(1-\phi)/(\rho_m\rho_b)\boldsymbol{\delta v}\otimes\boldsymbol{\delta v}\right]. \qquad \text{(A.25)}
\end{aligned}$$

We observe that we can also write this equation in terms of the parameters α and β, and thus in the quasi-hydrostatic limit,

$$\lim_{\beta\to 0} \frac{\mu^* \boldsymbol{\delta v}^*}{\rho^* \phi k^*(\phi)} = \boldsymbol{g}^* + \alpha^2 \left(\frac{\boldsymbol{\nabla}^* \cdot \boldsymbol{\sigma}_c^*}{\phi} - \frac{2\mu^* \boldsymbol{\nabla}^* \cdot \boldsymbol{\varepsilon}^*}{1-\phi} \right). \tag{A.26}$$

In the limit of $\alpha \to 0$, we find a slightly modified version of the velocity of a sedimenting sphere. However, we wish to capture the influence of processes on the microscale, thus α is very small but finite. In this case, we find that the contribution from the deviatoric stress of the liquid is very small, and thus we neglect it. The contribution of the colloids $\boldsymbol{\sigma}_c$ may have a singularity, especially for volume fractions near ϕ_m, thus it will probably play an important role. We also note that the value of α depends on the grid size, so the right-most term may not drop out for very fine grids.

In our case, we isolate the velocity difference and re-dimensionalise the equation. From the definition of u_0, we observe that $\rho^* \boldsymbol{g}^* / \mu^* = -\hat{\boldsymbol{z}}$. For notational convenience, we leave k and ρ dimensionless, and note that $\rho^* = 1$ by assumption. Thus, in the quasi-hydrostatic limit,

$$\boldsymbol{\delta v} \approx k^*(\phi) \left(-u_0 \phi \hat{\boldsymbol{z}} + \sigma^2 / \mu \, \boldsymbol{\nabla} \cdot \boldsymbol{\sigma}_c \right) \tag{A.27}$$

B The accuracy of discretization schemes

In section 5.3, we mentioned that the choice of defining the flux at cell boundaries can affect the accuracy of the integration scheme. The accuracy is typically defined as the the Taylor series truncation error, which arises more naturally when we study finite difference methods (FDMs). We will use the FDM to introduce the concept, and this discussion also illustrates that the FVM and FDM are computationally the same, despite their different reasoning. It is important to note that this is only true for specific cases such as a uniform[44] one-dimensional grid. The FDM is the oldest method of obtaining numerical solutions to differential equations, of which the first application is attibuted to Leonhard Euler in 1768 [187]. This method is based on defining derivatives in terms of differences of the state variable over a finite distance, corresponding to the distances between grid points. That is, we use the following discretization:

$$\left(\frac{d\phi}{dx} \right)_i = \lim_{\delta x \to 0} \frac{\phi(x+\delta x) - \phi(x)}{\delta x} \Rightarrow \frac{\phi(x_{i+1}) - \phi(x_i)}{x_{i+1} - x_i}, \tag{B.1}$$

where ϕ is our state variable, and x_i the discretized version of the space variable. The method above is referred to as *first-order forward difference*, where forward refers to the choice of comparing $\phi(x_i)$ with its neighboring value in the positive direction, and first-order to its Taylor series truncation error. For the sake of completeness, we write the Taylor expansion of ϕ around x_i:

$$\phi(x_{i\pm 1}) \approx \phi(x_i) \pm \delta x \left(\frac{d\phi}{dx} \right)_i + \frac{\delta x^2}{2} \left(\frac{d^2\phi}{dx^2} \right)_i \pm \frac{\delta x^3}{6} \left(\frac{d^3\phi}{dx^3} \right)_i + \mathcal{O}(\delta x^4)$$

[44] A uniform grid is evenly spaced, with cell boundaries exactly in the middle of grid points

We illustrate the accuracy with the obvious alternative *first-order backward difference*, which is based on considering a difference of $-\delta x$ instead of δx, leading to

$$\frac{\phi(x_{i-1}) - \phi(x_i)}{x_{i-1} - x_i} \approx \left(\frac{d\phi}{dx}\right)_i = \frac{\phi(x_i) - \phi(x_{i-1})}{\delta x} + \frac{\delta x}{2}\left(\frac{d^2x}{\delta x^2}\right)_i + \mathcal{O}(\delta x^2)$$

This shows that this approximation is first-order accurate in terms of the truncation error of the Taylor series, given on the right. The first-order error can be eliminated by averaging the backward and forward difference, creating a second-order approximation that is referred to as the central difference (CD) scheme for obvious reasons.

Accuracy of FVM schemes

Having introduced the necessary tools to study the accuracy of an integration scheme, we turn our attention to FVMs, where we are interested in the cell boundaries. Applying the CD scheme to the upper boundary of cell i (denoted by $i+$ again), using a distance of $\delta x/2$, has the following result:

$$\begin{aligned}\left(\frac{d\phi}{dx}\right)_{i+} &= \frac{1}{2}\left(\frac{\phi(x_{i+1}) - \phi(x_{i+})}{\delta x/2} + \frac{\delta x}{8}\left(\frac{d^2x}{\delta x^2}\right)_i + \frac{\phi(x_{i+}) - \phi(x_i)}{\delta x/2} - \frac{\delta x}{8}\left(\frac{d^2x}{\delta x^2}\right)_i\right) + \mathcal{O}(\delta x^2) \\ &\approx \frac{\phi(x_{i+1}) - \phi(x_i)}{\delta x},\end{aligned} \tag{B.2}$$

which is thus second-order accurate in δx. This relation is used to approximate diffusive terms that depend on the spatial derivative of ϕ. Confusingly, the RHS of this equation is exactly the same as that of equation B.1, which is first-order accurate. The difference lies in the LHS, we define the derivative at the cell boundary instead of the center.

Despite the apparent analogy to FDMs, the reasoning behind FVMs is very different, which is based on fluxes rather than derivatives. In section 5.3.1, we introduced the mathematical representation of this method, leading to equation 74, which shows that we express the flux at the boundary of a cell in terms of the state variable ϕ. The central difference is rather trivial in this case,

$$\phi(x_{i+}) = \left(\phi(x_i) + \phi(x_{i+1})\right)/2 + \mathcal{O}(\delta x^2),$$

which is again second-order accurate since the first-order terms cancel. The upwind-biased scheme for pure convection, introduced in section 5.3.2, depends on only one term, but is first-order accurate. We repeat the scheme,

$$\phi(x_{i+}) \approx \phi(x_{i+1})$$

assuming convective flow from right to left. Note that *upwind* is defined in terms of flow direction, whereas direction in FDMs is defined in terms of spatial orientation, independent of the flow direction. Comparing the scheme to the Taylor series of $\phi(x_{i+})$, we can trivially conclude that this approximation is first-order accurate. To increase the accuracy, we can use the CD scheme, but we lose transportiveness (discussed in section 5.3) of the scheme. Using that the grid is uniform, we explore different combinations of terms with higher-order

accuracy, such as the linear upwind difference (LUD) scheme, in which the first-order error can be shown to cancel in the following way:

$$\phi(x_{i+1}) = \phi(x_{i+}) + \frac{\delta x}{2}\left(\frac{d\phi}{dx}\right)_{i+} + \mathcal{O}(\delta x^2)$$
$$\phi(x_{i+2}) = \phi(x_{i+}) + 3\,\frac{\delta x}{2}\left(\frac{d\phi}{dx}\right)_{i+} + \mathcal{O}(\delta x^2)$$

Combining these leads to the LUD scheme which is thus second-order accurate,

$$\phi(x_{i+}) = \left(3\,\phi(x_{i+1}) - \phi(x_{i+2})\right)/2 + \mathcal{O}(\delta x^2)$$

A similar procedure can be applied to further increase the accuracy while keeping the scheme biased in the 'upwind' direction, leading to the third-order accurate scheme that meets the transportiveness requirement. An example of this is the quadratic upstream interpolation for convective kinetics (QUICK) scheme,

$$\phi(x_{i+}) = \left(6\,\phi(x_i) + 3\,\phi(x_{i+1}) - \phi(x_{i+2})\right)/8 + \mathcal{O}(\delta x^3)$$

These results can be generalized to apply to non-uniform grids, but we shall not do so here, since the grid used in our study is uniform. We also note that increasing accuracy comes at the cost of computational effort, and we will also show that higher-order schemes are do not meet the boundedness requirement unconditionally. Also, since higher-order schemes depend on more neighboring nodes, implementing boundary conditions becomes more involved.

Another important remark is that the polynomial order of accuracy that naturally follows from the Taylor expansion is a good measure in most situations. However, in convection-dominated problems, ϕ typically depends exponentially on x, such that a polynomial representation is only valid for extremely small values of δx [179]. This is illustrated by the better performance of the UD scheme in comparison to the CD scheme at higher Péclet numbers, despite its lower degree of accuracy. More details can be found in appendix C.2.

C The steady convection-diffusion problem

In section 5.3, we claimed that the boundedness property provides clear boundaries on the applicability of an integration scheme, in terms of parameters that define the system. The parameters that we will use to define the system are F and D, describing convection and diffusion, respectively. The definition of these parameters follows from the the differential equation that governs one-dimensional convection-diffusion problems,

$$\frac{d}{dx}(\rho u \phi) = \frac{d}{dx}\left(\Gamma \frac{d\phi}{dx}\right) \tag{C.1}$$

where ρ denotes the density of the transported fluid, u its velocity, ϕ denotes a property of the fluid per unit mass and Γ denotes the diffusion coefficient. We assume our fluid to be

incompressible, such that ρ is constant and the property ϕ that we consider is the volume fraction of colloids. Continuity and incompressibility imply

$$\frac{d}{dx}(\rho u) = \frac{d}{dx}(u) = 0$$

Since our discussion is largely based on chapter 5.2 from [173], we will also adopt the notation used there. Figure 29 illustrates a cell, or control volume, around node P and adjoining nodes W and E. Following the finite volume method, we need an integral over a local balance equation in terms of divergences, reducing it to a surface integral, so equation C.1 becomes

$$(\rho u \phi A)_e - (\rho u \phi A)_w = \left(\Gamma A \frac{d\phi}{dx}\right)_e - \left(\Gamma A \frac{d\phi}{dx}\right)_w$$

In our one-dimensional case, A is constant, so we may drop that term. The continuity equation leads to $u_e - u_w = 0$, such that in one dimension, the flow velocity must be constant throughout the sample.

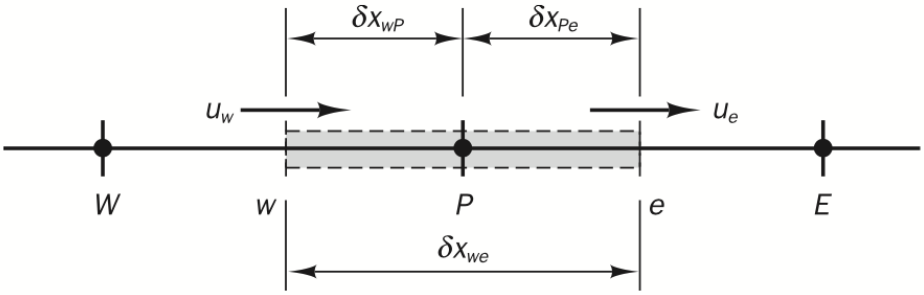

Figure 29: Control volume around node P, with east and west boundaries e and w, respectively. Image taken from [173], with permission.

Using the above definitions and denote the cell width[45] by δx, the parameters defining the system are

$$F = \rho u \quad \text{and} \quad D = \Gamma/\delta x$$

Note that $\delta\phi$ does depend on the cell boundary at which it is computed, for example, $(\delta\phi)_e = \phi_E - \phi_P$. Using this notation, equation C.1 can now be written as

$$F_e\phi_e - F_w\phi_w = D_e(\phi_E - \phi_P) - D_w(\phi_P - \phi_W) \tag{C.2}$$

and the continuity equation implies $F_e = F_w$. Once again, we must make a choice in defining the flux at the boundaries of the cells, in this case by choosing the volume fraction ϕ at that boundary. We will illustrate how this choice affects the boundedness of an integration scheme.

[45]Note that we simplify our discussion by the assumption of a regular grid, such that this is a single parameter.

C.1 Boundedness of the central difference scheme

The CD scheme has been introduced in appendix B, adopting notation leads to $\phi_e = (\phi_P + \phi_E)/2$ and $\phi_w = (\phi_W + \phi_P)/2$. Substituting this into equation C.2,

$$F_e(\phi_P + \phi_E)/2 - F_w(\phi_W + \phi_P)/2 = D_e(\phi_E - \phi_P) - D_w(\phi_P - \phi_W)$$

Collecting terms of ϕ,

$$\begin{aligned}(F_e/2 - F_w/2)\phi_P + (D_e + D_w)\phi_P = \\ ((D_w + F_w/2) + (D_e - F_e/2) + (F_e - F_w))\,\phi_P = (D_w + F_w/2)\phi_W + (D_e - F_e/2)\phi_E \quad \text{(C.3)}\end{aligned}$$

We introduce $a_W = (D_w + F_w/2)$ and $a_E = (D_e - F_e/2)$. Note that continuity implies $F_e = F_w$ here, such that

$$(a_W + a_E)\phi_P = a_W\phi_W + a_E\phi_E$$

Some care must be taken at the boundaries of the grid, but these choices are of limited relevance for the performance of the scheme. Especially in our case, where boundary conditions are relatively simple, since we impose that the walls are not permeable. This also implies that we can express our problem in terms of these coefficients only, without source terms (corresponding to the creation or destruction of colloids). The Scarborough condition [200] is sufficient for convergence of an iterative method, corresponds to *diagonal dominance* of the matrix of coefficients, and is expressed in terms of terms of these coefficients a,

$$\frac{\sum |a_{\text{nb}}|}{|a'_P|} \quad \begin{cases} \leq 1 & \text{at all nodes} \\ < 1 & \text{at one node at least} \end{cases}$$

where a_{nb} are the coefficients of the neighboring nodes, in this case a_W and a_E, and a'_P is the net coefficient of node P, taking into account the source term, which is zero in our case, such that $a'_P = a_P = a_W + a_E$. We note that $\sum |a_{\text{nb}}| = |a_E| + |a_W| = |a_E + a_W| = |a_P|$ if all coefficients have the same sign, showing that the boundedness and diagonal dominance are related but do not coincide. In the absence of sources, the CD scheme does not meet the Scarborough criterion and thus is not diagonally dominant, but is bounded under the condition that all coefficients are positive, since $a_P = D_w + D_e \geq 0$. We have that $a_E > 0$ if $F_e/2 < D_e$ and $a_W > 0$ if $-F_w/2 < D_w$. We assume that Γ is constant, such that $D_e = D_w = D$ on a uniform grid, and since $F_e = F_w = F$, we summarize these conditions as

$$F/D < \text{Pe}_c = 2$$

Where Pe_c is the critical value of the Péclet number[46], above which not all coefficients are positive, such that the CD scheme does not meet the boundedness requirement.

[46]For a discussion of the Péclet number, see section 5.

C.2 Boundedness of the upwind-biased scheme

The UD scheme was introduced in appendix B as well, expressed in our current notation, $\phi_e = \phi_E$ and $\phi_w = \phi_P$, assuming flow from east to west (which is the negative direction). We substitute these relations in equation C.2 to find

$$F_e\phi_E - F_w\phi_P = D_e(\phi_E - \phi_P) - D_w(\phi_P - \phi_W)$$

Collecting terms of ϕ,

$$\begin{aligned}(D_e + D_w - F_e + (F_e - F_w))\,\phi_P &= (D_e - F_e)\phi_E + D_w\phi_W \\ (a_E + a_W + (F_e - F_w))\,\phi_P &= a_E\phi_E + a_W\phi_W\end{aligned} \tag{C.4}$$

The UD scheme is also not diagonally dominant in the absence of sources, but since $F_e \geq 0$, we have that all coefficients are positive, independent of the Péclet number that describes the system. This implies that we expect the UD scheme to produce bounded results under all conditions.

False diffusion

We observe that there are similarities between equations C.3 and C.4, and that these can be converted into one another by a transformation of the diffusive terms. If we substitute $D_{e,w} = D'_{e,w} + F_{e,w}/2$ in equation C.4, we find

$$((D'_w + F_w/2) + (D'_e - F_e/2) + (F_e - F_w))\,\phi_P = (D'_w + F_w/2)\phi_W + (D'_e - F_e/2)\phi_E,$$

which correspond to the CD scheme, equation C.3. This substitution can be defined in terms of the diffusion coefficient as $\Gamma = \Gamma' + \rho u\delta x/2$. Since the UD scheme can be interpreted as the CD scheme with an artificial diffusion term, this is sometimes (incorrectly[47]) referred to as *false diffusion*. The problem is the frame of reference, since the CD scheme does not correspond to the exact solution, except for the case $\mathrm{Pe} = 0$. The additional diffusive term should rather be considered as a compensation for the error introduced by the CD scheme, which is necessary at higher Péclet numbers.

The idea of 'absorbing' a part of the convection into the diffusive term to ensure boundedness, has resulted in new discretization schemes, using the CD and UD schemes as limits. For $\mathrm{Pe} = 0$, we use the CD scheme and for $\mathrm{Pe} = \infty$, we use the UD scheme. In between, the correction depends on the Péclet number, e.g. the hybrid scheme employs the CD scheme for $|\mathrm{Pe}| < \mathrm{Pe}_c$ and the UD scheme otherwise [178]. A more sophisticated version is the exponential scheme [201], that reproduces the exact solution of steady-state convection-diffusion problems (on the grid points) [38]. The power-law scheme reproduces these results very well, but is computationally less expensive [179]. The accuracy of these methods is illustrated in figure 30 by considering the very simple case with fixed values $\phi_W = 1$, $\phi_E = 0$ and ϕ_P is the derived value, depending on the scheme.

[47] Following the discussion by Patankar [179, p. 105-109], false diffusion in steady problems can only be observed on two-dimensional grids. It occurs when the fluid flows at an angle of 45° to the grid lines, where numerical errors cause results that are more diffused than the exact solution. In the unsteady case, false diffusion may be observed in one-dimensional problems, which will be further discussed in appendix D.

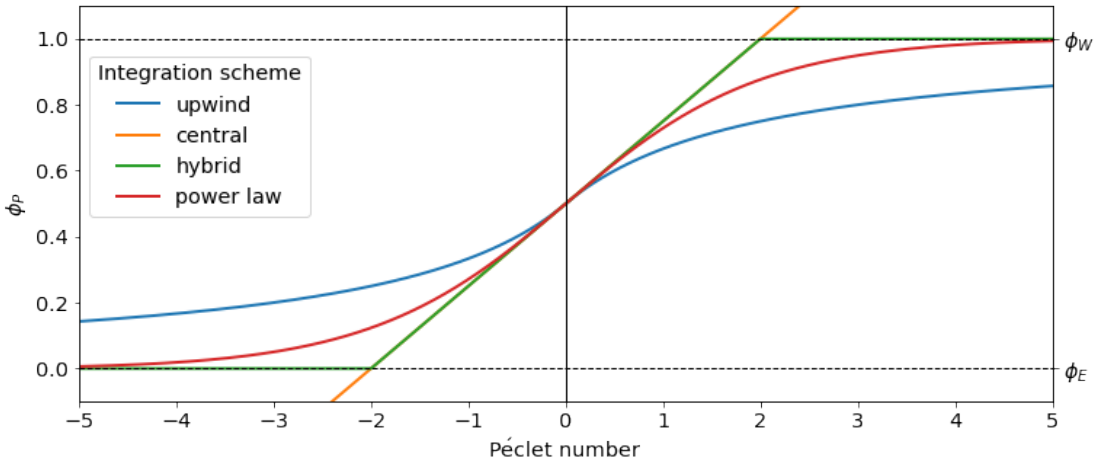

Figure 30: The resulting value of ϕ_P in the simple system with fixed values $\phi_W = 1$ and $\phi_E = 0$. In this case, ϕ_P depends on the numerical scheme, as indicated in the legend.

We observe that the flow is characterized by the Péclet number, which affects the accuracy of the discretization method. In section 5.1, we have shown that the diffusion coefficient is very small in our problem, corresponding to a very high Péclet number. This suggests that we can apply the very fast UD scheme without worrying about low accuracy. However, it will turn out that this statement is only true for time-independent problems. We will study the time-dependent case in further detail in appendix D.

D A mathematical analysis of numerical schemes

In this appendix, we provide the theoretical justification of the discussion in section 5.3.3, and we are guided by the book by Hirsch [187]. In order to generalize our results from steady to unsteady problems, we need a more rigorous definition of requirements on a numerical scheme. These requirements are of a more mathematical nature, but these are necessary to ensure physical outcomes. Also, as mentioned in appendix B, FVM schemes on uniform grids can be transformed into FDM schemes, which changes the interpretation of some terms, but lead to the same results. We will make use of this correspondence, since this discussion is a bit more straightforward in terms of a FDM scheme.

The first of three requirements is *consistency*, which means that the numerical scheme must tend to the exact differential equation as time and space steps, δt and δx, tend to zero. The second is *stability*, which means that for a given δt, $\delta x > 0$, all errors must remain bounded as iteration advances, with the number of time steps $n \to \infty$. The final requirement is *convergence*, which means that the numerical solution must tend to the exact solution as δt, $\delta x \to 0$. These requirements can be considered to be relations between the following concepts:

Condition	Relation between	and
Consistency	Discretized equation	Exact differential equation
Stability	Numerical solution	Exact solution of the discretized equation
Convergence	Numerical solution	Exact solution of the differential equation

Table 6: Overview of the concepts that are related by the requirements that we impose on the discretization.

The physical requirements that we studied before were mainly relations between the numerical solution and its exact solution. These conditions shall be replaced by Von Neumann analysis, which we will further discuss in section D.2. The accuracy requirement falls in the category of a consistency requirement, and as in appendix B, the Taylor expansion will be a valuable tool in this analysis. The most important relation is ensured by convergence, which ensures that our numerical result does actually correspond to the exact solution of the equation we study. As table 6 already suggests, if a discretization scheme[48] is consistent and stable, it is also convergent. This relation is described by the *Equivalence theorem of Lax*,

Theorem D.1 *For a well-posed initial value problem and a consistent discretization scheme, stability is the necessary and sufficient condition for convergence.*

A proof of this theorem can be found in [202]. This allows us to limit our attention to just the first two requirements, that can be analyzed with well-defined mathematical procedures.

D.1 Consistency

The requirement of consistency has already been mentioned to be somewhat related to the accuracy as studied before. In fact, we follow the same procedure of taylor expanding the function values of $\phi(x', t')$ around $\phi(x, t)$ for all $x' \neq x$ and $t' \neq t$. At this point, we make use of the discreteness of the problem to introduce a shorthand notation, $\phi(x_i, t_n) = \phi^i_n$, where i thus indicates a spatial index and n the time level. An important difference here is that we do not only expand in terms of space, but also time. As before, these expanded forms are entered into the numerical equation, leading to the original plus an extra term, the truncation error $\varepsilon_T = \mathcal{O}(\delta t^q, \delta x^p)$. The numbers q and p are the lowest order of temporal and spatial terms in the truncation error, i.e. the order of accuracy of the scheme.

Consistency can be stated in terms of the truncation error, so we require that $\varepsilon_T \to 0$ as δt, $\delta x \to 0$. This leads to the statement that a scheme needs to have a positive order of accuracy (in terms of the spatial *and* temporal errors) to be consistent. This requirement leads to some more insight if we perform the described procedure, so as an illustrative example, we consider the linear convection model,

$$\phi_t + a\phi_x = 0, \tag{D.1}$$

[48] Note that a discretization scheme thus consists of a choice of discretizing a differential equation *and* a choice of integration scheme, including setting δt and δx.

where the subscripts denote to temporal and spatial derivatives. We apply the UD scheme that has been introduced in spatial terms. The time dependency is straightforward up to first order, as a time step corresponds to an iteration step for a steady problem. The time-dependent UD scheme is thus

$$\frac{\phi_i^{n+1} - \phi_i^n}{\delta t} + a\frac{\phi_i^n - \phi_{i-1}^n}{\delta x} = 0. \tag{D.2}$$

The Taylor expansions that we need are those of ϕ_i^{n+1} and ϕ_{i-1}^n,

$$\phi_i^{n+1} = \phi_i^n + \delta t \left(\phi_t\right)_i^n + \delta t^2/2 \left(\phi_{tt}\right)_i^n + \mathcal{O}(\delta t^3) \tag{D.3}$$
$$\phi_{i-1}^n = \phi_i^n - \delta x \left(\phi_x\right)_i^n + \delta x^2/2 \left(\phi_{xx}\right)_i^n + \mathcal{O}(\delta x^3) \tag{D.4}$$

The substitution of these into equation D.2 leads to

$$\frac{\phi_i^{n+1} - \phi_i^n}{\delta t} + \frac{\phi_i^n - \phi_{i-1}^n}{\delta x} - \left(\phi_t\right)_i^n - a\left(\phi_x\right)_i^n = \delta t/2 \left(\phi_{tt}\right)_i^n - \delta x/2 \left(\phi_{xx}\right)_i^n + \mathcal{O}(\delta t^2, \delta x^2). \tag{D.5}$$

We observe the RHS of equation D.5 to be the truncation error ε_T, which is first order in both δt and δx. Note that these are not necessarily equal, e.g. the CD scheme with the same time discretization method has second order accuracy in terms of δx. This means that the overall order of accuracy of this scheme does now depend on relation between δt and δx. This relation is important when we want to increase accuracy or reduce the computational effort with minimal loss of accuracy.

It is important to note that we have not specified the meaning of ϕ so far. It can be interpreted as the exact variable we are solving for (satisfying equation D.1), or the exact solution of the numerical scheme (satisfying equation D.2). The first interpretation is common and rather straightforward, it shows us that the exact solution does not satisfy equation D.2, and the truncation error describes the deviation. The second interpretation leads to some more insight, and provides us with a differential equation for the variable ϕ_i^n, which we can use to obtain the *equivalent differential equation* (EDE). The equation we have obtained so far is

$$\left(\phi_t\right)_i^n + a\left(\phi_x\right)_i^n = -\delta t/2 \left(\phi_{tt}\right)_i^n + a\delta x/2 \left(\phi_{xx}\right)_i^n + \mathcal{O}(\delta t^2, \delta x^2), \tag{D.6}$$

which contains higher order derivatives in time and space. To obtain the EDE, it is common practice to eliminate the lowest order time derivatives by applying equation D.6 on itself, in this case abbreviating the RHS by $\mathcal{O}(\delta t, \delta x)$. Using its time derivative, we find

$$\begin{aligned}\left(\phi_{tt}\right)_i^n &= -a\left(\phi_{xt}\right)_i^n + \mathcal{O}(\delta t, \delta x) \\ &= -a\left(\left(\phi_t\right)_x\right)_i^n + \mathcal{O}(\delta t, \delta x) \\ &= a\left(\phi_{xx}\right)_i^n + \mathcal{O}(\delta t, \delta x)\end{aligned} \tag{D.7}$$

Now we insert this relation in equation D.6, and we find

$$\begin{aligned}\left(\phi_t\right)_i^n + a\left(\phi_x\right)_i^n &= \left(-a^2\delta t/2 + a\delta x/2\right)\left(\phi_{xx}\right)_i^n + \mathcal{O}(\delta t^2, \delta x^2) \\ &= a\delta x/2(1 - a\delta t/\delta x)\left(\phi_{xx}\right)_i^n + \mathcal{O}(\delta t^2, \delta x^2)\end{aligned} \tag{D.8}$$

This is what we refer to as the EDE up to the lowest order, the higher order terms can be taken into account in a similar way. What we learn from this equation requires a physical interpretation of the RHS of equation D.8. Comparing this result to the convection-diffusion equation, we see that our numerical method introduced a diffusive term. This phenomenon is what can correctly be referred to as false (or numerical) diffusion. Diffusion reduces

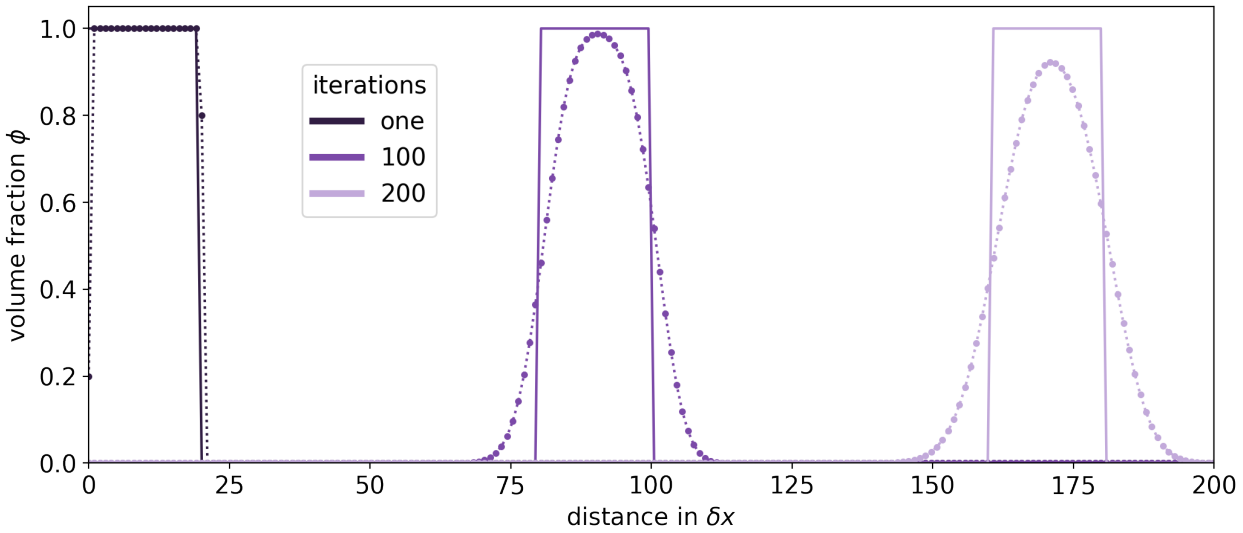

Figure 31: Comparison of the exact solution and numerical results of the FOU scheme for a one-dimensional convection problem, where an iteration corresponds to a time step. The effect of numerical diffusion is clearly visible, already for a low amount of time steps.

strong gradients and damps oscillations if the coefficient is positive, so if $1 - a\delta t/\delta x$ becomes negative, our scheme favors strong gradients and causes oscillations. This leads to a stability requirement for this scheme in terms of the CFL number $\sigma = a\delta t/\delta x$,

$$0 \leq \sigma \leq 1.$$

The effect of false diffusion clearly visible in figure 31, where the most extreme case of a travelling block is illustrated. The procedure of obtaining the EDE becomes a lot more involved for higher order schemes, a more detailed discussion is given in appendix E.1.

D.2 Stability

The next requirement that we study is the stability of a scheme, where a Von Neumann analysis is considered a sufficient condition for stability (for now). This analysis is based on a Fourier decomposition of the computed solution[49], which is a discrete function, so the Fourier representation is also discrete. We consider a spatial range of $[0, L]$, and use the mirror image to extend it to $[-L, L]$. If we imagine a sinusoidal wave, we conclude that the smallest wavelength that can be resolved on a uniform mesh of width δx is equal to $2\delta x$. The

[49]For the sake of completeness, we could also use the decomposition of the error. Consider a numerical scheme N with exact solution ϕ_i^n and numerical solution $\overline{\phi}_n^i$, then $N(\phi_i^n) = N(\overline{\phi}_n^i + \bar{\varepsilon} ni) = N(\overline{\phi}_n^i) + N(\bar{\varepsilon}_i^n) = N(\bar{\varepsilon}_i^n) = 0$. This shows that in the case of *linear* numerical schemes, the error satisfies the same relation.

largest wave length that we can represent in this range is equal to $2L$, which corresponds to a lower limit on the the wave number $k_{\min} = \pi/L$. The accessible wave numbers for our solution are thus $k_j = jk_{\min}$ for $j = 0, 1, 2, \ldots, N$, where N is the number of grid points. The parameter that we are interested in is the phase angle $\theta_j = k_j \delta x = j\pi/N$, which allows us to decompose any function on our finite mesh as

$$\phi_i^n = \sum_{j=-N}^{N} V_j^n \exp(\mathtt{i} k_j x_i) = \sum_{j=-N}^{N} V_j^n \exp(\mathtt{i} i \theta_j), \tag{D.9}$$

where we have used $\mathtt{i}$ to denote the imaginary unit, and V_j^n is the amplitude of the jth harmonic. This method now relies on the observation that for linear[50] schemes, each individual harmonic must also satisfy the discretized equation. Now we have all the necessary elements to express the Von Neumann stability condition: the amplitude of any harmonic may not grow indefinitely in time, i.e. when $n \to \infty$. A useful parameter in this analysis is thus the *amplification factor*,

$$|G| \equiv V^{n+1}/V^n,$$

in terms of which the Von Neumann stability condition reads

$$G \leq 1 \quad \text{for all values of } \theta_j, \quad \text{where} \quad j = -N, \ldots, +N$$

Since this condition must hold for each harmonic independently, we drop the j-dependence from equation D.9, and the condition must hold for all $-\pi \leq \theta \leq \pi$. This leads us to the following replacement of the discetized ϕ terms in our scheme,

$$\phi_{i+m}^{n+k} \Rightarrow V^{n+k} \exp(\mathtt{i}(i+m)\theta). \tag{D.10}$$

We see that for our relatively low-order schemes, we need just a few terms from this rather general definition. Also, each term will contain a factor $\exp(\mathtt{i} i\theta)$, the removal of which will greatly simplify the equations we are faced with. As a simple example, we treat the CD scheme of the pure convection problem, first order forward in time[51],

$$\phi_i^{n+1} = \phi_i^n - \sigma/2 \left(\phi_{i+1}^n - \phi_{i-1}^n\right), \tag{D.11}$$

where σ is the CFL number as introduced before. The procedure described above leads to the following:

$$\begin{aligned} V^{n+1} \exp(\mathtt{i} i\theta) &= V^n \exp(\mathtt{i} i\theta) - \sigma/2 \left(V^n \exp(\mathtt{i}(i+1)\theta) - V^n \exp(\mathtt{i}(i-1)\theta)\right) \\ V^{n+1} &= V^n - \sigma/2 \left(V^n \exp(\mathtt{i}\theta) - V^n \exp(-\mathtt{i}\theta)\right) \end{aligned} \tag{D.12}$$

[50] We stress that this condition is sufficient for linear schemes. For nonlinear schemes, we need to resort to a stability analysis in small enough regions to consider nonlinearities to be constant, allowing us to consider these to be locally linear. This implies that the Von Neumann stability analysis is merely a necessary condition for stability.

[51] Note that we use the term time-forward for its more intuitive definition, but this is more often referenced to as *explicit*. The alternative to explicit schemes are time-forward, or *implicit* schemes, which presents us with a trade-off in properties. Implicit schemes are generally more stable, allowing larger time steps, but are computationally much more expensive per iteration. In this thesis, we will deal only with explicit methods.

Using this result, we calculate the norm of the amplification factor.

$$G = 1 - \sigma/2 \cdot (2\mathtt{i}\sin(\theta))$$
$$|G| = \sqrt{G \cdot G^*} = 1 + \sigma^2 \sin^2(\theta) \tag{D.13}$$

We conclude that this scheme can never satisfy the stability condition except for $\theta = 0$, which would correspond to a single cell. Note that we discuss the stability of a discretized equation, which depends not only the scheme, but also on the problem that is being discretized.

D.2.1 Stability of the upwind-biased schemes

Having introduced the time-dependent problem, we must be more careful with the nomenclature of our schemes. By upwind-biased, we mean the generalization of the steady UD scheme, given by equation D.2, which we will refer to as first-order upwind (FOU). To study its stability, we follow the same procedure as above. For simplicity, we repeat equation D.2 in a more suggestive way,

$$\phi_i^{n+1} = \phi_i^n - \sigma\left(\phi_i^n - \phi_{i-1}^n\right) \tag{D.14}$$

From which the amplification factor is easily determined, and some algebra leads to

$$G = 1 - \sigma\left(1 - \exp(-\mathtt{i}\theta)\right) = (1 - \sigma) + \sigma\cos(\theta) - \mathtt{i}\sigma\sin(\theta). \tag{D.15}$$

We have written this in a way to suggest a representation in the imaginary plane. Notice that G is described by a circle with radius σ centered around the point $1-\sigma$ on the real line. We see that $|G| \leq 1$ if $0 \leq \sigma \leq 1$, which justifies the CFL condition in section 5.3.3.

This stability analysis applies to higher order schemes as well, and would result in $0 \leq \sigma \leq 2$ for the second order accurate upwind-biased scheme. In appendix E.1, we study the stability of this scheme in a more general context.

D.2.2 Numerical diffusion

To conclude our ongoing discussion of artificial diffusion effects, we define the *diffusion error* as the modulus of G. If it is smaller than one, there is an artificial damping of all harmonics. Since the the damping factor is $|G|^n$ after n time steps, this may have severe effects. Similar to the discussion of stability, we represent the diffusion error as a function of θ and σ. Choosing a mesh corresponding to smaller values of σ is undesirable for practical reasons, so a scheme that has a damping factor $|G|$ that is (very!) close to one for a large range of θ has a larger practical value. This leads to the remark that first-order schemes are useless for unsteady problems, since they are too diffusive [187, p. 311].

E Introducing diffusion in unsteady flow problems

There are many ways in which a diffusive term can be implemented, limited by the accuracy of the scheme and the number of neighboring nodes that are used. Thus we express these

different options in terms of one general scheme in the following way. Any explicit scheme that uses two time levels can be expressed as

$$\phi_i^{n+1} = \sum_j b_j \phi_{i+j}^n, \tag{E.1}$$

where the coefficients b_j define the scheme. We use the procedure as described in appendix D.1 to find the *equivalent differential equation* (EDE). Following Hirsch [187, p. 342 – 346], we find the following expression

$$\phi_t + a\phi_x = \sum_{m=p}^{\infty} a_{m+1} \delta x^m \left(\frac{\partial^{m+1}\phi}{\partial x^{m+1}} \right), \tag{E.2}$$

where p is the order of accuracy of the scheme and the coefficients a follow from the calculation of the EDE. Note that that the spatial accuracy corresponds to $a_m = 0$ for $m \leq p$. These coefficients are zero when the following conditions are met,

$$\sum_j b_j j^m = (-\sigma)^m \quad \text{for} \quad 0 \leq m \leq p. \tag{E.3}$$

Thus a scheme with accuracy p requires at least $p+1$ nodes, and their coefficients b_j are determined by these constraints. In order to introduce a diffusive term, we requires a free parameter. We need at least $p+2$ contributing nodes for a scheme of accuracy p with a diffusive term. We will come back to this in our discussion of higher order schemes.

For a scheme of accuracy p, we have the following coefficients a in equation E.2:

$$a_{p+1} = \frac{\delta x}{\delta t} \left(\sum_j b_j j^{p+1} - (-\sigma)^{p+1} \right) \frac{1}{(p+1)!}, \tag{E.4}$$

$$a_{p+2} = \frac{\delta x}{\delta t} \left(\sum_j b_j j^{p+2} - (-\sigma)^{p+2} \right) \frac{1}{(p+2)!} + \sigma a_{p+1}. \tag{E.5}$$

As before, we are interested in the lowest order truncation error term, which is equal to the lowest order δx term on the right-hand side of equation E.2. At this point, we recall the first step of the Von Neumann stability analysis, where we wrote ϕ as

$$\phi_i^n = \sum_{j=-N}^{N} V_j^n \exp(\mathtt{i} k_j x_i) = \sum_{j=-N}^{N} V_j^n \exp(\mathtt{i} i \theta_j). \tag{D.9, repeated}$$

We observe that even and odd powers of space derivatives of ϕ thus lead to real and imaginary contributions to the error, respectively. In the context of stability, we are interested in the real contribution, since that corresponds to the modulus of the amplification factor G as introduced in section D.2. For the problem under our consideration, the diffusion error is given by

$$\begin{aligned} \epsilon_D = |G| &= \exp\left[\sum_m (-)^m a_{2m} \phi^{2m} \frac{\delta t}{\delta x} \right], \\ &= 1 + \sum_m (-)^m a_{2m} \phi^{2m} \frac{\delta t}{\delta x} + \mathcal{O}(\phi^{4m}). \end{aligned} \tag{E.6}$$

With the stability condition $|G| \leq 1$ in mind, we find that (to lowest order in ϕ) we must have

$$(-)^l a_{2l} < 0, \tag{E.7}$$

where $2l$ corresponds to the lowest even order coefficient a that is nonzero. So if the accuracy p is uneven, $2l = p + 1$ and $2l = p + 2$ otherwise.

These are the constituents of our more general stability condition. As an example, let us consider the explicit, first-order accurate CD scheme. In the purely convective case, this scheme is given by D.11, which we showed to be *never* stable. If we add a centrally discretized diffusive term, we find a different result. In terms of equation E.1, this scheme has the following coefficients,

$$b_{-1} = \sigma/2 + \beta, \qquad b_0 = 1 - 2\beta, \qquad b_1 = -\sigma/2 + \beta, \tag{E.8}$$

where β describes the diffusivity of the system. Since the accuracy $p = 1$, we have that $2l = 2$, so we use equation E.4 and E.7 to find

$$a_2 = \frac{\delta x}{\delta t}\left(2\beta - \sigma^2\right)\frac{1}{2} > 0. \tag{E.9}$$

A further analysis, using ideas introduced in section D.2.2, shows that damping, i.e. $|G| < 1$, is desirable for high-frequency oscillations. In particular, this leads to $|G(\pi)| < 1$, which can be shown to correspond to $0 < \sum_j b_{2j} < 1$. This gives us the additional condition

$$0 < 1 - 2\beta < 1 \tag{E.10}$$

We wish to express these conditions in terms of parameters that have a clear significance in terms of our discretized problem. We recall our definition of the Péclet number, $\mathrm{Pe} = \rho u \delta x/\Gamma$, and the CFL number $\sigma = \rho u \delta t/\delta x$. Comparing equation E.1 and coefficients E.8 to the convection-diffusion problem (equation C.1 in section C), we see that $\beta = \Gamma \delta t/\delta x^2$. Combining these relations, we observe that $\beta = \sigma/\mathrm{Pe}$. We use this relation together with conditions E.9 and E.10 to find

$$\sigma < \frac{\mathrm{Pe}}{2} \qquad \text{and} \qquad \sigma < \frac{2}{\mathrm{Pe}}. \tag{E.11}$$

The same reasoning applies to any other explicit first-order accurate scheme. We compare these results to the FOU scheme with the same diffusive term, leading to the following coefficients,

$$b_{-1} = \sigma + \beta, \qquad b_0 = 1 - \sigma - 2\beta, \qquad b_1 = \beta. \tag{E.12}$$

These coefficients lead to the following conditions,

$$\sigma + 2\beta - \sigma^2 > 0 \qquad \text{and} \qquad 0 < 1 - \sigma - 2\beta < 1.$$

Using the relation $\beta = \mathrm{Pe}/\sigma$, we rewrite this to the following conditions,

$$\sigma < 1 + 2/\mathrm{Pe} \qquad \text{and} \qquad \sigma < (1 + 2/\mathrm{Pe})^{-1}. \tag{E.13}$$

For $\mathrm{Pe} > 0$, we see that the right conditions is always more stringent. We compare the regions of stability of these schemes in figure 32, and observe that the FOU scheme is a better choice for convection-dominated problems.

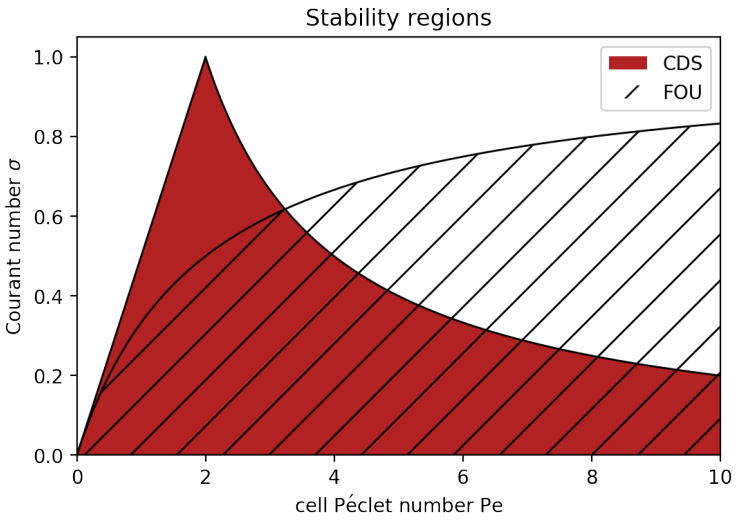

Figure 32: Regions of stability for convection-diffusion problems, where the convective term is either modeled by the central difference scheme (CDS) or the first order upwind scheme (FOU). Flows in the opposite direction have both a negative σ and Pe, and the diagram is mirrored. Note that the cutoff at Pe $= 10$ is arbitrary and the CDS and FOU stability boundaries converge to $\sigma = 0$ and 1, respectively.

E.1 Diffusion in higher order schemes

For schemes of second order accuracy, equation E.3 results in three conditions. So if we want to introduce a diffusive term in the SOU scheme, we need (at least) four nonzero coefficients. If we choose to define our scheme on the support[52] $j = \{-2, -1, 0, 1\}$, using the SOU scheme for the convective term, we have the following coefficients

$$b_{-2} = \sigma(\sigma - 1)/2 - \beta, \qquad b_{-1} = \sigma(2 - \sigma) + 3\beta, \qquad b_0 = (1 - \sigma)(2 - \sigma)/2 - 3\beta, \qquad b_1 = \beta \tag{E.14}$$

Note that the accuracy of our scheme is even, so the calculation of the stability region requires an extra step. We have that

$$a_3 = \frac{\delta x}{6\,\delta t}\left(6\beta + 2\sigma - 3\sigma^2 + \sigma^3\right), \tag{E.15}$$

$$a_4 = \frac{\delta x}{24\,\delta t}\left(-12\beta - 6\sigma + 7\sigma^2 - \sigma^4\right) + \sigma a_3,$$

$$a_4 = \frac{\delta x}{24\,\delta t}\left(-12\beta - 6\sigma + 24\beta\sigma + 15\sigma^2 - 12\sigma^3 + 3\sigma^4\right). \tag{E.16}$$

We simplify this by using $\beta = \sigma/\mathrm{Pe}$,

$$a_4 = \frac{\delta x}{8\,\delta t}\left(-2\sigma(1 + 2/\mathrm{Pe}) + \sigma^2(5 + 8/\mathrm{Pe}) - 4\sigma^3 + \sigma^4\right). \tag{E.17}$$

[52] In this context, 'on the support' means that we have nonzero coefficients b_j *only* when j lies in this support.

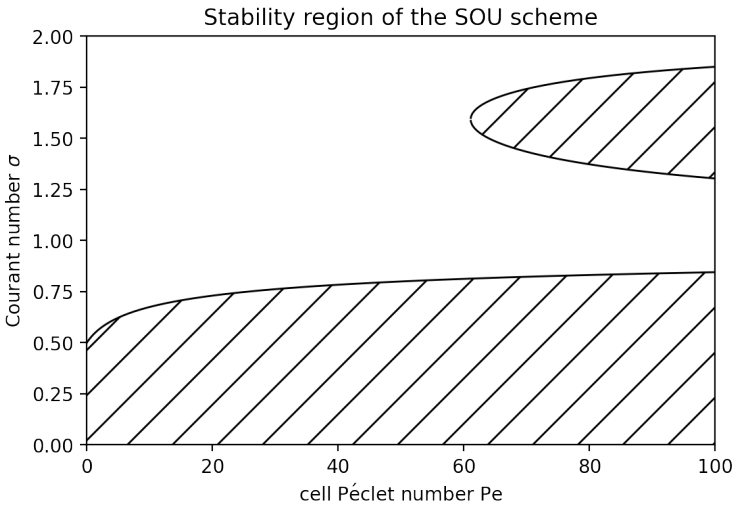

Figure 33: Regions of stability for convection-diffusion problems, for the scheme given by coefficients in equation E.14. Note that these two separate regions eventually merge, and when $\text{Pe} \to \infty$, the scheme is stable for $0 \leq \sigma \leq 2$.

Stability requires that $a_4 < 0$, so we calculate the roots of this polynomial in σ. The resulting region of stability is illustrated in figure 33. Interestingly, this scheme has distinct regions of stability, that merge in the limit of $\text{Pe} \to \infty$. There, the stability condition is independent of the diffusive term, and we find that $0 \leq \sigma \leq 2$. We conclude that our choice of discretizing the diffusive term does not affect the accuracy of the scheme, and with a good region of stability.

References

[1] R. Feynman, R. B. Leighton, and M. Sands, *The Feynman Lectures of Physics*, vol. I. Addison–Wesley, 1964.

[2] S. Slomkowski, J. V. Alemán, R. G. Gilbert, M. Hess, K. Horie, R. G. Jones, P. Kubisa, I. Meisel, W. Mormann, S. Penczek, *et al.*, "Terminology of polymers and polymerization processes in dispersed systems (iupac recommendations 2011)," *Pure and Applied Chemistry*, vol. 83, no. 12, pp. 2229–2259, 2011.

[3] C. P. Royall, M. A. Faers, S. L. Fussell, and J. E. Hallett, "Real space analysis of colloidal gels: triumphs, challenges and future directions," *Journal of Physics: Condensed Matter*, vol. 33, p. 453002, Aug. 2021.

[4] H. Barnes, J. Hutton, and K. Walters, *An Introduction to Rheology*, vol. 3 of *An Introduction to Rheology*. Elsevier Science, 1989.

[5] P. Coussot, *Rheometry of pastes, suspensions, and granular materials: applications in industry and environment*. John Wiley & Sons, 2005.

[6] J. Liang, Y. Ma, Y. Zheng, H. T. Davis, H.-T. Chang, D. Binder, S. Abbas, and F.-L. Hsu, "Solvent-induced crystal morphology transformation in a ternary soap system: sodium stearate crystalline fibers and platelets," *Langmuir*, vol. 17, no. 21, pp. 6447–6454, 2001.

[7] Z. Hu, M. Liao, Y. Chen, Y. Cai, L. Meng, Y. Liu, N. Lv, Z. Liu, and W. Yuan, "A novel preparation method for silicone oil nanoemulsions and its application for coating hair with silicone," *International journal of nanomedicine*, pp. 5719–5724, 2012.

[8] W. Russel, D. Saville, and W. Schowalter, "Colloidal dispersions cambridge univ," *Press, Cambridge*, 1989.

[9] B. Bai, Y. Liu, J.-P. Coste, and L. Li, "Preformed particle gel for conformance control: transport mechanism through porous media," *SPE Reservoir Evaluation & Engineering*, vol. 10, no. 02, pp. 176–184, 2007.

[10] R. Mezzenga and P. Fischer, "The self-assembly, aggregation and phase transitions of food protein systems in one, two and three dimensions," *Reports on Progress in Physics*, vol. 76, no. 4, p. 046601, 2013.

[11] J. Ubbink, "Soft matter approaches to structured foods: from "cook-and-look" to rational food design?," *Faraday discussions*, vol. 158, no. 1, pp. 9–35, 2012.

[12] J. L. Drury and D. J. Mooney, "Hydrogels for tissue engineering: scaffold design variables and applications," *Biomaterials*, vol. 24, no. 24, pp. 4337–4351, 2003.

[13] S. Rose, A. Prevoteau, P. Elzière, D. Hourdet, A. Marcellan, and L. Leibler, "Nanoparticle solutions as adhesives for gels and biological tissues," *Nature*, vol. 505, no. 7483, pp. 382–385, 2014.

[14] K. Haraguchi, T. Takehisa, and S. Fan, "Effects of clay content on the properties of nanocomposite hydrogels composed of poly (n-isopropylacrylamide) and clay," *Macromolecules*, vol. 35, no. 27, pp. 10162–10171, 2002.

[15] Z. Liu, L. Liu, H. Zhou, J. Wang, and L. Deng, "Toothpaste microstructure and rheological behaviors including aging and partial rejuvenation," *Korea-Australia Rheology Journal*, vol. 27, pp. 207–212, 2015.

[16] R. Buscall and L. R. White, "The consolidation of concentrated suspensions. part 1.—the theory of sedimentation," *Journal of the Chemical Society, Faraday Transactions 1: Physical Chemistry in Condensed Phases*, vol. 83, no. 3, pp. 873–891, 1987.

[17] R. Harich, T. Blythe, M. Hermes, E. Zaccarelli, A. Sederman, L. F. Gladden, and W. Poon, "Gravitational collapse of depletion-induced colloidal gels," *Soft Matter*, vol. 12, no. 19, pp. 4300–4308, 2016.

[18] L. Starrs, W. Poon, D. Hibberd, and M. Robins, "Collapse of transient gels in colloid-polymer mixtures," *Journal of Physics: Condensed Matter*, vol. 14, no. 10, p. 2485, 2002.

[19] S. Manley, J. Skotheim, L. Mahadevan, and D. A. Weitz, "Gravitational collapse of colloidal gels," *Physical review letters*, vol. 94, no. 21, p. 218302, 2005.

[20] P. Bartlett, L. J. Teece, and M. A. Faers, "Sudden collapse of a colloidal gel," *Physical Review E*, vol. 85, no. 2, p. 021404, 2012.

[21] P. Padmanabhan and R. Zia, "Gravitational collapse of colloidal gels: Non-equilibrium phase separation driven by osmotic pressure," *Soft Matter*, vol. 14, no. 17, pp. 3265–3287, 2018.

[22] A. Darras, A. K. Dasanna, T. John, G. Gompper, L. Kaestner, D. A. Fedosov, and C. Wagner, "Erythrocyte sedimentation: Collapse of a high-volume-fraction soft-particle gel," *Physical Review Letters*, vol. 128, feb 2022.

[23] Z. Varga, J. L. Hofmann, and J. W. Swan, "Modelling a hydrodynamic instability in freely settling colloidal gels," *Journal of Fluid Mechanics*, vol. 856, pp. 1014–1044, 2018.

[24] S. Buzzaccaro, E. Secchi, G. Brambilla, R. Piazza, and L. Cipelletti, "Equilibrium concentration profiles and sedimentation kinetics of colloidal gels under gravitational stress," *Journal of Physics: Condensed Matter*, vol. 24, no. 28, p. 284103, 2012.

[25] E. Secchi, S. Buzzaccaro, and R. Piazza, "Time-evolution scenarios for short-range depletion gels subjected to the gravitational stress," *Soft Matter*, vol. 10, no. 29, pp. 5296–5310, 2014.

[26] L. J. Teece, J. M. Hart, K. Y. N. Hsu, S. Gilligan, M. A. Faers, and P. Bartlett, "Gels under stress: The origins of delayed collapse," *Colloids and Surfaces A: Physicochemical and Engineering Aspects*, vol. 458, pp. 126–133, 2014.

[27] X. Zhou, *Onset of gravitational collapse of colloidal gels: an optical microscopy study*. PhD thesis, The University of Edinburgh, 2018.

[28] S. Kim and S. J. Karrila, *Microhydrodynamics: principles and selected applications*. Courier Corporation, 2013.

[29] J. Happel and H. Brenner, *Low Reynolds number hydrodynamics: with special applications to particulate media*, vol. 1. Springer Science & Business Media, 1983.

[30] T. B. Blijdenstein, E. van der Linden, T. van Vliet, and G. A. van Aken, "Scaling behavior of delayed demixing, rheology, and microstructure of emulsions flocculated by depletion and bridging," *Langmuir*, vol. 20, no. 26, pp. 11321–11328, 2004.

[31] A. Krall and D. Weitz, "Internal dynamics and elasticity of fractal colloidal gels," *Physical review letters*, vol. 80, no. 4, p. 778, 1998.

[32] W. C. Poon, L. Starrs, S. Meeker, A. Moussaid, R. M. Evans, P. Pusey, and M. Robins, "Delayed sedimentation of transient gels in colloid–polymer mixtures: dark-field observation, rheology and dynamic light scattering studies," *Faraday Discussions*, vol. 112, pp. 143–154, 1999.

[33] L. C. Johnson and R. N. Zia, "Phase mechanics of colloidal gels: osmotic pressure drives non-equilibrium phase separation," *Soft Matter*, vol. 17, no. 14, pp. 3784–3797, 2021.

[34] Z. Varga, G. Wang, and J. Swan, "The hydrodynamics of colloidal gelation," *Soft Matter*, vol. 11, no. 46, pp. 9009–9019, 2015.

[35] Z. Varga and J. Swan, "Hydrodynamic interactions enhance gelation in dispersions of colloids with short-ranged attraction and long-ranged repulsion," *Soft matter*, vol. 12, no. 36, pp. 7670–7681, 2016.

[36] Z. Varga and J. W. Swan, "Normal modes of weak colloidal gels," *Physical Review E*, vol. 97, no. 1, p. 012608, 2018.

[37] A. Razali, C. J. Fullerton, F. Turci, J. E. Hallett, R. L. Jack, and C. P. Royall, "Effects of vertical confinement on gelation and sedimentation of colloids," *Soft Matter*, vol. 13, no. 17, pp. 3230–3239, 2017.

[38] A. Veldman, "Computational fluid dynamics," *Lecture Notes, University of Groningen, The Netherlands*, 2013.

[39] G. G. Stokes, "On the effect of the internal friction of fluids on the motion of pendulums," *Trans. Cambridge Philos. Soc.*, vol. 9, pp. 8–106, 1856.

[40] Kraaiennest, "Forces on and streamlines around a sphere in stokes flow.," 2012. Accessed on May 28, 2024. Licensed under CC BY-SA 3.0.

[41] A. Constantin and R. Johnson, "Large-scale oceanic currents as shallow-water asymptotic solutions of the navier-stokes equation in rotating spherical coordinates," *Deep Sea Research Part II: Topical Studies in Oceanography*, vol. 160, pp. 32–40, 2019.

[42] D. McLean, "Continuum fluid mechanics and the navier-stokes equations," *Understanding Aerodynamics: Arguing from the Real Physics*, pp. 13–78, 2012.

[43] C. L. Fefferman, "Existence and smoothness of the navier-stokes equation," *The millennium prize problems*, vol. 57, p. 67, 2000.

[44] D. E. Rival, J. Kriegseis, P. Schaub, A. Widmann, and C. Tropea, "Characteristic length scales for vortex detachment on plunging profiles with varying leading-edge geometry," *Experiments in fluids*, vol. 55, pp. 1–8, 2014.

[45] O. Reynolds, "Xxix. an experimental investigation of the circumstances which determine whether the motion of water shall be direct or sinuous, and of the law of resistance in parallel channels," *Trans. Cambridge Philos. Soc.*, vol. 174, pp. 935–982, 1883.

[46] M. Potter, D. Wiggert, and B. Ramadan, *Mechanics of Fluids, SI Version*. Cengage Learning, 2012.

[47] A. Sommerfeld, "Ein beitrag zur hydrodynamischen erklaerung der turbulenten fluessigkeitsbewegungen," in *Atti del IV Congresso Internazionale dei Matematici (Roma, 6-11 Aprile 1908)*, vol. 3, pp. 116–124, 1909.

[48] S. Novopashin and A. Muriel, "Is the critical reynolds number universal?," *Journal of Experimental and Theoretical Physics*, vol. 95, pp. 262–265, 2002.

[49] K. Avila, D. Moxey, A. De Lozar, M. Avila, D. Barkley, and B. Hof, "The onset of turbulence in pipe flow," *Science*, vol. 333, no. 6039, pp. 192–196, 2011.

[50] A. Einstein, "Ist die trägheit eines körpers von seinem energiegehalt abhängig," *Annalen der Physik*, vol. 18, no. 639, pp. 67–71, 1905.

[51] M. Smoluchowski, "On the practical applicability of stokes' law of resistance, and the modifications of it required in certain cases," in *Proceedings of the Fifth International Congress of Mathematicians (Cambridge, 22-28 August 1912)*, vol. 2, pp. 192–201, University Press, 1913.

[52] G. Batchelor, "Sedimentation in a dilute dispersion of spheres," *Journal of fluid mechanics*, vol. 52, no. 2, pp. 245–268, 1972.

[53] A. Maude and R. Whitmore, "A generalized theory of sedimentation," *British journal of applied physics*, vol. 9, no. 12, p. 477, 1958.

[54] F. Concha A., *Solid-Liquid Separation in the Mining Industry*. Springer International Publishing, 2014.

[55] M. G. Noro and D. Frenkel, "Extended corresponding-states behavior for particles with variable range attractions," *The Journal of Chemical Physics*, vol. 113, no. 8, pp. 2941–2944, 2000.

[56] J. A. Barker and D. Henderson, "What is "liquid"? understanding the states of matter," *Reviews of Modern Physics*, vol. 48, no. 4, p. 587, 1976.

[57] K. W. Torre and J. de Graaf, "Hydrodynamic lubrication in colloidal gels," *Soft Matter*, vol. 19, no. 38, pp. 7388–7398, 2023.

[58] K. Miyazaki, K. Schweizer, D. Thirumalai, R. Tuinier, and E. Zaccarelli, "The asakura–oosawa theory: Entropic forces in physics, biology, and soft matter," *The Journal of Chemical Physics*, vol. 156, no. 8, 2022.

[59] A. Baer, S. E. Wawra, K. Bielmeier, M. J. Uttinger, D. M. Smith, W. Peukert, J. Walter, and A.-S. Smith, "The stokes–einstein–sutherland equation at the nanoscale revisited," *Small*, vol. 20, no. 6, p. 2304670, 2024.

[60] S. Li, H. Jiang, and Z. Hou, "Effects of hydrodynamic interactions on the crystallization of passive and active colloidal systems," *Soft Matter*, vol. 11, no. 28, pp. 5712–5718, 2015.

[61] A. Furukawa and H. Tanaka, "Key role of hydrodynamic interactions in colloidal gelation," *Physical review letters*, vol. 104, no. 24, p. 245702, 2010.

[62] J. K. Whitmer and E. Luijten, "Influence of hydrodynamics on cluster formation in colloid- polymer mixtures," *The Journal of Physical Chemistry B*, vol. 115, no. 22, pp. 7294–7300, 2011.

[63] R. Yamamoto, K. Kim, Y. Nakayama, K. Miyazaki, and D. R. Reichman, "On the role of hydrodynamic interactions in colloidal gelation," *Journal of the Physical Society of Japan*, vol. 77, no. 8, pp. 084804–084804, 2008.

[64] H. Tanaka and T. Araki, "Simulation method of colloidal suspensions with hydrodynamic interactions: Fluid particle dynamics," *Physical review letters*, vol. 85, no. 6, p. 1338, 2000.

[65] C. P. Royall, J. Eggers, A. Furukawa, and H. Tanaka, "Probing colloidal gels at multiple length scales: The role of hydrodynamics," *Physical review letters*, vol. 114, no. 25, p. 258302, 2015.

[66] A. J. Ladd, "Hydrodynamic screening in sedimenting suspensions of non-brownian spheres," *Physical review letters*, vol. 76, no. 8, p. 1392, 1996.

[67] P. Ahlrichs, R. Everaers, and B. Dünweg, "Screening of hydrodynamic interactions in semidilute polymer solutions: A computer simulation study," *Physical Review E*, vol. 64, no. 4, p. 040501, 2001.

[68] L. Turetta and M. Lattuada, "The role of hydrodynamic interactions on the aggregation kinetics of sedimenting colloidal particles," *Soft Matter*, vol. 18, no. 8, pp. 1715–1730, 2022.

[69] H. C. Hamaker, "The london—van der waals attraction between spherical particles," *physica*, vol. 4, no. 10, pp. 1058–1072, 1937.

[70] J. De Graaf, W. C. Poon, M. J. Haughey, and M. Hermes, "Hydrodynamics strongly affect the dynamics of colloidal gelation but not gel structure," *Soft Matter*, vol. 15, no. 1, pp. 10–16, 2019.

[71] G. J. Kynch, "A theory of sedimentation," *Transactions of the Faraday society*, vol. 48, pp. 166–176, 1952.

[72] A. D. Watson, G. C. Barker, and M. M. Robins, "Sedimentation in bidisperse and polydisperse colloids," *Journal of colloid and interface science*, vol. 286, no. 1, pp. 176–186, 2005.

[73] K. Sugiyama, S. Ii, S. Takeuchi, S. Takagi, and Y. Matsumoto, "A full eulerian finite difference approach for solving fluid–structure coupling problems," *Journal of Computational Physics*, vol. 230, no. 3, pp. 596–627, 2011.

[74] M. E. Rosti and L. Brandt, "Numerical simulation of turbulent channel flow over a viscous hyper-elastic wall," *Journal of Fluid Mechanics*, vol. 830, pp. 708–735, 2017.

[75] M. E. Rosti and L. Brandt, "Suspensions of deformable particles in a couette flow," *Journal of Non-Newtonian Fluid Mechanics*, vol. 262, pp. 3–11, 2018.

[76] M. H. Lee and E. M. Furst, "Response of a colloidal gel to a microscopic oscillatory strain," *Physical Review E*, vol. 77, no. 4, p. 041408, 2008.

[77] E. M. Furst and J. P. Pantina, "Yielding in colloidal gels due to nonlinear microstructure bending mechanics," *Physical Review E*, vol. 75, no. 5, p. 050402, 2007.

[78] V. Trappe and D. Weitz, "Scaling of the viscoelasticity of weakly attractive particles," *Physical review letters*, vol. 85, no. 2, p. 449, 2000.

[79] J. Schummer, "The chemical core of chemistry i: A conceptual approach," *Hyle*, vol. 4, no. 2, pp. 129–162, 1998.

[80] N. D. Jespersen and A. Hyslop, *Chemistry: The molecular nature of matter*. John Wiley & Sons, 2021.

[81] A. Morozov and S. E. Spagnolie, "Introduction to complex fluids," *Complex Fluids in Biological Systems: Experiment, Theory, and Computation*, pp. 3–52, 2015.

[82] "Laminar flow parallel to a no-slip boundary at $y = 0$.." Accessed on May 31, 2024. Public domain.

[83] G. K. Batchelor, *An introduction to fluid dynamics*. Cambridge university press, 1967.

[84] M. A. Meyers and K. K. Chawla, *Mechanical behavior of materials*. Cambridge university press, 2008.

[85] M. Nabizadeh and S. Jamali, "Life and death of colloidal bonds control the rate-dependent rheology of gels," *Nature Communications*, vol. 12, no. 1, p. 4274, 2021.

[86] L. D. Landau and E. M. Lifshitz, *Course of theoretical physics*, vol. 6, Fluid Mechanics. Pergamon Press, 1 ed., 1959.

[87] K. W. Torre and J. de Graaf, "Delayed gravitational collapse of attractive colloidal suspensions," 2024.

[88] A. P. Eberle, R. Castañeda-Priego, J. M. Kim, and N. J. Wagner, "Dynamical arrest, percolation, gelation, and glass formation in model nanoparticle dispersions with thermoreversible adhesive interactions," *Langmuir*, vol. 28, no. 3, pp. 1866–1878, 2012.

[89] W. Richtering and B. R. Saunders, "Gel architectures and their complexity," *Soft Matter*, vol. 10, no. 21, pp. 3695–3702, 2014.

[90] S. Summonte, G. F. Racaniello, A. Lopedota, N. Denora, and A. Bernkop-Schnürch, "Thiolated polymeric hydrogels for biomedical application: Cross-linking mechanisms," *Journal of Controlled Release*, vol. 330, pp. 470–482, 2021.

[91] Y.-R. Luo, *Comprehensive handbook of chemical bond energies*. CRC press, 2007.

[92] T. L. Cottrell, "The strengths of chemical bonds," *(No Title)*, 1958.

[93] E. Zaccarelli, "Colloidal gels: equilibrium and non-equilibrium routes," *Journal of Physics: Condensed Matter*, vol. 19, p. 323101, July 2007.

[94] M. J. Solomon and P. Varadan, "Dynamic structure of thermoreversible colloidal gels of adhesive spheres," *Physical Review E*, vol. 63, no. 5, p. 051402, 2001.

[95] J. R. Weeks, J. S. van Duijneveldt, and B. Vincent, "Formation and collapse of gels of sterically stabilized colloidal particles," *Journal of Physics: Condensed Matter*, vol. 12, no. 46, p. 9599, 2000.

[96] R. D. Eastham, "The erythrocyte sedimentation rate and the plasma viscosity," *Journal of Clinical Pathology*, vol. 7, no. 2, p. 164, 1954.

[97] S. E. Bedell and B. T. Bush, "Erythrocyte sedimentation rate. from folklore to facts," *The American journal of medicine*, vol. 78, no. 6, pp. 1001–1009, 1985.

[98] L. J. Teece, M. A. Faers, and P. Bartlett, "Ageing and collapse in gels with long-range attractions," *Soft Matter*, vol. 7, no. 4, pp. 1341–1351, 2011.

[99] J. C. F. Toledano, F. Sciortino, and E. Zaccarelli, "Colloidal systems with competing interactions: from an arrested repulsive cluster phase to a gel," *Soft Matter*, vol. 5, no. 12, pp. 2390–2398, 2009.

[100] A. P. Eberle, N. J. Wagner, and R. Castaneda-Priego, "Dynamical arrest transition in nanoparticle dispersions with short-range interactions," *Physical review letters*, vol. 106, no. 10, p. 105704, 2011.

[101] B. Ruzicka, E. Zaccarelli, L. Zulian, R. Angelini, M. Sztucki, A. Moussaïd, T. Narayanan, and F. Sciortino, "Observation of empty liquids and equilibrium gels in a colloidal clay," *Nature materials*, vol. 10, no. 1, pp. 56–60, 2011.

[102] I. Saika-Voivod, H. M. King, P. Tartaglia, F. Sciortino, and E. Zaccarelli, "Silica through the eyes of colloidal models—when glass is a gel," *Journal of Physics: Condensed Matter*, vol. 23, no. 28, p. 285101, 2011.

[103] F. Sciortino, S. V. Buldyrev, C. De Michele, G. Foffi, N. Ghofraniha, E. La Nave, A. Moreno, S. Mossa, I. Saika-Voivod, P. Tartaglia, *et al.*, "Routes to colloidal gel formation," *Computer physics communications*, vol. 169, no. 1-3, pp. 166–171, 2005.

[104] E. Zaccarelli, S. Buldyrev, E. La Nave, A. Moreno, I. Saika-Voivod, F. Sciortino, and P. Tartaglia, "Model for reversible colloidal gelation," *Physical review letters*, vol. 94, no. 21, p. 218301, 2005.

[105] E. Bianchi, J. Largo, P. Tartaglia, E. Zaccarelli, and F. Sciortino, "Phase diagram of patchy colloids: Towards empty liquids," *Physical review letters*, vol. 97, no. 16, p. 168301, 2006.

[106] M. E. Helgeson, Y. Gao, S. E. Moran, J. Lee, M. Godfrin, A. Tripathi, A. Bose, and P. S. Doyle, "Homogeneous percolation versus arrested phase separation in attractively-driven nanoemulsion colloidal gels," *Soft matter*, vol. 10, no. 17, pp. 3122–3133, 2014.

[107] V. J. Anderson and H. N. Lekkerkerker, "Insights into phase transition kinetics from colloid science," *Nature*, vol. 416, no. 6883, pp. 811–815, 2002.

[108] S. F. Edwards and D. V. Grinev, "constrained dynamics on microscopic and macroscopic scales," in *Jamming and rheology* (A. J. Liu and S. R. Nagel, eds.), CRC Press, 2001.

[109] A. J. Liu and S. R. Nagel, "Jamming is not just cool any more," *Nature*, vol. 396, no. 6706, pp. 21–22, 1998.

[110] V. Trappe, V. Prasad, L. Cipelletti, P. Segre, and D. A. Weitz, "Jamming phase diagram for attractive particles," *Nature*, vol. 411, no. 6839, pp. 772–775, 2001.

[111] P. N. Pusey and W. van Megen, "Observation of a glass transition in suspensions of spherical colloidal particles," *Physical review letters*, vol. 59, no. 18, p. 2083, 1987.

[112] S. Ren and C. Sorensen, "Relaxations in gels: Analogies to α and β relaxations in glasses," *Physical review letters*, vol. 70, no. 11, p. 1727, 1993.

[113] D. Bonn, H. Kellay, H. Tanaka, G. Wegdam, and J. Meunier, "Laponite: What is the difference between a gel and a glass?," *Langmuir*, vol. 15, no. 22, pp. 7534–7536, 1999.

[114] E.-J. Donth, *The Glass Transition: Relaxation Dynamics in Liquids and Disordered Materials*. Springer-Verslag, 2001.

[115] P.-G. De Gennes, *Scaling concepts in polymer physics*. Cornell university press, 1979.

[116] H. Tanaka, J. Meunier, and D. Bonn, "Nonergodic states of charged colloidal suspensions: Repulsive and attractive glasses and gels," *Phys. Rev. E*, vol. 69, p. 031404, Mar 2004.

[117] S. K. Kumar and J. F. Douglas, "Gelation in physically associating polymer solutions," *Phys. Rev. Lett.*, vol. 87, p. 188301, Oct 2001.

[118] P. J. Lu, E. Zaccarelli, F. Ciulla, A. B. Schofield, F. Sciortino, and D. A. Weitz, "Gelation of particles with short-range attraction," *Nature*, vol. 453, no. 7194, pp. 499–503, 2008.

[119] M. A. Miller and D. Frenkel, "Phase diagram of the adhesive hard sphere fluid," *The Journal of chemical physics*, vol. 121, no. 1, pp. 535–545, 2004.

[120] K. N. Pham, A. M. Puertas, J. Bergenholtz, S. U. Egelhaaf, A. Moussaıd, P. N. Pusey, A. B. Schofield, M. E. Cates, M. Fuchs, and W. C. Poon, "Multiple glassy states in a simple model system," *Science*, vol. 296, no. 5565, pp. 104–106, 2002.

[121] M. Cates, "Arrest and flow of colloidal glasses," in *Annales Henri Poincaré*, vol. 4, pp. 647–661, Springer, 2003.

[122] A. Stradner, H. Sedgwick, F. Cardinaux, W. C. Poon, S. U. Egelhaaf, and P. Schurtenberger, "Equilibrium cluster formation in concentrated protein solutions and colloids," *Nature*, vol. 432, no. 7016, pp. 492–495, 2004.

[123] H. Sedgwick, S. Egelhaaf, and W. Poon, "Clusters and gels in systems of sticky particles," *Journal of Physics: Condensed Matter*, vol. 16, no. 42, p. S4913, 2004.

[124] H. Sedgwick, K. Kroy, A. Salonen, M. Robertson, S. Egelhaaf, and W. Poon, "Non-equilibrium behavior of sticky colloidal particles: beads, clusters and gels," *The European Physical Journal E*, vol. 16, pp. 77–80, 2005.

[125] M. Laurati, G. Petekidis, N. Koumakis, F. Cardinaux, A. B. Schofield, J. M. Brader, M. Fuchs, and S. U. Egelhaaf, "Structure, dynamics, and rheology of colloid-polymer mixtures: From liquids to gels," *The Journal of chemical physics*, vol. 130, no. 13, 2009.

[126] J. Conrad, H. Wyss, V. Trappe, S. Manley, K. Miyazaki, L. Kaufman, A. B. Schofield, D. Reichman, and D. Weitz, "Arrested fluid-fluid phase separation in depletion systems: Implications of the characteristic length on gel formation and rheology," *Journal of rheology*, vol. 54, no. 2, pp. 421–438, 2010.

[127] F. Cardinaux, T. Gibaud, A. Stradner, and P. Schurtenberger, "Interplay between spinodal decomposition and glass formation in proteins exhibiting short-range attractions," *Physical Review Letters*, vol. 99, no. 11, p. 118301, 2007.

[128] A. Vrij, "Polymers at interfaces and the interactions in colloidal dispersions," *Pure and Applied Chemistry*, vol. 48, no. 4, pp. 471–483, 1976.

[129] S. Asakura and F. Oosawa, "On interaction between two bodies immersed in a solution of macromolecules," *The Journal of chemical physics*, vol. 22, no. 7, pp. 1255–1256, 1954.

[130] S. Asakura and F. Oosawa, "Interaction between particles suspended in solutions of macromolecules," *Journal of polymer science*, vol. 33, no. 126, pp. 183–192, 1958.

[131] C. Pathmamanoharan, H. De Hek, and A. Vrij, "Phase separation in mixtures of organophilic spherical silica particles and polymer molecules in good solvents," *Colloid and Polymer Science*, vol. 259, no. 7, pp. 769–771, 1981.

[132] C. Bechinger, D. Rudhardt, P. Leiderer, R. Roth, and S. Dietrich, "Understanding depletion forces beyond entropy," *Physical review letters*, vol. 83, no. 19, p. 3960, 1999.

[133] S. Sukenik, L. Sapir, and D. Harries, "Balance of enthalpy and entropy in depletion forces," *Current opinion in colloid & interface science*, vol. 18, no. 6, pp. 495–501, 2013.

[134] J. Bergenholtz, W. C. Poon, and M. Fuchs, "Gelation in model colloid-polymer mixtures," *Langmuir*, vol. 19, no. 10, pp. 4493–4503, 2003.

[135] K. T. Saud, M. Ganesan, and M. J. Solomon, "Yield stress behavior of colloidal gels with embedded active particles," *Journal of Rheology*, vol. 65, no. 2, pp. 225–239, 2021.

[136] P. Pusey, J. Hansen, D. Levesque, and J. Zinn-Justin, "Liquids, freezing and the glass transition," 1991.

[137] L. Cipelletti, S. Manley, R. Ball, and D. Weitz, "Universal aging features in the restructuring of fractal colloidal gels," *Physical review letters*, vol. 84, no. 10, p. 2275, 2000.

[138] S. Manley, B. Davidovitch, N. R. Davies, L. Cipelletti, A. Bailey, R. J. Christianson, U. Gasser, V. Prasad, P. Segre, M. Doherty, *et al.*, "Time-dependent strength of colloidal gels," *Physical review letters*, vol. 95, no. 4, p. 048302, 2005.

[139] J. Y. Huh, M. L. Lynch, and E. M. Furst, "Microscopic structure and collapse of depletion-induced gels in vesicle-polymer mixtures," *Physical Review E*, vol. 76, no. 5, p. 051409, 2007.

[140] P. Tartaglia, "Models of gel-forming colloids," in *AIP Conference Proceedings*, vol. 982, pp. 295–303, American Institute of Physics, 2008.

[141] J. de Graaf, K. W. Torre, W. C. Poon, and M. Hermes, "Hydrodynamic stability criterion for colloidal gelation under gravity," *Physical Review E*, vol. 107, no. 3, p. 034608, 2023.

[142] R. P. Chapuis and M. Aubertin, *Predicting the coefficient of permeability of soils using the Kozeny-Carman equation*. École polytechnique de Montréal Montréal, 2003.

[143] J. Kozeny, "Ueber kapillare leitung des wassers im boden," *Sitzungsberichte der Akademie der Wissenschaften in Wien*, vol. 136, p. 271, 1927.

[144] G. M. Fair, L. P. Hatch, and H. E. Hudson, "Fundamental factors governing the streamline flow of water through sand [with discussion]," *Journal (American Water Works Association)*, vol. 25, no. 11, pp. 1551–1565, 1933.

[145] H. Darcy, *Les fontaines publiques de Dijon*. Dalmomt, Victor, 1856.

[146] S. Whitaker, "Flow in porous media i: A theoretical derivation of darcy's law," *Transport in porous media*, vol. 1, pp. 3–25, 1986.

[147] P. Xu and B. Yu, "Developing a new form of permeability and kozeny–carman constant for homogeneous porous media by means of fractal geometry," *Advances in water resources*, vol. 31, no. 1, pp. 74–81, 2008.

[148] F. J. Valdes-Parada, J. A. Ochoa-Tapia, and J. Alvarez-Ramirez, "Validity of the permeability carman–kozeny equation: A volume averaging approach," *Physica A: Statistical Mechanics and its Applications*, vol. 388, no. 6, pp. 789–798, 2009.

[149] B. Xiao, W. Wang, X. Zhang, G. Long, J. Fan, H. Chen, and L. Deng, "A novel fractal solution for permeability and kozeny-carman constant of fibrous porous media made up of solid particles and porous fibers," *Powder Technology*, vol. 349, pp. 92–98, 2019.

[150] G. Brambilla, S. Buzzaccaro, R. Piazza, L. Berthier, and L. Cipelletti, "Highly nonlinear dynamics in a slowly sedimenting colloidal gel," *Physical review letters*, vol. 106, no. 11, p. 118302, 2011.

[151] V. Trappe and P. Sandkühler, "Colloidal gels—low-density disordered solid-like states," *Current opinion in colloid & interface science*, vol. 8, no. 6, pp. 494–500, 2004.

[152] P. J. Lu and D. A. Weitz, "Colloidal particles: Crystals, glasses, and gels," *Annu. Rev. Condens. Matter Phys.*, vol. 4, no. 1, pp. 217–233, 2013.

[153] V. Prasad, V. Trappe, A. Dinsmore, P. Segre, L. Cipelletti, and D. Weitz, "Rideal lecture, universal features of the fluid to solid transition for attractive colloidal particles," *Faraday discussions*, vol. 123, pp. 1–12, 2003.

[154] J. Ruiz-Franco, F. Camerin, N. Gnan, and E. Zaccarelli, "Tuning the rheological behavior of colloidal gels through competing interactions," *Physical Review Materials*, vol. 4, no. 4, p. 045601, 2020.

[155] D. Voet, J. G. Voet, C. W. Pratt, *et al.*, *Fundamentals of biochemistry*. Wiley New York, 2002.

[156] E. Meijer, "Jacobus henricus van't hoff; hundred years of impact on stereochemistry in the netherlands," *Angewandte Chemie International Edition*, vol. 40, no. 20, pp. 3783–3789, 2001.

[157] N. J. Tro, T. D. Fridgen, L. Shaw, and R. S. Boikess, *Chemistry: A molecular approach*, vol. 5. Pearson Boston, MA, 2017.

[158] J. D. Van der Waals, *Over de Continuiteit van den Gas-en Vloeistoftoestand*, vol. 1. Sijthoff, 1873.

[159] B. F. Dodge, *Chemical engineering thermodynamics*. McGraw Hill, 1944.

[160] K. Shah and G. Thodos, "A comparison of equations of state," *Industrial & Engineering Chemistry*, vol. 57, no. 3, pp. 30–37, 1965.

[161] v. C. Dieterici, "Ueber den kritischen zustand," *Annalen der Physik*, vol. 305, no. 11, pp. 685–705, 1899.

[162] R. J. Sadus, "Equations of state for fluids: The dieterici approach revisited," *The Journal of Chemical Physics*, vol. 115, no. 3, pp. 1460–1462, 2001.

[163] I. Cachadina, A. Mulero, and M. Silbert, "Comment on "equations of state for fluids: The dieterici approach revisited"[j. chem. phys. 115, 1460 (2001)]," *The Journal of chemical physics*, vol. 120, no. 18, pp. 8868–8869, 2004.

[164] R. J. Sadus, "Response to "comment on 'equations of state for fluids: The dieterici approach revisited'"[j. chem. phys. 115, 1460 (2001)]," *The Journal of Chemical Physics*, vol. 120, no. 18, pp. 8870–8870, 2004.

[165] R. J. Sadus, "The dieterici alternative to the van der waals approach for equations of state: second virial coefficients," *Physical Chemistry Chemical Physics*, vol. 4, no. 6, pp. 919–921, 2002.

[166] L. D. Landau and E. M. Lifshitz, *Course of theoretical physics.*, vol. 5, Statistical physics. Pergamon Press, 1 ed., 1959.

[167] R. Munn, "Role of the elastic constants in negative thermal expansion of axial solids," *Journal of Physics C: Solid State Physics*, vol. 5, no. 5, p. 535, 1972.

[168] D. Wanta, W. T. Smolik, J. Kryszyn, P. Wróblewski, and M. Midura, "A finite volume method using a quadtree non-uniform structured mesh for modeling in electrical capacitance tomography," *Proceedings of the National Academy of Sciences, India Section A: Physical Sciences*, vol. 92, no. 3, pp. 443–452, 2022.

[169] D. Zhao, H. Shen, J. Lai, and G. T. III, "Approximate riemann solvers in fvm for 2d hydraulic shock wave modeling," *Journal of Hydraulic Engineering*, vol. 122, no. 12, pp. 692–702, 1996.

[170] G. Marck, M. Nemer, and J.-L. Harion, "Topology optimization of heat and mass transfer problems: laminar flow," *Numerical Heat Transfer, Part B: Fundamentals*, vol. 63, no. 6, pp. 508–539, 2013.

[171] R. Eymard, R. Herbin, and A. Michel, "Mathematical study of a petroleum-engineering scheme," *ESAIM: Mathematical Modelling and Numerical Analysis*, vol. 37, no. 6, pp. 937–972, 2003.

[172] R. Eymard, T. Gallouët, and R. Herbin, "Finite volume methods," *Handbook of numerical analysis*, vol. 7, pp. 713–1018, 2000.

[173] H. K. Versteeg and W. Malalasekera, *An introduction to computational fluid dynamics: the finite volume method*. Pearson education, 2007.

[174] P. J. Roache, *Computational fluid dynamics*. Hermosa Publishers, 1976.

[175] A. K. Runchal, "Brian spalding: Cfd and reality–a personal recollection," *International Journal of Heat and Mass Transfer*, vol. 52, no. 17-18, pp. 4063–4073, 2009.

[176] A. Gosman, W. Pun, A. Runchal, D. Spalding, and M. Wolfshtein, *Heat and Mass Transfer in Recirculating Flows*. Academic Press, 1969.

[177] J. Tan, "An upwind finite volume method for convection-diffusion equations on rectangular mesh," *Chaos, Solitons & Fractals*, vol. 118, pp. 159–165, 2019.

[178] D. B. Spalding, "A novel finite difference formulation for differential expressions involving both first and second derivatives," *International Journal for Numerical Methods in Engineering*, vol. 4, no. 4, pp. 551–559, 1972.

[179] S. V. Patankar, *Numerical heat transfer and fluid flow*. Hemisphere Publishing Corporation, McGraw Hill, 1980.

[180] B. P. Leonard, "A stable and accurate convective modelling procedure based on quadratic upstream interpolation," *Computer methods in applied mechanics and engineering*, vol. 19, no. 1, pp. 59–98, 1979.

[181] B. P. Leonard, "Simple high-accuracy resolution program for convective modelling of discontinuities," *International journal for numerical methods in fluids*, vol. 8, no. 10, pp. 1291–1318, 1988.

[182] F.-S. Lien and M. Leschziner, "Upstream monotonic interpolation for scalar transport with application to complex turbulent flows," *International Journal for Numerical Methods in Fluids*, vol. 19, no. 6, pp. 527–548, 1994.

[183] P. L. Roe, "Some contributions to the modelling of discontinuous flows," *Large-scale computations in fluid mechanics*, pp. 163–193, 1985.

[184] P. K. Sweby, "High resolution schemes using flux limiters for hyperbolic conservation laws," *SIAM journal on numerical analysis*, vol. 21, no. 5, pp. 995–1011, 1984.

[185] G. D. Van Albada, B. Van Leer, and W. Roberts Jr, "A comparative study of computational methods in cosmic gas dynamics," *Astronomy and Astrophysics, vol. 108, no. 1, Apr. 1982, p. 76-84.*, vol. 108, pp. 76–84, 1982.

[186] B. Van Leer, "Towards the ultimate conservative difference scheme. ii. monotonicity and conservation combined in a second-order scheme," *Journal of computational physics*, vol. 14, no. 4, pp. 361–370, 1974.

[187] C. Hirsch, *Numerical computation of internal and external flows*, vol. 2, Computational methods for inviscid and viscous flows. John Wiley & Sons, 1990.

[188] P. D. Lax and B. Wendroff, "Systems of conservation laws," *Comm. Pure Appl. Math.*, vol. 13, pp. 217–237, 1960.

[189] R. F. Warming and R. M. Beam, "Upwind second-order difference schemes and applications in aerodynamic flows," *AIAA Journal*, vol. 14, no. 9, pp. 1241–1249, 1976.

[190] C.-W. Shu, "High order weighted essentially nonoscillatory schemes for convection dominated problems," *SIAM review*, vol. 51, no. 1, pp. 82–126, 2009.

[191] D. J. Acheson, *Elementary fluid dynamics*. Oxford University Press, 1990.

[192] O. Reynolds, *Papers on Mechanical and Physical Subjects*, vol. 3, The sub-mechanics of the universe. Cambridge University Press, 1903.

[193] H. Yamaguchi, *Engineering fluid mechanics*, vol. 85. Springer Science & Business Media, 2008.

[194] T. Belytschko, W. K. Liu, B. Moran, and K. Elkhodary, *Nonlinear finite elements for continua and structures*. John wiley & sons, 2014.

[195] G. Buresti, "A note on stokes' hypothesis," *Acta Mechanica*, vol. 226, pp. 3555–3559, 2015.

[196] J. Serrin, "Mathematical principles of classical fluid mechanics," in *Fluid Dynamics I/Strömungsmechanik I*, pp. 125–263, Springer, 1959.

[197] G. G. Stokes, "On the theories of the internal friction of fluids in motion, and of the equilibrium and motion of elastic solids," *Trans. Cambridge Philos. Soc.*, vol. 8, pp. 287–319, 1845.

[198] H. Lamb, *Hydrodynamics*. Cambridge University Press, 1932.

[199] F. M. White, *Fluid Mechanics*. WCB/McGraw-Hill, 4 ed., 1999.

[200] J. B. Scarborough, *Numerical Mathematical Analysis, 4th ed.* Johns Hopkins University Press, 1958.

[201] D. N. D. G. Allen and R. V. Southwell, "Relaxation methods applied to determine the motion, in two dimensions, of viscous fluid past a fixed cylinder," *Quarterly Journal of Mechanics and Applied Mathematics*, vol. 8, pp. 129–145, 1955.

[202] R. D. Richtmyer and K. Morton, *Difference methods for initial-value problems*. Interscience Publication J. Wiley & Sons, 2 ed., 1967.